Elise Moen

Dynamic responses of monopile wind turbines subjected to nonlinear wave loads

Master's thesis in Marine Technology

Supervisor: Erin Bachynski

June 2020

Master's thesis

NTNU
Norwegian University of Science and Technology
Faculty of Engineering
Department of Marine Technology

NTNU
Norwegian University of
Science and Technology

Dynamic responses of monopile wind turbines subjected to nonlinear wave loads

Master thesis in Marine Technology

Elise Moen

Department of Marine Technology
Norwegian University of Science and Technology
NTNU Trondheim
Spring 2020

NTNU Trondheim
Norwegian University of Science and Technology
Department of Marine Technology – Group of Marine Structures

THESIS IN MARINE TECHNOLOGY

SPRING 2020

FOR

STUD.TECHN. Elise Moen

Dynamic responses of monopile wind turbines subjected to nonlinear wave loads
Dynamisk respons av vindturbiner med monopælfundament til ikke-lineære bølgelaster

Background:
The offshore wind industry is moving toward larger wind turbines and deeper water, and monopile foundations are growing. Due to the increase in top mass and the lower rotational frequencies of the turbine, the first natural frequency of the system is being pushed lower, and the dynamic responses of the system are becoming more important. Furthermore, the increased diameter and increased water depth result in the increasing importance of extreme wave loads.

In the WAS-XL project, experimental investigations of monopile responses to wave loads have been carried out in both regular and irregular waves. The thesis project aims to identify appropriate load models for considering non-linear and breaking waves on monopile foundations (based on comparison against experimental data), and to apply these load models to monopile designs with different dynamic characteristics. Based on the project work, several events of interest have been identified. These events will serve as case studies for the comparisons.

Assignment:
The following tasks should be addressed in the project work:

1. Literature review regarding wave loads on monopile wind turbines, including both numerical and experimental approaches, as well as design standards.

2. Familiarization with the numerical model in SIMA for the WAS-XL flexible monopile by carrying out decay tests and regular wave tests and comparing against experimental results. Tuning of structural damping coefficients and hydrodynamic coefficients. The Morison load model with 2nd order waves serves as the baseline numerical model.

3. Comparison of selected experimental results for irregular waves with the baseline numerical model. Implement a slamming load model and examine the results for selected events with wave breaking.

4. Based on the results, consider the need for implementation of different slamming load models, or of different wave load models (Rainey, KF, etc).

5. Report and conclude on the investigation.

The work scope could be larger than anticipated. Subject to approval from the supervisor, topics may be deleted from the list above or reduced in extent.

In the project, the candidate shall present her personal contribution to the resolution of problem within the scope of the project work.

Theories and conclusions should be based on mathematical derivations and/or logic reasoning identifying the various steps in the deduction.

The candidate should utilize the existing possibilities for obtaining relevant literature.

The project report should be organized in a rational manner to give a clear exposition of results, assessments, and conclusions. The text should be brief and to the point, with a clear language. Telegraphic language should be avoided.

The project report shall contain the following elements: A text defining the scope, preface, list of contents, main body of the project report, conclusions with recommendations for further work, list of symbols and acronyms, reference and (optional) appendices. All figures, tables and equations shall be numerated.

The supervisor may require that the candidate, in an early stage of the work, present a written plan for the completion of the work. The plan should include a budget for the use of computer and laboratory resources that will be charged to the department. Overruns shall be reported to the supervisor.

The original contribution of the candidate and material taken from other sources shall be clearly defined. Work from other sources shall be properly referenced using an acknowledged referencing system.

Erin Bachynski
Supervisor

Deadline: 10.06.2020

Preface

This thesis concludes my Master in Science in Marine Technology at the Norwegian University of Science and Technology. The work was carried out during the spring semester of 2020 and was mostly carried out from home due to the ongoing situation of Covid-19. The experimental data used in this thesis was obtained trough tests at the Department of Marine Technology in June 2019. The experimental data were processed and characterized during the fall semester of 2019 as part of the pre-thesis project. The thesis work has been challenging but also very rewarding and inspiring.

Special thanks go to my supervisor Professor Erin Bachynski for great advise and support through our weekly guidance meetings and numerous emails. Her dedication and extensive knowledge have been of great importance and inspiration to me. I also want to thank Postdoctoral Fellow Fatemeh H. Dadmarzi for help and guidance. Finally, I would like to thank my friends and family for all their support during my master's degree.

Elise Moen

Trondheim, 10.06.20

Abstract

In this thesis, experimental data on a 9-diameter monopile foundation supporting a 10 MW wind turbine subjected to regular and irregular sea have been studied. The experimental data have been compared to numerical methods. The model has a scale of 1:50 and is fully flexible with 1st and 2nd eigenfrequencies and 1st mode shape representative of a full-scale wind turbine. The structural damping coefficients of the numerical model in SIMA are tuned to fit the eigenfrequencies and damping ratio obtained from decay tests of the physical model.

For the regular wave tests, the wave elevation is recreated by linear waves, Stoke's second order waves and stream function waves. The stream function waves provide the best match for the wave elevation when the Ursell number $Ur > 26$. The mudline bending moment was split into contributions of the 1st, 2nd, 3rd and 4th harmonic, and four different numerical methods were compared to the measurements. All methods provided fair estimates of the 1st harmonic response for both steepnesses investigated. For waves of steepness $s = 1/40$, the Morison equation using second order kinematics provided the best estimate of the 2nd harmonic response but was not able to capture the 3rd harmonic response. The 3rd harmonic response was matched well by the FNV method for waves of steepness $s = 1/40$, while severely overestimating for waves of steepness $s = 1/22$. The Morison equation using stream function kinematics provided conservative estimates for the 2nd and 3rd harmonic response for waves of steepness $s = 1/22$ and 2nd harmonic response for waves of steepness $s = 1/40$, but underestimating the 3rd harmonic response for waves of steepness $s = 1/40$. None of the proposed numerical methods were able to capture the correct response in 2nd and 3rd harmonic response for waves of both steepnesses.

20 different high-response events are identified from the measurements of a 3-hour irregular sea state of $H_s = 8.6$ m and $T_p = 11$ s. The response is filtered around the 1st and 2nd eigenfrequency, where the response will consist mainly of 1st and 2nd mode, respectively, and the residue is said to be the quasi-static response. The largest responses are found to occur when there is an excitation of the 2nd mode on top of a ringing response. Three different numerical approaches are tested. The Morison equation using linear kinematics integrated up to the still water level only provides contribution to the quasi-static response, which is underestimated compared to the measurements. The Morison equation combined with stream function kinematics integrated to the free surface is able to trigger ringing response in the 1st mode. This numerical method provides better estimate of the quasi-static response, however, the 1st mode response is generally overpredicted, especially when the measured wave is breaking. The Wienke slamming model is added, which excites 2nd mode response. Compared to the measurements, the 2nd mode contribution is very overestimated. The numerical method ends up providing a conservative estimate of the response from an extreme wave, and the balance between the 1st and 2nd mode response is not captured.

Sammendrag

I denne masteroppgaven blir eksperimentelle målinger fra en vindturbin med monopælfundament utsatt for regulære og irregulære bølger undersøkt. Monopælen har en diameter på 9 meter og bærer en 10 MW vindturbin. Ulike numeriske metoder blir brukt for å estimere responsen, og resultatene blir målt opp mot målinger fra eksperimentet. Modellen er laget i skala 1:50 og er fullt fleksibel. Den har første og andre egenfrekvens, samt første egenmode, som er representativ for en fullskala vindturbin med monopælfundament. De strukturelle dempningskoeffisientene i den numeriske modellen er tilpasset ved å bruke første og andre egenfrekvens og dempningsratio fra den fysiske modellen.

Bølgehevningen i de regulære bølgetestene ble forsøkt gjenskapt ved tre forskjellige metoder: Lineære bølger, Stokes andreordens bølger og strømfunksjonsbølger. Strømfunksjonsbølgene gir det beste estimatet for bølgehevningen når Ursell nummeret $Ur > 26$. Fire ulike numeriske metoder blir sammenlignet mot målingene fra eksperimentet. Responsen er fremstilt ved bøyemoment i bunnen av fundamentet, og er delt opp i bidrag fra første til fjerde harmonisk. Alle metodene ga rimelige estimater av første harmonisk respons for begge bølgesteilhetene. For bølger med steilhet $s = 1/40$ ga Morison modellen med andreordens kinematikk det beste estimatet av andre harmonisk respons, men den klarte ikke å gjengi tredje harmonisk respons. Tredje harmonisk respons ble best estimert av FNV modellen for bølger med steilhet $s = 1/40$, men for bølger av steilhet $s = 1/22$ ble denne kraftig overestimert. Morison modellen med strømfunksjons kinematikk ga konservative estimater av andre og tredje harmonisk respons i bølger med steilhet $s = 1/22$ og andre harmonisk respons i bølger med steilhet $s = 1/40$, men underestimerte tredje harmonisk respons. Ingen av de undersøkte numeriske metodene klarte å gjengi korrekt respons i andre og tredje harmonisk respons for begge bølgesteilheter.

20 ulike hendelser med høy respons er identifisert fra målingene av en tre timers irregulær sjøtilstand med $H_s = 8.6$ s og $T_p = 11$ s. Responsen er filtrert rundt første og andre egenfrekvens, der den vil bestå hovedsakelig av henholdsvis første- og andremode. Kvasistatisk respons er definert som resten etter at første- og andremode respons er trukket fra den totale responsen. De største responsene finner sted når andremode blir eksitert samtidig som førstemode opplever transient respons, såkalt ringing. Tre ulike numeriske metoder blir sammenlignet mot målingene fra eksperimentet. Morison modellen med lineær kinematikk integrert opptil stillevannsnivå gir kun kvasistatisk bidrag til den totale responsen. Den kvasistatiske responsen er underestimert sammenlignet med målingene. Morison modellen med strømfunksjons kinematikk integrert opp til den faktiske bølgehevningen er i stand til å eksitere ringing i førstemode. Denne metoden gir bedre estimat av den kvasistatiske responsen, men responsen i førstemode er generelt overestimert, spesielt når den målte bølgen er brytende. Når Wienkes slamming modell legges til, blir andremode eksitert også. Sammenlignet med målingene er bidraget fra andremode meget overestimert. Den numeriske modellen gir derfor et konservativt estimat av responsen fra en ekstrem bølge, og balansen mellom første- og andremode blir ikke korrekt representert.

Contents

List of Figures

List of Tables

List of Symbols

ζ	Wave elevation
ζ_A	Wave amplitude
H	Wave height
ω	Radial frequency
h	Water depth
a	Monopile radius
t	Time
k	Wave number
x	Horizontal position
ε	Phase of wave
Φ	Velocity potential
g	Gravitational acceleration
z	Vertical position
u	Horizontal velocity
$dudt, \dot{u}$	Horizontal acceleration
s	Steepness
λ	Wave length
T	Wave period
S	Spectrum
f	Frequency in Hz
f_p	Peak frequency
U_r	Ursell number
ψ	Stream function
c	Wave celerity
$\bar{U}$	Mean fluid speed
v	Vertical velocity
H_b	Breaking wave height
F	Force
ρ	Density of sea water
C_M	Mass coefficient
C_D	Drag coefficient
D	Monopile diamater
ϕ	Total potential
ζ_I	Incident wave elevation
C_s	Slamming coefficient
λ_c	Curling factor
η_b	Breaking wave amplitude
ω_n	Eigenfrequency
K	Stiffness
M	Mass
C	Damping
Q	External loads
DAF	Dynamic amplification factor
ξ	Damping ratio
u_i, X_n	Amplitude of the i'th or n'th oscillation
T_m	Period of oscillation
p_1	Linear damping coefficient
p_2	Quadratic damping coefficient
α_1	Mass damping coefficient
α_2	Stiffness damping coefficient
F_N	Froude number
H_s	Significant wave height
T_p	Peak period
f_0	Eigenfrequency
T_0	Time of peak

1 Introduction

Today, the monopile foundation is the most popular foundation type in water depth up to 30-40 meters, due to it being a relative cheap and simple construction [1]. The offshore wind industry is moving towards larger wind turbines and deeper waters, causing the monopile foundations to grow as well. Due to increasing top mass and lower rotational frequencies of the wind turbine, the first eigenperiod of the system is being pushed higher, closer to the primary wave periods (3-5s). This causes the dynamic responses of the system to become more important. Furthermore, the increased diameter of the monopile foundation and the increasing water depths also results in a greater importance of extreme wave loads.

As the dimensions of the monopile foundation grow, so do the costs. Therefore, avoiding being over-conservative is important. In order to evaluate this, an understanding of the loads subjected to the foundation is vital. In the WAS-XL project (Wave loads and soil support for extra large monopiles), experimental investigations of monopile responses to wave loads have been carried out in both regular and irregular waves [2]. The wind turbine modelled in the experiment is representing a 10 MW wind turbine with a monopile foundation of 9 meter diameter at 27 meter water depth. The thesis aims to identify appropriate load models for considering non-linear and breaking waves on monopile foundations (based on comparison against experimental data), and to apply these load models to monopile designs with different dynamic characteristics. In the project work, the main focus was to be on becoming familiar with the state-of-the-art and the available experimental data set. Relevant results and discussions from the project work will also be included in the thesis.

Particular responses of interest are ringing due to steep waves and excitation of the second eigenmode due to breaking waves. Ringing is defined as the transient response at frequencies higher than the incident wave frequency [3], and generally occurs after the passing of a high steep wave [4]. Studies have shown that inclusion of these responses are important in order to correctly predict the maximum response of a monopile structure [5]. While ringing is associated with transient effects, springing is the steady-state oscillation response to sum-frequency forces [3].

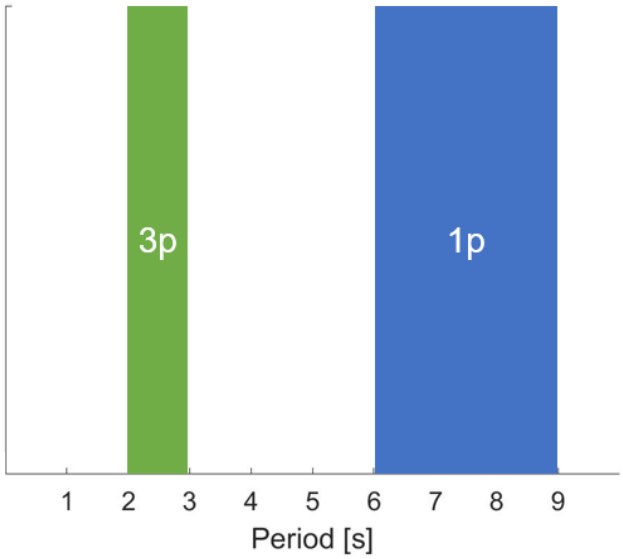

Figure 1.1: Approximate 1p and 3p periods for a 10 MW rotor. 1p is due to the passing rotation of the turbine blades, while 3p is due to the passing of one turbine blade in front of the tower

2 Literature review

Similar studies have previously been done on the subject. Particular relevant studies are those published by Loup Suja-Thauvin in relation to his Ph.D. thesis. In 2017 Suja-Thauvin et al. presented experimental data from tests on a bottom-fixed monopile subjected to severe irregular wave conditions [6]. The test was performed at Maritime Research Institute Netherlands (MARIN) and the turbine studied represents is a 4 MW turbine, with a diameter at mean sea level of 5.8 m. The first article published in 2017 focuses on the response of the monopile wind turbine. Two different models are studied, where one is fully flexible with representative 1st and 2nd eigenfrequency, and 1st mode shape is representative of the full-scale turbine. The other model is stiff in order to study the hydrodynamic excitation loads. The first and second eigenfrequency were found to be 0.29 Hz and 1.21 Hz respectively, while the damping ratio for the 1st and 2nd mode is 1.1%. Suja-Thauvin et al. discuss that this may result in somewhat conservative results, as the damping ratio of the first mode in full scale is somewhat larger ($1.7 - 2.8\%$), dependant on the wind speed. However, it is further discussed that this may be of less importance to the maximum values than for the decays.

The responses were filtered into contributions from the quasi-static response (typically wave load), 1st mode response and 2nd mode response. 21 different events were identified and studied and it was found that the most significant responses occurred when there was excitation of the second mode due to a breaking wave on top of a ringing response. The contribution from quasi-static response dominates with between $40 - 50\%$ of the total response, while 1st mode response accounts for between $30 - 40\%$ and the 2nd mode response with up to 20%.

A study of long-term monitoring of an offshore 3 MW turbine published in 2013, focuses on resonant frequencies and damping values of the dominant modes of the support structure [7]. Devriendt et al. discusses the importance of accurate damping ratio in relation to fatigue and lifetime predictions. Further, the damping of an offshore wind turbine will consist of a combination of aerodynamic damping, damping due to added devices (such as a tuned mass damper), structural damping, soil damping and hydrodynamic damping. The actual damping ratio of a structure is hard to predict by numerical tools, stating the importance of such measurements. In the study, the focus is on the conditions when the turbine is parked or idling due to the reduced aerodynamic damping and the increased dynamic response in these conditions. The mean damping ratio is found to be between $0.72 - 2.49\%$, dependent on the mode shape. The first fore-aft bending mode is found to have a mean damping ratio of 1.86%, while the second fore-aft mode, including the nacelle, has a mean damping ratio of 1.14%.

In 2018, Loup Suja-Tauvin et al. continued to investigate the same experimental data set as presented in 2017 [5]. This paper focuses on comparing the experimental data with numerical models suggested in offshore wind energy standards in order to assess the ultimate limit state (ULS) conditions. Numerical models can provide conservative estimates of extreme responses. However, the balance between the first and second mode responses seen in model measurements are not captured. In addition, the simplifications done in the numerical models can lead to inaccuracies in the response prediction. Three numerical models were applied: Morison with linear kinematics, Morison with stream function wave kinematics and Morison with steam function wave kinematics together with Wienke's slamming model [8]. The linear kinematics are obtained by linearizing the wave elevation measured during the experiment. The stream function kinematics are obtained by embedding a stream function wave into the linearization of the measured wave elevation. The quasi-static response was in general accurately estimated regardless of linear or stream function wave kinematics. However, when linear wave kinematics was used, neither 1st or 2nd mode response was excited, so

the linear Morison model was not able to match the measured response [5]. This finding agrees with the ones reported by, amongst others, Paulsen et al. in 2013, stating the limitations of using linear wave kinematics to simulate extreme waves [9]. The ringing responses were inconsistently predicted by the Morison equation in combination with the stream function kinematics. The 2nd mode was only excited if a slamming model, such as Wienke, was applied. For a total of 51 events, the response was overestimated 17 times. Where the models overestimated the total response, the 2nd mode response was also overestimated, meaning that the balance between the 1st and 2nd mode response might not be accurate.

Another experiment was set up by Erin Bachynski et al. at the Ocean basin at SINTEF Ocean and published in 2019 [10]. This also included a fully flexible model, this time representative of a 5 MW offshore wind turbine. This paper focuses on comparing the experimental data with two models, numerical and analytical, and assess the uncertainties. The results suggest that the bias errors in the model properties and in the wave elevation contribute the most to the total uncertainty. It is also found that the numerical model does not capture all of the responses within the level of uncertainty of the experiments. This paper also assesses the repeatability of the tests, where an identical signal is sent to the wavemaker. One realization of the sea state with H_s = 9 m and T_p = 12.3 s was run in total 9 times with the model and 3 times without. The coefficient of variation (ratio of the standard deviation to the mean) of the extreme bending moment is found to be 18%, while the calibrated wave has a coefficient of variation of 7 %.

Another experimental and numerical study of the response of a monopile subjected to steep and breaking waves was presented by Henrik Bredmose et al. in 2013 [11]. The monopile wind turbine structure was modeled by a pile at scale 1:80 and two masses were mounted to achieve accurate 1st and 2nd eigenfrequencies of the NREL 5 MW monopile at a water depth of 20 meters. The eigenfrequencies are 0.28 Hz and 2.0 Hz, while the mode shapes are not preserved. The model was placed on a sloping sea bed. The structural accelerations were analyzed with respect to individual wave parameters, and it was found that the largest response occur for breaking waves. Using a fully nonlinear potential flow solver combined with a finite element model of the pile with Morison loading, the measured wave and response were reproduced. The solver gave accurate reproductions for two selected episodes, but for some of the waves the response did not match the measurements.

A comparison of different approaches for estimating the wave impact force from steep and breaking waves was published by Burmester et al. in 2017 [12]. This study was a part of the Joint Industry Project Wave Impacts on Fixed turbines (WiFi JIP) project. The tests were conducted at MARIN and at Deltares. Breaking waves were generated at MARIN by producing a focused wave. The impact approaches tested are Wienkes slamming model and the formulation under development in the WiFi project, and they are both added to the quasi-static wave load estimated by the Morison equation using stream function wave kinematics. It was found that there is a strong correlation between the type of breaker and the wave load measured, suggesting that identification of the breaker type is important when analyzing wave slamming loads. It is also shown that representing a plunging breaking wave by a stream function wave causes a discrepancy of the results for the quasi-static load. The impact duration of Wienke was also used in the WiFi formulation, however, compared with the measurements it is found to be too short. In conclusion, it was found that applying the Wienke slamming model to the quasi-static loading corresponds well with the measurements. The WiFi formulation is found the estimate the load from spilling breakers well but underestimates the load from the plunging breakers.

In 2016, H. Bredmose et al. presented the first result of the DeRisk project [13]. The loads from extreme wave events can be dimensioning for the foundation of offshore wind turbines, and therefore this paper aims to provide a de-risked load evaluation procedure for extreme wave loads. The research is based on both numerical tools, experimental model tests and statistical analyses. The goal is to develop new methods enabling fully nonlinear kinematics to be applied while assessing them against existing methods. Fully non-linear wave kinematics are computationally expensive, and therefore a goal within the DeRisk project is to produce a database of fully nonlinear kinematics.

A paper using the same experimental data studied in this report has been published by Fatemeh H. Dadmarzi et al. in 2019 [4]. However, for the most part data from the stiff model as opposed to the flexible model was used. This paper aims to validate hydrodynamic loads on the monopile subjected to regular waves of increasing steepness. Different methods are tested to validate the prediction of first, second and third harmonic wave loads, including generalized FNV model, Morison equation and MacCamy-Fuchs method.. It was found that for the first harmonic load, MacCamy-Fuch provided the best estimate compared to the experimental results. For the short waves, the second harmonic load was generally overpredicted, while for long waves, they were underpredicted. The third harmonic load was overpredicted by the calculations.

One of the methods tested by Fatemeh H. Dadmarzi et al. was the generalized FNV model. The FNV model, named after authors Faltinsen, Newman and Vinje, were first reported in 1995 [14]. The model were developed by analytic studies of ringing loads on a fixed, non-moving surface piercing cylinder subjected to incident waves in deep waters. In 2017, Kristiansen and Faltinsen further generalized the model to be valid in finite water depth [15]. One important difference of deep and finite water depths is that the third-order incident potential is zero for deep water depths while it is a dominant contributor to the third harmonic load in finite water depths [15]. Harmonic loads oscillating from 1ω to 5ω were studied, however, the main focus was the 3ω loads. For small to medium steep waves, the predicted 3ω load agreed well with the experiments, but for steeper waves above some limit, the load was overpredicted. For the conditions reported by Kristiansen and Faltinsen, this limit was found to be $H_1/\lambda = 1/40$, where H_1 is the linear wave height. The tests were performed at two different water depths; $h/a = 7.83$ and $h/a = 5.51$, where h is the water depth and a is the radius of the monopile. Generally, for waves steeper than the limit of $1/40$, local run up at the rear of the monopile was observed, which again caused a local steep wave propergating against the incident wave. This was believed to be the cause of significant 3ω, 4ω and 5ω loads [15].

There are various other methods that includes nonlinearities in irregular waves, one of them being Computational Fluid Dynamics (CFD). CFD is based on generating an approximate solution to the Navier-Stokes equation, and is often used when simulating breaking waves. However, the CFD is computationally expensive [1]. Another method is the fully non-linear potential flow theory, which integrates the Laplace equation with fully nonlinear boundary conditions at the water surface. One such fully nonlinear potential flow solver is OsceanWave3D, presented by Ensig-Karup et al [16]. However, this method is also proven to be computationally expensive. A computationally cheaper method is the long-crested second-order model by Longuett-Higgins, which corrects the sum-frequencies and difference frequencies, resulting in a nonlinear irregular wave [17].

3 Theory

This sections explains some of the underlying theory used throughout the thesis work. It starts by presenting linear wave theory, before moving onto irregular waves and nonlinear waves. The relevant hydrodynamic load models are then presented, before response of a monopile structure and how to find its eigenfrequencies and damping ratio is presented at the end.

3.1 Regular linear waves

The foundation of higher order wave theory is found in the linear wave theory (Airy theory). The understanding of these theories is crucial before introducing higher order theories. The wave elevation of a linear wave can be described as

$$\zeta(t) = \zeta_A \cos(\omega t - kx + \varepsilon) \tag{3.1}$$

where ζ_A is the wave amplitude, which is half of the wave height H, $\omega = 2\pi/T$ is the radial frequency of the wave, t is the time, $k = 2\pi/\lambda$ is the wave number, x is the position in space and ε is the phase of the wave. An illustration of a cosine wave elevation can be seen in Figure 3.1.

Further, the velocity potential of a propagating wave in finite water can be derived as

$$\Phi = \frac{\zeta_A g}{\omega} \frac{\cosh k(z+h)}{\cosh kh} \sin(\omega t - kx + \varepsilon) \tag{3.2}$$

where h is the water depth and k is the wave number [3]. This can be used to express the horizontal and vertical wave particle velocity and acceleration components, namely the wave kinematics. The horizontal velocity and acceleration are given below:

$$u = \omega \zeta_A \frac{\cosh k(z+h)}{\sinh kh} \cos(\omega t - kx + \varepsilon) \tag{3.3}$$

$$dudt = \frac{du}{dt} = -\omega^2 \zeta_A \frac{\cosh k(z+h)}{\sinh kh} \sin(\omega t - kx + \varepsilon) \tag{3.4}$$

These again are used to derive the loading on an object present in the sea. However, the linear wave theory is only able to describe wave kinematics up to the mean sea level ($z = 0$), and the need for a profile extension method therefore arises. Popular examples of such methods are constant extrapolation, Wheeler stretching and Taylor expansion model [18].

In linear wave theory, wave steepness is defined as

$$s = \frac{H}{\lambda} \tag{3.5}$$

where s is wave steepness, H is the wave height and λ is the wave length illustrated in Figure 3.1 [19]. For finite water depths, the maximum wave steepness can be calculated as

$$s = \frac{1}{7} \tanh\left(\frac{2\pi h}{\lambda}\right) \tag{3.6}$$

where h here denotes the water depth. Further, for finite water depths, the wave length λ can be iterated from

$$\lambda = \frac{gT^2}{2\pi} \tanh\left(\frac{2\pi h}{\lambda}\right) \tag{3.7}$$

where T is the wave period and g is the acceleration of gravity [18].

When the water depth is greater than $\lambda/2$ it is known as deep water [18]. The steepness in Equation 3.6 will then be reduced to $1/7$, and we can derive the limiting wave height as $\lambda/7$. This implies that if the wave height exceeds this value, it will break. Shallow water is defined when the water depth is less than $\lambda/20$. For shallow waters, the breaking wave limit is found to be $0.88h$. In practice, a wave is characterized as breaking if there is foam present.

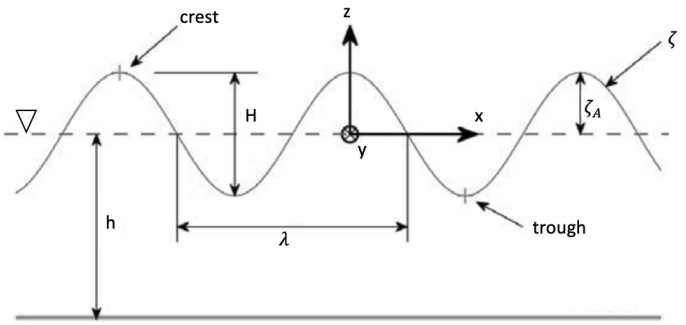

Figure 3.1: Regular wave for illustration of different definitions

3.2 Irregular waves

The waves we see in real life, does not behave according to regular wave theory. We therefore need to introduce the concept of irregular waves. A sea state can be described as a series of regular, long crested waves with different amplitudes, frequencies and phase angles [20]. At a given location $x = 0$ the wave elevation can be described as

$$\zeta(t) = \sum_{n=1}^{N} \zeta_{An} \cos\left(\omega_n t + \varepsilon_n\right) \tag{3.8}$$

The wave process is assumed to be stationary, meaning that within an time interval of approximately 20 minutes to 3 hours, the mean value and the variance of the process will be constant. It is also assumed that the wave elevation is Gaussian distributed with zero mean and variance of σ^2. Lastly, it is assumed that the wave process is ergodic. This implies that one time series of the wave elevation can represent the whole wave process, and that the expected value and the variance can be found from time averaging of the single time series [20].

Further, the spectrum $S(\omega)$ of $\zeta(t)$ can be introduced, and the wave elevation at $x = 0$ can now be expressed as

$$\zeta(t) = \sum_{n=1}^{N} \sqrt{2S\left(\omega_n\right)\Delta\omega} \cos\left(\omega_n t + \varepsilon_n\right) \tag{3.9}$$

However, it should be noted that this is a sum of linear wave components. Nonlinear waves will be touched upon in section 3.4.

3.3 Spectrum

As introduced in the previous section, a spectrum is needed in order to describe irregular sea states. One such spectrum is called "Joint North Sea Wave Project" (JONSWAP) spectrum. This spectrum is the result of a measurement project in the South-Eastern part of the North Sea in 1968 and 1969, and represents a developing sea [20]. The spectrum has its origin from the Pierson-Moskowitz (PM) spectrum, which is given as

$$S(\omega) = \frac{A}{\omega^5} \exp\left[-\frac{B}{\omega^4}\right] \tag{3.10}$$

where A and B is given as

$$\begin{aligned} A &= 0.0081g^2 \\ B &= 0.74\left(\tfrac{g}{U}\right)^4 \end{aligned} \tag{3.11}$$

U is the wind speed at an altitude of 19.5 metes above the sea surface [20].

However, the JONSWAP spectrum is described by the peak frequency, f_p, instead of the wind speed. In addition, the spectrum is peaked by multiplying with a peakedness factor γ. The JONSWAP spectrum is therefore expressed as

$$S(f) = \frac{\alpha g^2}{16\pi^4} f^{-5} \exp\left[-\frac{5}{4}\left(\frac{f}{f_\mathrm{p}}\right)^{-4}\right] \gamma^b \tag{3.12}$$

where α=0.0081, g is the gravitational acceleration and the factors b and σ is given as

$$\begin{aligned} b &= \exp\left[-\tfrac{1}{2\sigma^2}\left(\tfrac{f}{f_\mathrm{p}} - 1\right)^2\right] \\ \sigma &= \begin{cases} \sigma_a & \text{for } f \leq f_\mathrm{p} \\ \sigma_b & \text{for } f > f_\mathrm{p} \end{cases} \end{aligned} \tag{3.13}$$

One example of a JONSWAP spectrum is given in Figure 3.2.

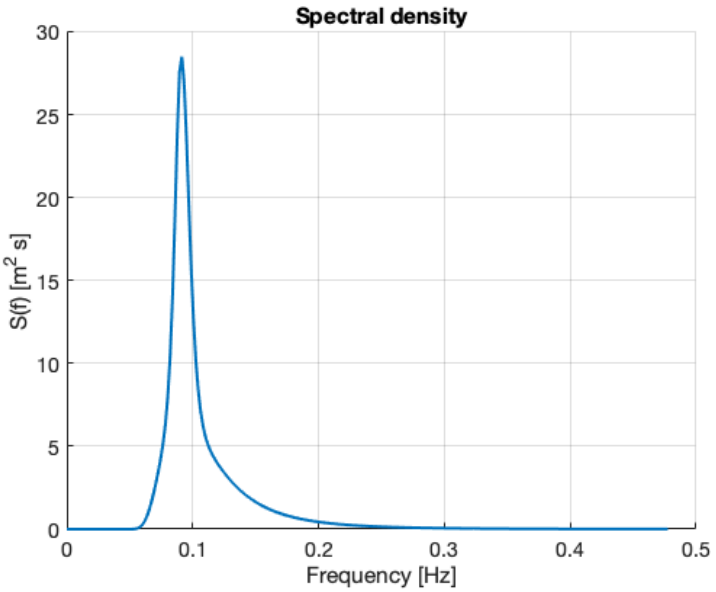

Figure 3.2: JONSWAP spectrum with the following input: f_p=0.09 Hz, γ=4.2, σ_a=0.07 and σ_b=0.09

3.4 Nonlinear waves

When the waves are too steep linear wave theory is no longer valid, as is illustrated in Figure 3.4 [21]. The spectrum will no longer give a complete description of the waves. When there is deep waters, the waves are generally not too steep, and the linear wave model often suffices [1]. However, offshore wind farms are generally located in more shallow waters, and the nonlinear effects will therefore be more pronounced.

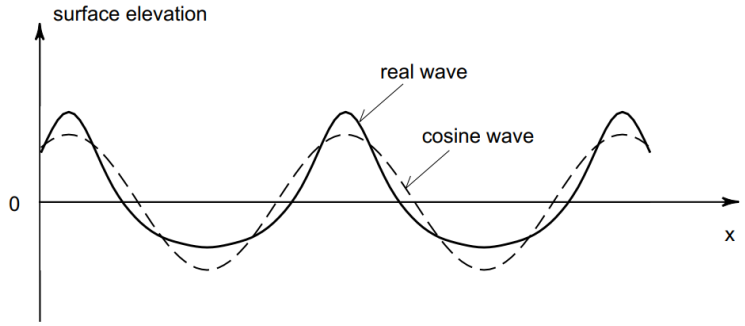

Figure 3.3: Comparison of a linear cosine wave and a nonlinear wave [22]

The degree of nonlinearity of the wave can be described by the Ursell number U_r

$$U_r = \frac{\text{steepness}}{(\text{relative depth})^3} = \frac{H/\lambda}{(h/\lambda)^3} = \frac{H\lambda^2}{h^3} \tag{3.14}$$

where H is the wave height, λ is the wave length and h is the depth [21].

To account for these nonlinearities, there are various nonlinear regular methods developed. One such method is Stokes theory [21], which is commonly used for steep waves with $U_r < 10$. The Stokes theory presents a better approximation of the nonlinear waves by adding higher order corrections to the regular wave, resulting in steeper crests and wider troughs than for regular waves [17]. For shallow waters with $U_r > 26$, the Cnoidal theory is generally more applicable [21]. This is due to the formation of a secondary peak in the wave trough for the Stokes 2nd order wave. For decreasing water depths, the wave crests will get sharper and the troughs will be flatter. Applicability of the different nonlinear regular wave methods can be seen in Figure 3.4.

The methods presented have limitations in applicability. Due to this, a more general formulation has been developed, namely the stream function wave theory [23]. The upside with this method is that it is able to describe the wave kinematics up to the actual free surface, and therefore a profile extension method is not needed. Miche's breaking limit criterion is used to predict the breaking wave height in both deep and shallow waters;

$$\frac{kH_\mathrm{b}}{\gamma \tanh kh} = 1 \tag{3.15}$$

where H_b is the breaking wave height and γ is a constant parameter[24]. When the water is deep, $\tanh kh \approx kh$ which results in the breaking limit

$$\frac{H_\mathrm{b}}{\lambda} = \frac{\gamma}{2\pi} \approx 0.14 - 0.17 \tag{3.16}$$

When there is shallow waters, $\tanh kh \approx 1$ which leads to the breaking limit of

$$\frac{H_\mathrm{b}}{h} = \gamma \approx 0.7 - 0.8 \tag{3.17}$$

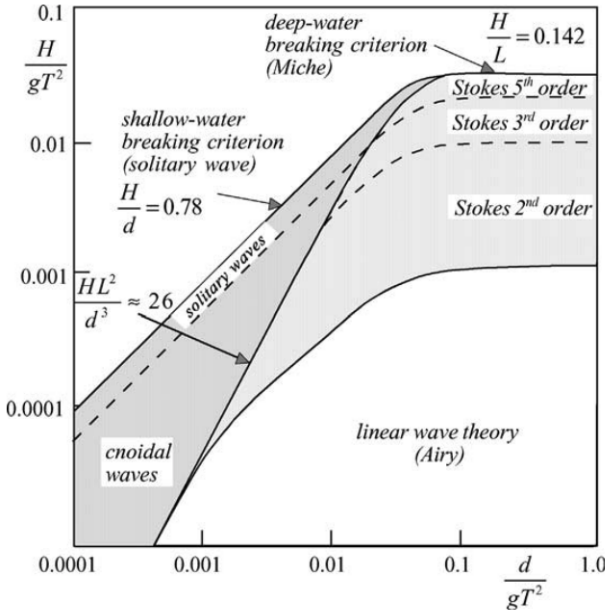

Figure 3.4: Applicability of nonlinear regular wave models [21]

In order to include nonlinearities in irregular waves, various methods has been developed. As mentioned in section 2, CFD and fully non-linear potential flow theory is two such methods. The methods can provide very accurate results, however, they are computational expensive. Another, more simple method, is the long-crested second-order model by Longuett-Higgins [17]. This method has corrections both to the sum-frequencies and to the difference frequencies. This method will result in an irregular wave state where the crests are generally higher and steeper, and the troughs are shallower. The method is based on correcting the linear wave component, which we defined in subsection 3.2, at a given location $x = 0$

$$\zeta_1(t) = \sum_{n=1}^{N} \zeta_{An} \cos\left(\omega_n t + \varepsilon_n\right) \tag{3.18}$$

The second order irregular wave is then found as $\zeta_2 = \zeta_1 + \Delta\zeta_2$ [17]. The second order correction is given by

$$\begin{aligned} \Delta\zeta_2 = &\sum_{m=1}^{N}\sum_{n=1}^{N} \zeta_{Am}\zeta_{An} E_{mn}^{(+)} \cos\left[\left(\omega_m + \omega_n\right)t + \left(\varepsilon_m + \varepsilon_n\right)\right] \\ &+ \sum_{m=1}^{N}\sum_{n=1}^{N} \zeta_{Am}\zeta_{An} E_{mn}^{(-)} \cos\left[\left(\omega_m - \omega_n\right)t + \left(\varepsilon_m - \varepsilon_n\right)\right] \end{aligned} \tag{3.19}$$

where $E_{mn}^{(\pm)} = E^{(\pm)}\left(\omega_m, \omega_n\right)$ is the quadratic surface elevation transfer functions [17].

3.4.1 Stokes' finite amplitude waves

The Stokes' theory is a classical nonlinear wave theory, implying that the waves are assumed to be periodic and permanent (they do not change as they propagate) [21]. The principle of the Stokes theory is to express the velocity potential, surface elevation, wave kinematics and dynamic pressure as a series expansion. In order for the Stokes theory to be valid, the series has to converge, meaning that the next term must always be smaller than the previous one. The first order term corresponds to Airy wave theory, and the higher order terms therefore act as corrections of the Airy wave theory. The Stokes 5th order wave theory is often applied in design of offshore structures [25]. The expansion of the velocity potential up to the order i can be expressed as

$$\Phi = \Phi^{(1)} + \Phi^{(2)} + \ldots + \Phi^{(i)} + \ldots \tag{3.20}$$

where the order of magnitude is given as [22]

$$o\left(\Phi^{(i+1)}\right) = o\left(\Phi^{(i)} \cdot \frac{H}{\lambda}\right) = o\left(\Phi^{(i-1)} \cdot \left(\frac{H}{\lambda}\right)^2\right) = \ldots = o\left(\Phi^{(1)} \cdot \left(\frac{H}{\lambda}\right)^i\right) \tag{3.21}$$

The expression for the surface elevation can then be expressed similarly as the velocity potential.

$$\zeta = \zeta^{(1)} + \zeta^{(2)} + \ldots + \zeta^{(i)} + \ldots \tag{3.22}$$

When applying higher order corrections to the Airy wave theory (1st order Stokes), the wave height will no longer be symmetrical about the mean still water level, and the wave height is therefore defined as the difference between the maximum and minimum surface elevation.

$$H = \zeta_{\max} - \zeta_{\min} \tag{3.23}$$

For a Stokes 2nd order wave, the wave crests are steeper and the troughs wider than for 1st order waves (linear waves)[25]. The velocity potential can be written as a sum of the 1st and 2nd order velocity potential expressions

$$\Phi = \Phi_1 + \Phi_2 = \frac{g\zeta_A}{\omega}\frac{\cosh k(z+h)}{\cosh kh}\sin(kx - \omega t) + \frac{3}{8}\zeta_A^2\omega\frac{\cosh 2k(z+h)}{\sinh^4 kh}\sin 2(kx - \omega t) \tag{3.24}$$

Following this, the free surface elevation can be expressed as

$$\zeta = \zeta_A \cos(kx - \omega t) + \frac{1}{4}k\zeta_A^2\frac{\cosh kh}{\sinh^3 kh}(2 + \cosh 2kh)\cos\big(2(kx - \omega t)\big) \tag{3.25}$$

As seen by the last cosine term, the second order wave elevation correction is oscillating twice as fast as the first order term, causing the amplification of the wave peaks and attenuation of the wave trough as seen in Figure 3.5.

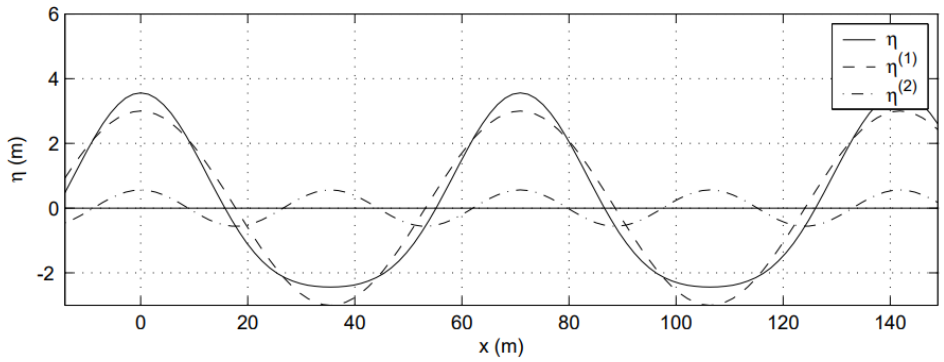

Figure 3.5: Illustration of the 1st and 2nd order Stokes wave terms (here η is the wave elevation known as ζ) [22]

However, as mentioned earlier, the most common order of the Stokes wave theory applied in design is the fifth order. By increasing the order of the Stokes wave theory, the extent of the calculations also increases. A fifth order theory was presented by Skjelbreia in 1960 [26]. The theory assumes that the wave period, wave height and water depth is known. The wave length λ and the coefficient λ_s is found by iteration. The full extent of these iterations are not covered in this section, but can be found in the publication of Skjelbreia [26].

After completion of the iterations, the velocity potential can be obtained by

$$\Phi = -\frac{c}{k}\sum_{j=1}^{5} D_j \cosh jk(z+h)\sin j(\omega t - kx) \tag{3.26}$$

where $c = \lambda/T$ is the wave celerity, $k = 2\pi/\lambda$ is the wave number and h is the given water depth. The coefficient D_j is a function of the iterated coefficent λ_s and the known function $A_{jm} = A_{jm}(kh)$ which are given by Skjelbreia [26]. Further, the horizontal velocity component is given as

$$u = c\sum_{j=1}^{5} jD_j \cosh jk(z+h)\cos j(\omega t - kx) \tag{3.27}$$

Lastly, the wave elevation is written as a sum of all five terms as

$$\zeta = \frac{1}{k}\sum_{j=1}^{5} E_j \cos j(\omega t - kx) \tag{3.28}$$

where the coefficent E_j is found similar to D_j as a function of λ_s and the known function $B_{jm} = B_{jm}(kh)$.

3.4.2 Stream function waves

The stream function theory provides wave kinematics and wave lengths for a constant form wave in constant water depth. It is based on expanding the stream function and the wave elevation into Fourier series. The theory was first presented by Dean in 1965 [27], and later further developed to include the highest possible waves by Rienecker and Fenton in 1981 [23]. In this section, the formulation from Fenton in 1999 is used [28].

The fixed coordinate system, which is the one typically of interest in engineering, is placed on the sea bed. For the sake of convenience, the problem is first solved in a moving coordinate system (X, Y) moving with the wave velocity c in positive x-direction illustrated in Figure 3.6. For later application, a fixed frame (x, y) is applied. To set the frame at the mean still water level, y is replaced with $y = z + h$.

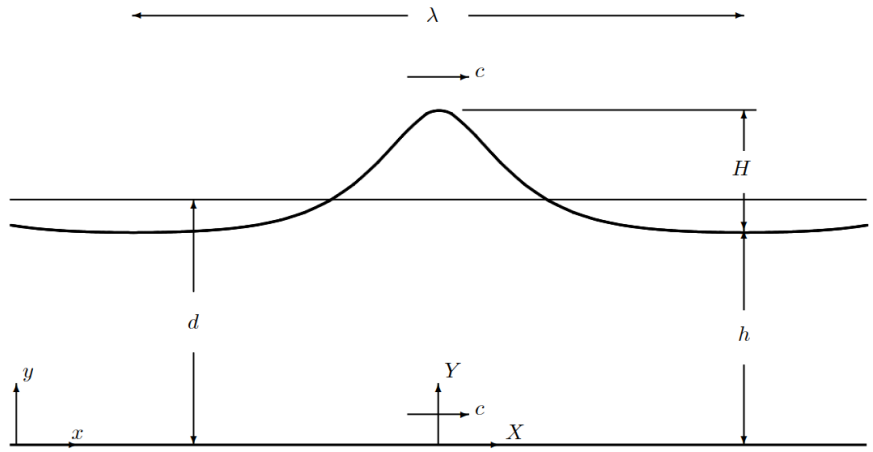

Figure 3.6: Sketch of the stream function wave observed from a coordinate system following the wave [28]

In the moving coordinate system all motion will be steady and the stream function formulation can be applied. The relation between the coordinate systems will be $x = X + ct$ and $y = Y$ where t is the time. Assuming incompressible fluid, the velocity components in the fixed frame can be written as $U = \delta\psi/\delta Y$ and $V = \delta\psi/\delta X$. Further, the motion is assumed to be irrotatioal $\nabla \times \mathbf{u} = \mathbf{0}$. The Laplace equation will then be satisfied by

$$\frac{\partial^2 \psi}{\partial X^2} + \frac{\partial^2 \psi}{\partial Y^2} = 0 \tag{3.29}$$

while the bottom and surface boundary conditions will be

$$\psi\left(X, 0\right) = 0 \quad ; \quad \psi\left(X, \zeta\left(X\right)\right) = -Q \tag{3.30}$$

where $Y = \zeta(X)$ and Q is a positive constant denoting the volume rate of flow per unit length normal to the flow underneath the stationary wave in the moving frame, also called the discharge, and is given by

$$Q = \int_{-h}^{\zeta} u dy \tag{3.31}$$

Lastly, the dynamic boundary condition of zero pressure at the surface must be satisfied, such that the Bernoulli's equation becomes

$$\frac{1}{2}\left(\left(\frac{\partial\psi}{\partial X}\right)^2+\left(\frac{\partial\psi}{\partial Y}\right)^2\right)+g\zeta=R \tag{3.32}$$

on the free surface, where R is a constant.

The stream function can now be written in the moving coordinate system as

$$\psi(X,Y)=-\bar{U}Y+\sqrt{\frac{g}{k^3}}\sum_{j=1}^{N}B_j\frac{\sinh jkY}{\cosh jkh}\cos jkX \tag{3.33}$$

where $\bar{U}$ is the mean fluid speed on any horizontal line under the stationary wave. B_j are dimensionless constant for a particular wave, while N is a finite integer, k is the wave number and h is the still water depth.

The mean current a stationary meter would measure is given by

$$\bar{u_1}=c-\bar{U} \tag{3.34}$$

where $c=\lambda/T$ is the wave speed and $\bar{U}$ is the mean fluid speed. If there is no current, $\bar{u_1}=0$ and $c=\bar{U}$ which is called Stokes' first approximation to the wave speed. The mass-transport velocity is similary given as

$$\bar{u_2}=c-\frac{Q}{h} \tag{3.35}$$

However, in a closed wave tank there will not be any mass transport and $\bar{u_2}=0$ and $c=Q/h$ which is Stokes' second approximation of the wave speed.

Converting to the fixed, physical frame, the velocity potential is now given by

$$\Phi(x,y,t)=(c-\bar{U})x+\sqrt{\frac{g}{k^3}}\sum_{j=1}^{N}B_j\frac{\cosh jky}{\cosh jkh}\sin jk(x-ct)+C(t) \tag{3.36}$$

where $C(t)$ is just an addition added for generality. The velocity components $u=\delta\Phi/\delta x$ and $v=\delta\Phi/\delta y$ anywhere in the fluid is given as

$$u(x,y,t)=c-\bar{U}+\sqrt{\frac{g}{k}}\sum_{j=1}^{N}jB_j\frac{\cosh jky}{\cosh jkh}\cos jk(x-ct) \tag{3.37}$$

and

$$w(x,y,t)=\sqrt{\frac{g}{k}}\sum_{j=1}^{N}jB_j\frac{\sinh jky}{\cosh jkh}\sin jk(x-ct) \tag{3.38}$$

For a mass dominated system, the accelerations will be more important than the velocities due to the mass forces being much larger than the viscous forces. The horizontal acceleration from the stream function will be $du/dt = \delta^2\Phi/\delta x^2$ given as

$$\frac{du}{dt}(x,y,t) = kc\sqrt{\frac{g}{k}}\sum_{j=1}^{N} j^2 B_j \frac{\cosh jky}{\cosh jkh}\sin jk(x-ct) \tag{3.39}$$

When estimating the acceleration in nonlinear waves, the convective acceleration terms may be non-zero due to the flow being non-steady. The total acceleration term is given below

$$\frac{du}{dt} = \underbrace{\frac{\partial u}{\partial t}}_{\text{local}} + \underbrace{u\frac{\partial u}{\partial x} + w\frac{\partial u}{\partial z}}_{\text{convective}} \tag{3.40}$$

where the local acceleration would be given by Equation 3.39.

The surface elevation is given as

$$\zeta(x,t) = 2{\sum_{j=0}^{N}}'' E_j \cos jk(x-ct) \tag{3.41}$$

where $\sum''$ denotes trapezoidal-type summation with factor 0.5 of the first and last contributions and E_j is given by

$$E_j = {\sum_{m=0}^{N}}'' \zeta_m \cos\frac{jm\pi}{N} \text{ for } j = 1,\ldots,N \tag{3.42}$$

where ζ_m are the known surface elevation at discrete points m.

It should be noted that the truncation of the series for finite N is the only mathematical or numerical approximation in this formulation [28]. The required order N of the series can be decided from the relation between the wave height, the wave period and the water depth as seen in Figure 3.7.

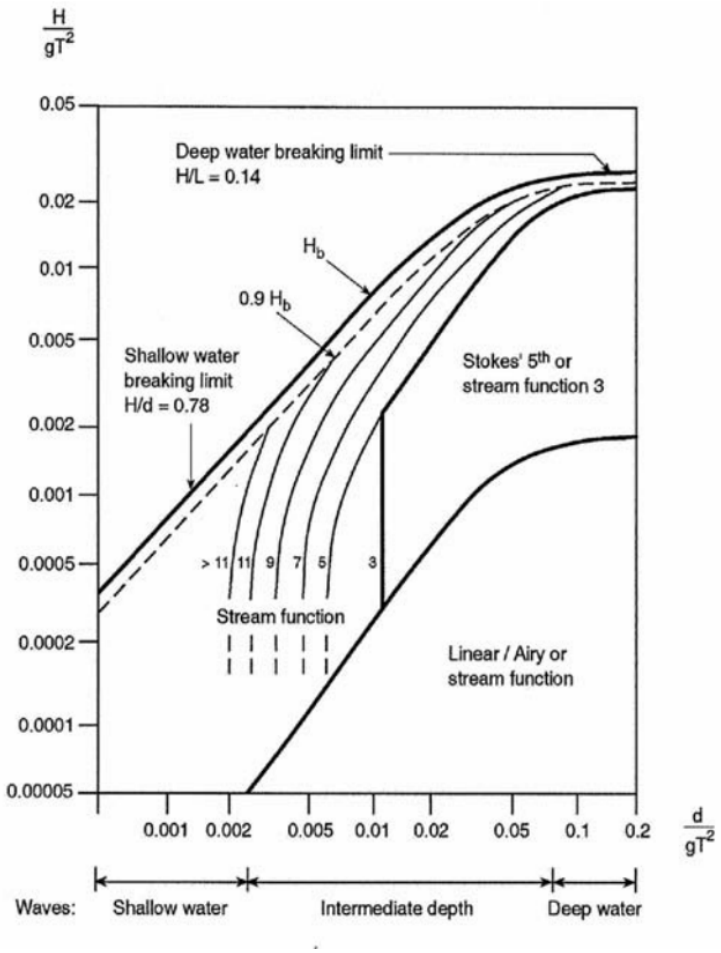

Figure 3.7: Required order, N, of stream function wave theory such that errors in maximum velocity and acceleration are less than one percent [17]

3.4.3 Comparison of non-linear wave theories

Different wave theories for modelling the wave elevation and the wave kinematics have been presented. The theories differ by their order; some require higher order to satisfy the dynamic and kinematic boundary condition at the free surface [5]. However, higher order will imply higher computational time. Both the Stokes theory and the stream function express the kinematics and wave elevation as series up to order N, where each additional harmonic term adds to the first basic harmonic term. One difference between these two theoires is that the stream function theory is formulated in therms of the stream function, while the Stokes theory uses the velocity potential. However, the stream function and the velocity potential are closely related [21].

In order to set the requirements of the wave theories into perspective, two different regular waves of steepness 1/40 and 1/22 are presented in Figure 3.8. The blue shaded area indicates a water depth of 27 meters and wave period in the range of $6.0 - 16.5$ seconds. Setting a requirement of a steepness of 1/40 results in the dark green area within the lighter green area. The waves of steepness 1/40, within the requirements set by the water depth and the wave period, would require a Stokes 5th order wave or a 3rd order stream function wave. In other words, the Stokes theory would be sufficient in this case. However, moving on to waves of the same periods and in the same water depth but this time with a steepness of 1/22, the Stokes 5th order wave no longer suffices. The longer waves in this range will require the stream function of 3rd, 5th and 7th order in order to achieve adequate accuracy.

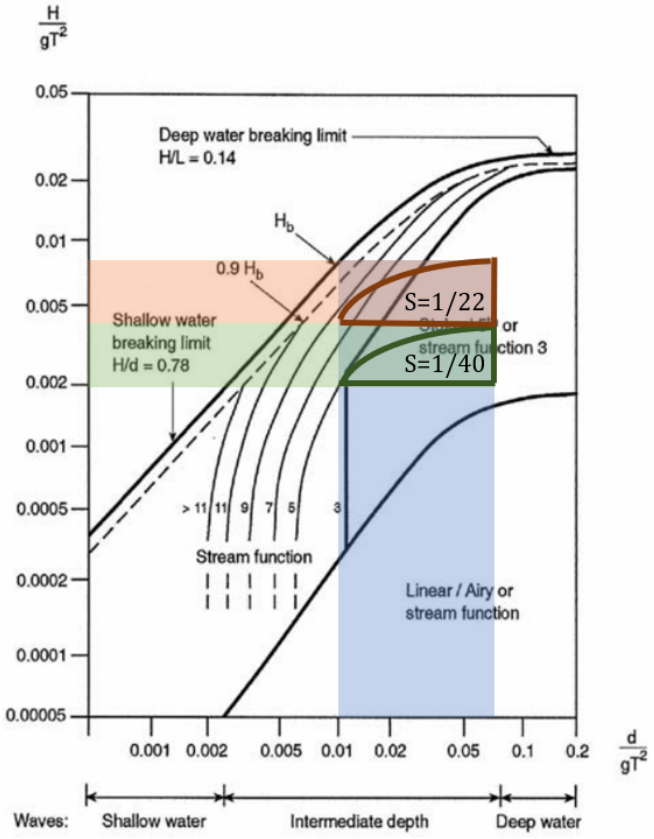

Figure 3.8: Comparison of wave theories with waves in water depth of 27 meters, with period ranging from $6 - 16.5$ s and steepnesses 1/40 and 1/22. Modified from Figure 3.7 [17]

The stream function theory therefore stands out as a flexible choice for the wave modelling, as it provides realistic reproduction of wave kinematics for a large range of relative water depths. The upper boundary of this theory is, as it is for all theories, the breaking wave height. In a slamming study presented by Burmester et al. in 2017, it was pointed out that implementing a stream function wave as an estimation of a breaking wave would result in significant discrepancy [12]. These differences would lead to discrepancies in the estimated quasi-static load, and in particular the wave steepness of a plunging wave was found to diverge from the measured wave. Burmester et al. concludes that the stream function theory is not sufficient for those kind of wave impacts. It will therefore be important to study the possible discrepancies between measured wave elevation and recreated stream function wave and consider the errors they may inflict on the results.

3.5 Breaking waves

When the wave becomes too steep, or when there are sudden changes in the sea bed, the wave breaks. The breaking limit is indicated in Figure 3.4. The breaking limit can also be found by

$$H_b = 0.142\lambda \tanh \frac{2\pi h}{\lambda} \tag{3.43}$$

where H_b is the breaking wave hegight, λ is the wave length and h is the water depth [17]. In shallow waters, the breaking limit can be estimated as $0.78h$, however, under idealized conditions the breaking limit can be even lower [17].

A breaking wave can be characterized by the shape of the breaker in relation to the slope of the sea bed. Generally, the breaker types can be classified by the non-dimensional parameter

$$\beta = \frac{H_b}{gT^2 m} \tag{3.44}$$

where m is the slope of the sea bed, H_b is the breaking wave height and T is wave period. When $\beta > 5$ the breaker is generally characterized as a spilling breaker. This type of breaker is often seen in deep waters or on beaches of gentle slopes [17]. For beach slopes of moderate steepness, with $0.1 < \beta < 5$, a plunging breaker can occur. A plunging breaker is characterized by its jet of water falling in front of the crest. For $\beta < 0.1$ a surging breaker occurs, generally when there is a steep beach with considerable reflection. The breaker types are illustrated in Figure 3.9.

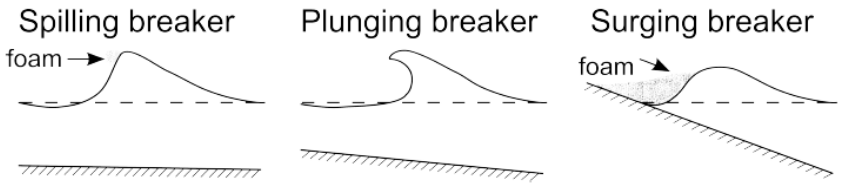

Figure 3.9: Definition of breaker types [12]

However, since the breaker type might as well differ from the range set by β parameter, the easiest and most accurate way to identify the breaker type is by visual inspection. In model tests such visual inspections can be done by eye or by video recordings.

3.6 Hydrodynamic load models

After calculating wave kinematics using a wave theory such as linear wave theory or stream function theory, a hydrodynamic load model can be applied in order to find the loading on the structure from the waves.

3.6.1 Morison's equation

The Morison equation is generally applicable when wave diffraction forces are negligible, i.e. the wave length must be larger than minimum 5 times the cylinder diameter, illustrated in Figure 3.10 [3]. In order to set these requirements into perspective, a cylinder of diamter 9 meter is used. Inserting $D = 9$ m into Figure 3.10 will result in mass forces dominating as long as the wave height is less than $H \approx 90$ m and a wave length greater than $\lambda \approx 45$ m or periods longer than $T \approx 5.5$ s.

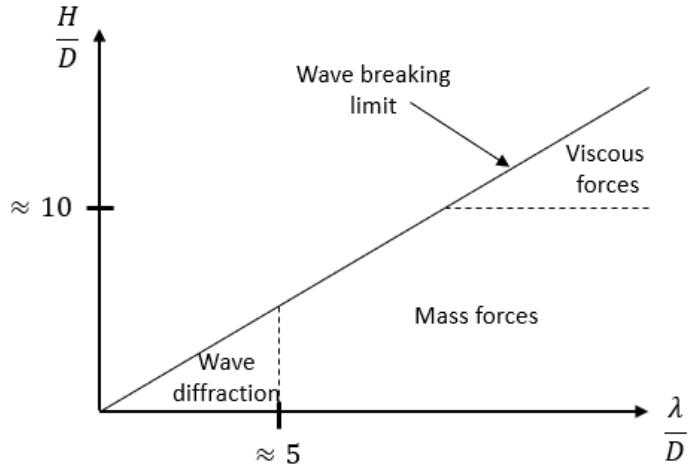

Figure 3.10: Relative importance of diffraction, inertia and viscous forces on marine structures [3]

For a cylinder subjected to hydrodynamic loading, the structure can be divided into sections of length dz, where the Morison's equation can be applied to find the hydrodynamic loads dF from both inertia forces and drag forces by

$$dF = \rho C_M \frac{\pi D^2}{4} \dot{u} dz + \frac{1}{2} \rho C_D D u|u| dz \tag{3.45}$$

where ρ is the water density, C_M and C_D are the inertia and drag coefficients, D is the cylinder diameter, u is the horizontal particle velocity and $\dot{u}$ is the horizontal particle acceleration [29]. The first term, often called the mass force, includes contributions from Froude-Krylov and diffraction forces. For $C_M = 2.0$, the potential theory is fulfilled, and half of the contribution will be from Froude-Krylov while the other half will be diffraction force. However, if viscous effects are accounted for, ie. the drag force is included, C_M will generally differ from 2 [3]. The coefficients C_M and C_D depend on many different parameters, such as the Reynolds number, the Keulegan-Carpenter (KC) number and the surface roughness number and must be determined empirically.

In the so-called common version of Morison's equation $\dot{u} = \delta u/\delta t$. By replacing $(\delta u/\delta t)$ with the total advection term $(\delta u/\delta t + u\delta u/\delta x + w\delta u/\delta z)$, modified Morison's equation is introduced.

3.6.2 FNV model

The FNV model, named after authors Faltinsen, Newman and Vinje, was first reported in 1995 [14]. The model was developed by analytic studies of ringing loads on a fixed, non-moving surface piercing cylinder subjected to incident waves in deep waters. Originally, regular waves were considered, but in 1996, Newman extended it to irregular waves. In 2017, Kristiansen and Faltinsen further generalized the model to be valid in finite water depth [15]. The generalization of the FNV model also leads to the possibility of combining it with higher order wave theory of numerically calculated wave kinematics, including irregular waves. In the study presented in 2017, the FNV model is combined with third and fifth order Stokes wave theory.

The generalized FNV theory from 2017 is based on the original FNV theory from 1995. The new generalized version is valid for both deep and finite water depths. One important difference of deep and finite water depths is that the third-order incident potential is zero for deep water depths while it is a dominant contributor to the third harmonic load in finite water depths [15]. The third harmonic loads where predicted by the FNV model corresponded well to the experiments for small to medium steep waves. For steeper waves, the theory overpredictes. The FNV model is not valid for breaking waves.

The total potential is defined as $\varphi = \varphi_I + \varphi_s + \psi$, where $\varphi_D = \varphi_I + \varphi_s$ is the diffraction potential whom which satisfies the two-dimensional Laplace equation. The three-dimensional Laplace equation and approximate free-surface condition to the third order are satisfied by the third order potential ψ. The incident wave potential is given by φ_I. The total horizontal load can then be expressed as a modified form of the Morison equation

$$F_x = \int_{-h}^{\zeta_l} F'(z,t)\mathrm{d}z + F^{\psi} \tag{3.46}$$

where the distributed load term F' due to φ_D is integrated from the sea bed $(-h)$ up to the incident free surface (ζ_I). The distributed load term is given as

$$F'(z,t) = \rho\pi a^2 \left(\frac{\partial u}{\partial t} + u\frac{\partial u}{\partial x} + w\frac{\partial u}{\partial z}\right) + a_{11}\left(\frac{\partial u}{\partial t} + w\frac{\partial u}{\partial z}\right) \quad \text{for } h \leq z \leq \zeta_I \tag{3.47}$$

where a is the radius of the cylinder, ρ is the density of water and a_{11} is the 2D added mass in surge. The incident wave potential, φ_I, is used to define $u = \partial\varphi_1/\,\partial x|_{x=0,}$, $\partial u/\partial x = \partial^2\varphi_1/\,\partial x^2\big|_{x=0}$ and $w = \partial\varphi_l/\,\partial z|_{x=0}$. The second term in Equation 3.46 is found as

$$F^{\psi} = \rho\pi a^2 \frac{4}{g} u^2 \frac{\partial u}{\partial t} \tag{3.48}$$

which is the same as the original FNV theory.

3.6.3 Wienke's slamming model

In order to account for slamming, a slamming model must be added to the Morison equation. One such model is the Wienke's model [8]. The Wienke's model is formulated as

$$F_{\text{slam}} = C_s \rho R c^2 \lambda_c \eta_b \tag{3.49}$$

where C_s is the slamming coefficient, R is the radius of the cylinder, c is the wave celerity, λ_c is the curling factor and η_b is the maximum wave elevation for the given slamming event, taken as the breaking wave elevation [8]. The time of impact is defined as the moment when the wave hits the upstream side of the monopile.

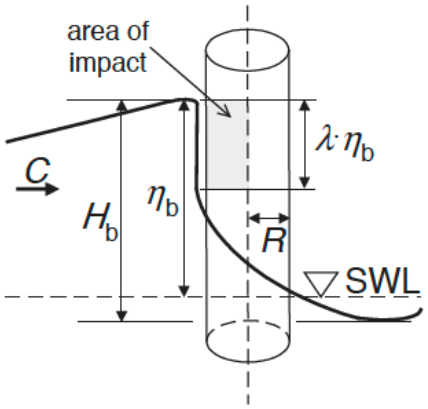

Figure 3.11: Definition of wave impact by Wienke [8]

The impact time of the slamming load is defined by Wienke as

$$T = \frac{13}{32}\frac{R}{c} \tag{3.50}$$

where once again c is the wave celerity given by the stream function theory.

The slamming coefficient C_s is time dependent [8]. When $0 < t < \frac{1}{8}\frac{R}{c}$ the slamming coefficient is given as

$$C_S = 2\pi - 2\sqrt{\frac{c}{R}t}\,\text{arctanh}\left(\sqrt{1 - \frac{1}{4}\frac{c}{R}t}\right) \tag{3.51}$$

If $\frac{3}{32}\frac{R}{c} \leq t' \leq \frac{12}{32}\frac{R}{c}$ where $t' = t - \frac{1}{32}\frac{R}{c}$, then the slamming coefficient is given as

$$C_S = \pi\sqrt{\frac{1}{6}\frac{1}{\frac{c}{R}}t'} - \sqrt[4]{\frac{8}{3}\frac{c}{R}t'}\,\text{arctanh}\left(\sqrt{1 - \frac{c}{R}t'\sqrt{6\frac{c}{R}t'}}\right) \tag{3.52}$$

3.6.4 WiFi formulation

The WiFi formulation is, similarly as the Wienke slamming model, an addition to the quasi-static force calculated by the Morison equation to account for slamming. The Wifi formulation is based on DNV-RP-C205 [17], and the preliminary formulation is given as

$$F_{slam} = \frac{1}{2}\rho_w(1.2 \cdot c)^2 C_S \left(0.25 \cdot H_b 2\pi \frac{R}{8}\right) \tag{3.53}$$

where the slamming coefficient is set as $C_s = 2\pi$ [12]. The wave celerity is here defined as $c = \frac{L_b}{T_b}$. The breaking wave period is found using the peak period of the wave spectrum $T_b = 0.9 \cdot T_p$, while the breaking wave length is given by the linear dispersion relation. The breaking wave height is then defined as

$$H_b = \min\left(1.4 \cdot H, 0.78 \cdot d, L_b \cdot 0.142 \cdot \tanh\left(\frac{2\pi d}{L_b}\right)\right) \tag{3.54}$$

3.6.5 Comparison of load models

In the previous sections, different hydrodynamic load models has been presented. If one considers the slender, flexible monopile structure up against the load models, one can do evaluations of which load model would be applicable in different cases. In Figure 3.12 the Morison load model and the finite depth FNV model are illustrated. The different arrows represents the area of application of the different methods, not the amplitude of the load. In Figure 3.12a the Morison model is applied with both linear wave kinematics (ML) and non-linear, stream function wave kinematics (MSF). The linear wave kinematics are only valid up to mean water level, and would require stretching of the velocity potential in order to be integrated up to the actual wave surface. However, in order to keep the model completely linear for comparison with the other models, stretching of the velocity potential is not applied. In Figure 3.12b the FNV model is illustrated with kinematics valid all the way to the actual wave surface, in this case by application of stream function wave kinematics. The distrucuted force term F' is indicated by light green arrows, while the point load F^{ψ} is represented by the dark green arrow.

Mockutè et al. presented a study in 2019 of a range of wave kinematics and hydrodynamic load models for slender cylinders, such as the monopile foundation structure [30]. The wave kinematics and the loading models were compared over a range of nonlinear wave conditions (such as steep waves and intermediate water depths) and for different cylinder radiuses. Further on, the wave-loading model combinations were assessed and compared to experimental data. It was found that overall, the finite-depth FNV model captured the loading for the widest range of the wave and cylinder conditions. It was found that loading from waves of large steepness were poorly predicted by the numerical models, and that the wave number for second harmonic and the vicinity of the wave-breaking limit for the third harmonic also were not predicted accurately.

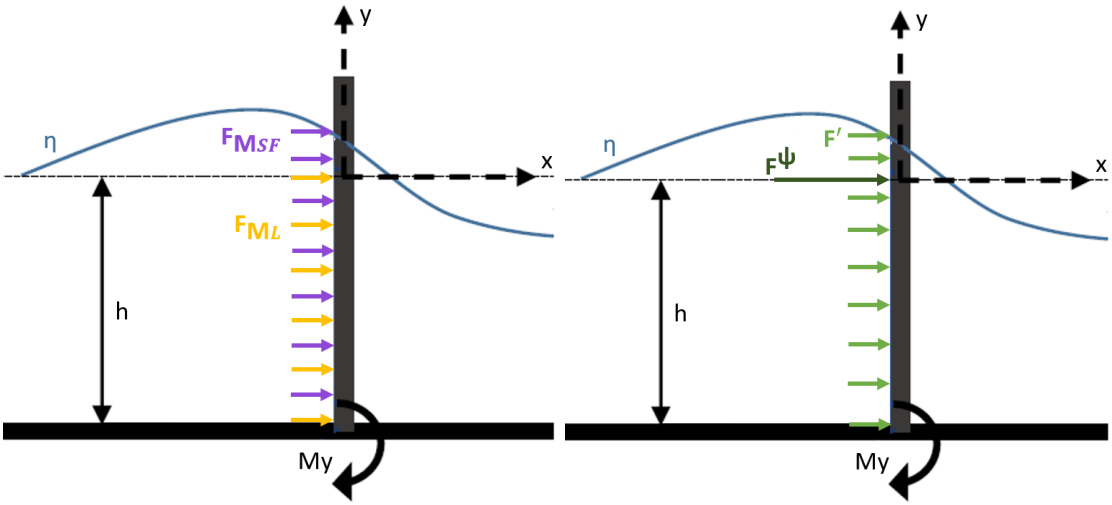

(a) Morison model (b) FNV model

Figure 3.12: Coordinate system and the implemented hydrodynamic loading model components of: (a) Morison equation with linear kinematics (ML) and stream function kinematcs (MSF); (b) FNV theory integrated term F' and point load at mean water level F^{ψ}.

To account for breaking waves causing slamming loads, a slamming model must be added. In the previous sections, two such models were presented; the Wienke's slamming model and the WiFi formulation. As mentioned in the literature review, Burmester et al. presented the WiFi formulation and conducted a comparison of the Wienke's slamming model [12]. The comparison indicated that Wienke's slamming model was the most suited to estimate the slamming load. However, for spilling breakers both the slamming models would agree well with the measurements. For plunging, and especially late plunging breakers, the WiFi formulation will underestimate the maximum impact load. It was found that the duration adopted from Wienke's slamming model in the WiFi formulation is too short in comparison with the experimental data.

3.7 Response of a monopile structure

The first thing to identify when analysing the response of a monopile structure, is the eigenfrequencies and eigenmodes. For a general structure, the lowest eigenmodes is generally the most important. In order to calculate the eigenfrequency, a monopile structure with a turbine on top can be simplified as a 1-DOF system, illustrated in Figure 3.13.

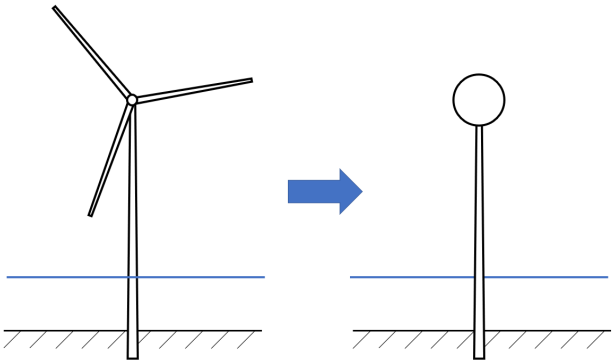

Figure 3.13: Simplification of the monopile wind turbine to a 1-DOF system

The first eigenfrequency can then be estimated by

$$\omega_n = \frac{1}{2\pi}\sqrt{\frac{k}{m}} \tag{3.55}$$

where k is the bending stiffness and m is the mass, often only the mass in top. This is derived from the equation of motion, which for a monopile structure can generally be written as

$$M\ddot{x} + C\dot{x} + Kx = Q(t) = F_0 \sin \omega t \tag{3.56}$$

where M is the mass term, $\ddot{x}$ is the acceleration, C is the damping term, $\dot{x}$ is the velocity, K is the stiffness term, x is the position and $Q(t)$ is the external forces, such as for example wind and wave loading.

The two first mode shapes of a monopile wind turbine can be seen in Figure 3.14. The blue curve is the first mode shape of the structure, and is related to the first eigenfrequency. The orange curve is the second mode shape, which corresponds to the second eigenfrequency.

The corresponding eigenfrequencies can be found by performing a decay test of the model. The first eigenmode (the blue one in Figure 3.14) can be found by applying a load on top of the structure, and then releasing it, letting the structure oscillate freely. The eigenfrequency will then be the inverse of the period of oscillation. The same can be done to find the second eigenfrequency, however, this time applying the load on the middle of the structure to excite the second eigenmode. One way of identifying the eigenfrequencies directly from the time series, is to apply Fast Fourier Transformation (FFT). This will return the frequencies present in the time series, and the first and second eigenfrequencies will appear as peaks.

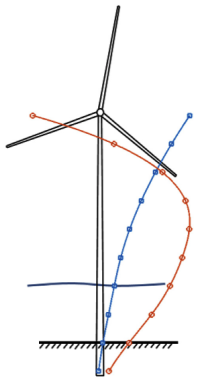

Figure 3.14: Two first bending modes of a monopile wind turbine [5]

The dynamic response of the offshore wind turbine can be described by the dynamic amplification factor DAF

$$DAF = \frac{u}{u_0} \tag{3.57}$$

where u is the steady state dynamic response to a harmonic load and u_0 is the static response. In Figure 3.15 the DAF is shown for different levels of damping as a function of the frequency ratio ω/ω_n. The dynamic amplification reaches its maximum when the excitation frequency ω is equal to the eigenfrequency of the structure ω_n. Increasing damping ratios ξ causes reduction of the DAF [31].

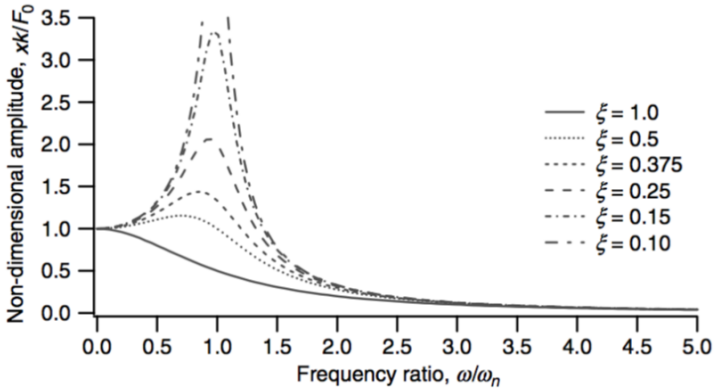

Figure 3.15: Dynamic amplification factors for different damping levels [31]

When the duration of the external load is of the same order of magnitude of shorter than the natural period of the structure, the load is a so-called impulsive load [32]. Slamming loads are one such type of impulsive load. In Figure 3.16 the impulse load is given as the solid line. The duration of the impulse load t_1 is much shorter than the period of free oscillation T. The duration of the impulse $0 < t < t_1$ is called phase 1 while $t > t_1$ is phase 2. For impulse duration of $t_1 > 0.5T$, the maximum response will occur in phase 1, and the DLF will normally be in the range $1 <= DLF <= 2$. For impulse duration of $t_1 < 0.2T$, the maximum response will always occur in phase 2.

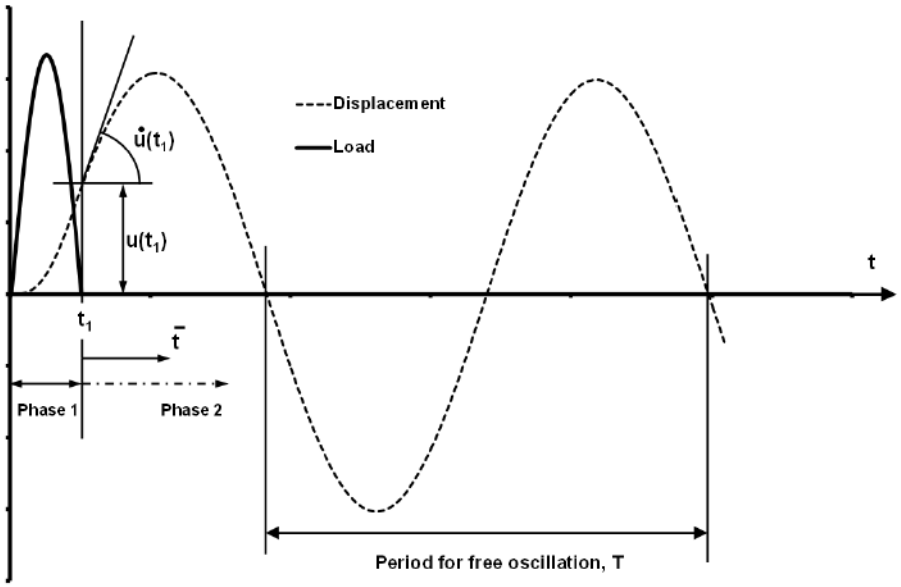

Figure 3.16: Response to an impulsive load [32]

3.7.1 Damping

A monopile foundation has multiple sources of damping, namely structural, aerodynamical, hydrodynamical and soil damping. The damping ratio ξ can be defined as $\xi = c/c_{cr}$, ie the ratio between the damping and the critical damping. The damping ratio can be estimated from decay tests using

$$\xi = \frac{1}{2\pi n} \ln\left(\frac{u_i}{u_{i+n}}\right) \tag{3.58}$$

where ξ are the damping ratio, n are the number of periods and u is the amplitude of oscillation [**?**]. In order to identify the linear and quadratic damping contributions from the decay test, another method can be applied. This methods assumes that the damping is constant with regards to the amplitude of oscillation, and is given by

$$\frac{2}{T_m} \log\left(\frac{X_{n-1}}{X_{n+1}}\right) = p_1 + \frac{16}{3}\frac{X_n}{T_m} p_2 \tag{3.59}$$

where X_n is the amplitude of the n-th oscillation, T_m is the period of oscillation and p_1 and p_2 are linear and quadratic damping, respectively [3]. The linear and quadratic damping terms can be found by plotting the left side of equation 3.59 versus $\frac{16}{3}\frac{X_n}{T_m}$ and applying the least square method to fit a straight line to the points.

If the empirical damping known, the structural damping of a fixed structure can be modelled by Rayleigh damping [**?**]. In the Rayleigh damping model, the damping matrix C is established as a linear combination of the mass M and the stiffness K matrices

$$C = \alpha_1 M + \alpha_2 K \tag{3.60}$$

where α_1 will be the mass damping coefficient and α_2 the stiffness damping coefficient [33]. The damping coefficients can be found using the damping ratio

$$\xi_i = \frac{1}{2}\left[\frac{\alpha_1}{\omega_i} + \alpha_2\omega_i\right] \tag{3.61}$$

and solving the equation set for $i = n, m$ as illustrated in Figure 3.17. If $\alpha_1 = 0$, the damping ratio is proportional to the frequency ω and there will be only stiffness proportional damping. If $\alpha_2 = 0$, the damping is mass proportional and the damping ratio will be inversely proportional to the frequency ω. The mass damping coefficient α_1 will damp out the lower mode shapes, while the stiffness damping coefficient α_2 will damp out the higher mode shapes.

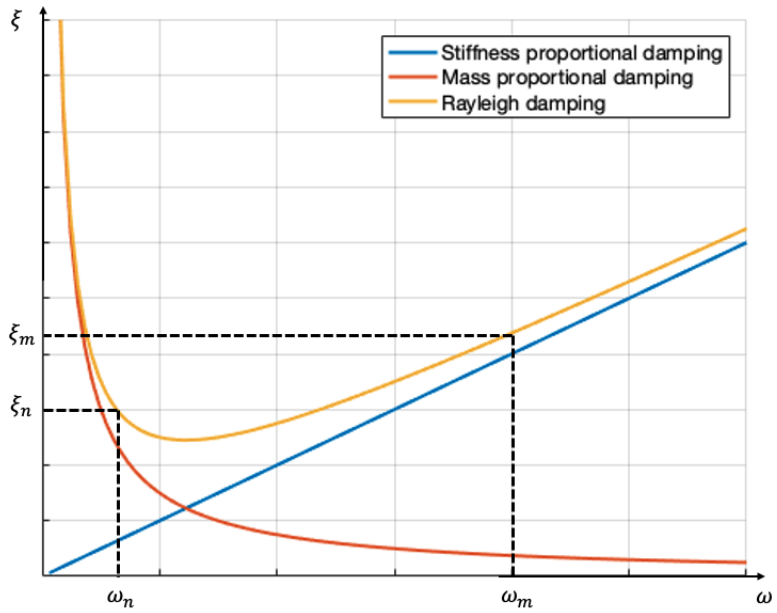

Figure 3.17: Rayleigh damping

3.8 Principles of model testing and scaling

When performing model tests, the goal is to represent the full scale system as close as possible. This is done by introducing scaling laws [34]. In order to achieve similarity in forces between the model and the full scale measurements, three different conditions presented below must be fulfilled.

Geometrical similarity
Geometrical similarity implies that the model and the full scale structure have the same shape, ie. there exist a constant relation between all lengths $\lambda = L_F/L_M$. Note that here λ is used as scaling coefficient, not the wave length. This relation must be valid for all structural dimensions and the surrounding environment, such as water depth and wave length.

Kinematic similarity
Kinematic similarity implies that the ratio between velocities in model scale must be equal to the ratios between velocities in full scale. This further means that the flow will undergo the same relative geometrical motions in both cases.

Dynamic similarity
Dynamic similarity means that the ratio of different force contributions are the same in model and full scale measurements.

Different scaling laws are introduced in order to approximately achieve similarity. One such scaling law is Froude scaling. By achieving geometrical and kinematic similarity and forcing equality in Froude number, the ratio of inertia and gravity forces in model and full scale will be similar.

The ratio between inertia and gravitational forces are given as

$$\frac{F_i}{F_g} \propto \frac{\rho u^2 L^2}{\rho g L^3} = \frac{u^2}{gL} \tag{3.62}$$

By applying this ratio to the model and full scale, the Froude number F_N is achieved as

$$F_N = \frac{u_M^2}{gL_M} = \frac{u_F^2}{gL_F} \tag{3.63}$$

where M implies model scale and F implies full scale [34]. Froude scaling is generally applicable when gravitational effects dominate, while viscosity, surface tension and roughness are negligible. An important aspect of the Froude scaling is that the accelerations are the same in model and full scale. Froude scaling is generally applied when testing in waves, as gravity forces will be governing [34]. The wave height will be scaled with the scale ratio and the wave periods will be scaled by the square root of the scale ratio.

While the Froude number F_N conserves the ratio between inertia and gravitational forces, the Reynolds number Re preserves the ratio between inertia and viscous forces:

$$\frac{F_i}{F_v} \propto \frac{\rho u^2 D^2}{\mu u D} = \frac{\rho u D}{\mu} = \frac{uD}{\nu} = Re \tag{3.64}$$

where $\nu = \mu/\rho$ is the kinematic viscosity [34]. Equality in Reynolds number in model scale and full scale causes the viscous forces to be scaled correctly. As the flow velocity in the model scale is much lower than the full scale flow velocity, similarity in Reynolds number is not possible. However, as the drag coefficient C_D in addition to Re is dependent of, amongst others, the surface roughness, additional surface roughness of the model can be introduced to compensate for the difference in scale. If the conditions are mass dominated, viscous effects are often much smaller than inertia effects, and the difference in Reynolds number is in those cases often neglected.

There are additional scaling requirements for when the hydrodynamic forces are influenced by elastic deformation [34]. Correctly scaled elastic behavior of the model will be important when looking at phenomenons such as ringing and springing. There are three additional requirements for the elastic model. The first one is that the global structural stiffness must be scaled correctly. Secondly, the model scale structural damping must be similar to those of full scale. Finally, the mass distribution in model scale must be similar to the full scale mass distribution.

4 Method

This section explains how the measured data were obtained through an experiment, how the data have been processed and how input for the numerical model was obtained. It is split into two main chapters, where the experimental method and processing are presented first before moving onto the numerical method.

4.1 Experimental setup

The experimental data used in this report were obtained through the second phase of model tests for the WAS-XL project. The tests were performed in the small towing tank "Lilletanken" at NTNU in June 2019 [2]. The tank consists of a piston wavemaker at one end and a parabolic beach at the other. The model test setup with associated wave probes can be seen in Figure 4.1.

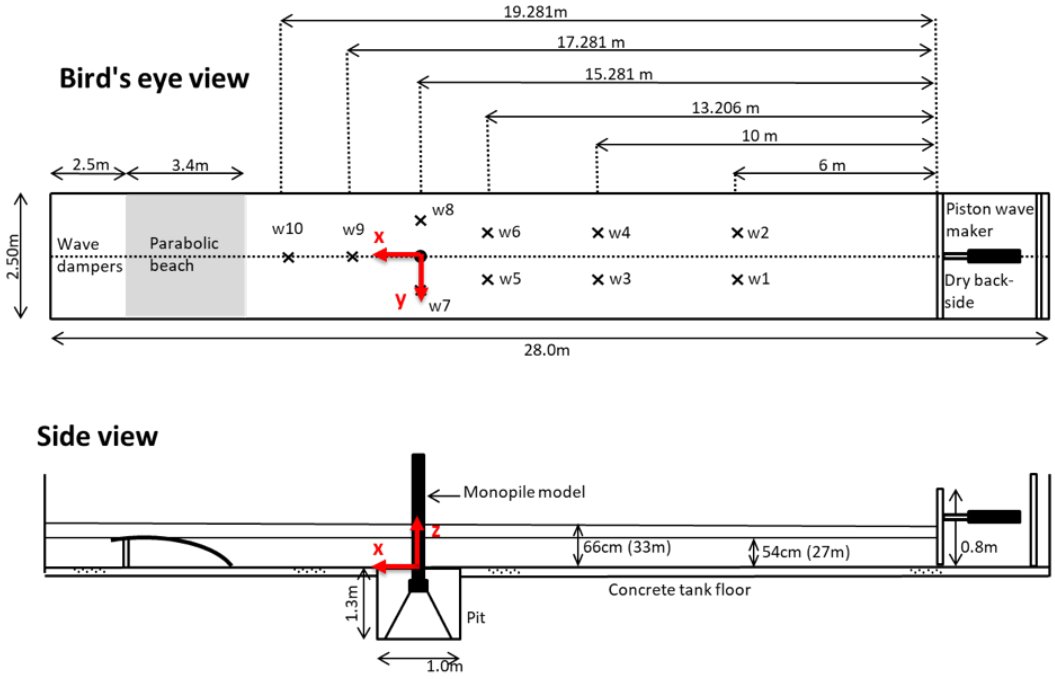

Figure 4.1: Model test setup in model scale. Wave gauges are marked with "w". Some selected full scale parameters are given in parentheses [2]

The Froude scaling factor is 50. This corresponds to a full scale water depth of 27 meters. All results obtained from the experiment have been up-scaled to match results from full scale measurements according to Froude scaling unless otherwise stated. A sampling frequency of 200 Hz was used, resulting in a full-scale time step of $dt = 0.0353$ s in the measurements. Three different models were tested, all with a diameter of 9 meters:

- Model 1: Rigid model made from a single metal tube to measure global wave loads
- Model 2: Rigid, segmented model with many load sensors to measure both local and global wave loads
- Model 3: Flexible model to measure the model response

4.1.1 The model

For the purpose of this thesis, only the flexible model is considered. This model consists of an inner elastic backbone column and a smooth outer shell to model the correct hydrodynamic diameter. The model has a diameter of 9 meters and total height from seabed to top of rotor nacelle assembly (RNA) of 151.45 meters. The model without the RNA on top has a mass of $2.652e6$ kg and a center of gravity 34.25 meters above the seabed. The mass of the RNA is artificially set to $9.55e5$ kg to achieve a good match of the first eigenfrequency [2]. The model reaches below the tank floor, where it is eventually fixed. The model is instrumented with both accelerometers and strain gauges, which can be seen in Figure 4.2. The strain gauges were glued on the inner backbone column to measure the strain, which is used to estimate the bending moment response [2].

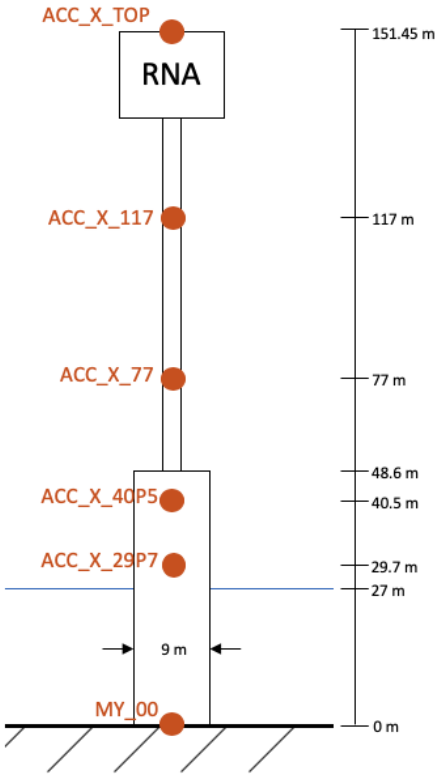

Figure 4.2: Model dimensions and instrumentation (only the relevant instrumentation is shown)

4.1.2 Regular wave tests

The regular wave tests were done with a flat seabed with water depth of 27 meters. Five different steepnesses ($s = H/\lambda$) were tested; 1/40, 1/30, 1/25, 1/22 and 1/20. For each steepness 22 different wave periods (T) were run, ranging from 6 s to 16.5 s with interval of 0.5 s. This implies that the waves will all be in the range of intermediate water depth $1/20 < h/\lambda < 1/2$. Two different steepnesses were selected for consideration, namely $s = 1/40$ and $s = 1/22$.

4.1.3 Irregular wave tests

For generation of the irregular sea state, the JONSWAP wave spectrum was used and the significant wave height H_s and peak wave period T_p were chosen from the 50-year contour line [2]. Three different sea states from the 50-year contour line was tested. The full-scale duration of each test run was 3 hours, including a sigmoid ramp of $10 \cdot T_p$ at the start-up and shut-down of the wave piston. In this report, only one sea state is considered. The chosen sea state is the one where the largest response was observed. The parameters of this test can be seen in Table 4.1.

Table 4.1: Description of test

h [m]	**T_p [s]**	**H_s [m]**	**Seeds**
27	11	8.6	201-220

4.2 Processing experimental data

The result files from the experiment are provided as binary files (.bin). Each bin file contains the entire test run, in other words, covering the full run time including all seeds. In order to make these files more manageable, they are split into several MATLAB files (.mat). These processed files contain only the relevant data from the binary file. In addition, they are split into each seed, such that one result file only contains the relevant data from one seed.

For each test run, there is also an associated wave calibration test. This is a test with the same input parameters as the test run, only without the model present. The seed files from the model test therefore need to be synchronized with the wave calibration seed files. This is done by looking at the flap position of each corresponding tests. The flap position is given as an input to the wavemaker, and should therefore be the same when the input values, such as the wave parameters and seed number, are the same.

In addition, each test run contains a corresponding video. Each video contains the entire test run. The timestamp of the video differs from the timestamp of the time series from the measurements in the experiments, and some investigation and synchronization have been done in order to match the correct events in the measurements with the video.

4.2.1 Identifying events

In the process of identifying events in the irregular sea state to study further, different selection criteria were used. Time series of accelerations at the top of the model was looked into, and events with high acceleration were investigated. The moment in the base was also checked to see if the same events would appear. Lastly, videos of the tests were investigated in order to characterize whether or not slamming and/or breaking was present.

One example of how the events are identified is given for seed 201 in Figure 4.3. The same six events are identified from both the accelerations on top of the model and from the bending moment at the model base. The events may be easier to identify from the accelerometer, however, when filtering and analyzing the response, the bending moment in the base is focused upon.

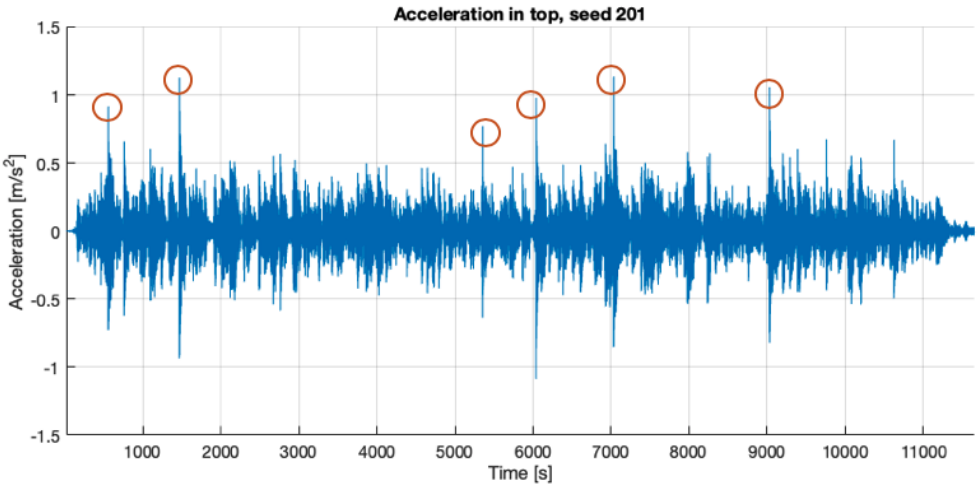

Figure 4.3: Identification of events in seed 201 marked with orange rings

4.2.2 Band pass filtering of time series

Bandpass filtering of time series implies transforming the data from the time domain to the frequency domain, then filter out unwanted frequencies and then transforming it back to the time domain. This is useful for example when we have both first and second mode excited in a decay test. Bandpass filtering using the second eigenfrequency will then return mainly the second eigenmode response. However, all modes are responding in all frequencies, the filtering returns mainly the response due to resonance of that particular mode, but will also contain some contributions of the other modes.

After identifying the first and second eigenfrequency of the model, the contributions from the first and second mode can be filtered from the total response. This is done by performing a bandpass filtration in MATLAB. The bandpass function is set to filter only the eigenfrequency f_0 with a sensitivity of $\pm 0.1 \cdot f_0$. This way, by setting the eigenfrequency to the first eigenfrequency, the bandpass filtration will return mainly the contribution to the response from the first mode. The same operation is performed to return the contribution from the second mode from the total response. The residue of the total response after subtracting the contribution from the first and second mode is said to be the quasi-static response. Bandpass filtering is also used to remove drift of measured data, meaning that very low frequencies are removed from the time series, correcting any drift of wave elevation etc.

4.2.3 Steepness of irregular waves

For irregular waves, a new definition of wave steepness is introduced in order to describe the steepness of a single wave in an irregular sea state. The wave steepness is now characterized as the time derivative of the wave elevation evaluated at $\zeta = 0.66\zeta_{max}$ prior to the crest, i.e. when the wave elevation is at 66% of its maximum value [35]. The wave steepness will have the dimension m/s, while for regular waves steepness is dimensionless.

In Figure 4.4, the steepness calculation is illustrated. The blue curve is the wave elevation, while the red curve is the time derivative of the wave elevation. The derivative is to be evaluated at 66% of the maximum wave elevation, marked with the dashed line.

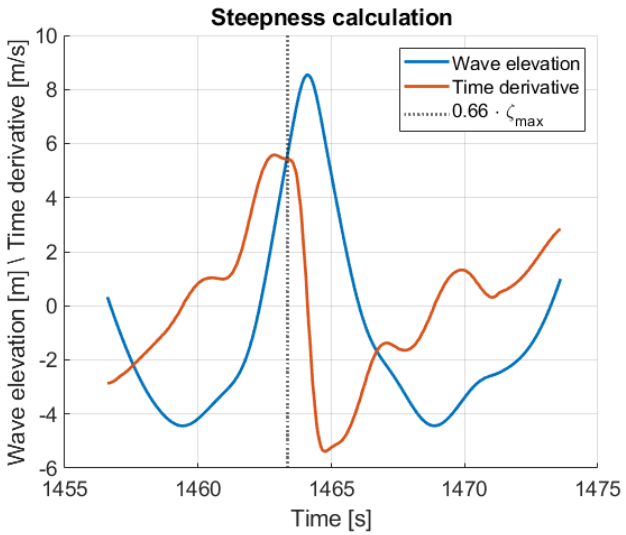

Figure 4.4: Calculation of wave steepness

4.3 Numerical modelling

The numerical modeling is performed in RIFLEX in SIMA. RIFLEX is a tool for static and dynamic analysis of slender marine structures, while SIMA is the workbench from which RIFLEX is ran [36]. The model is modeled as the physical model used in the experiment by Dr. Maxime Thys, and can be seen in Figure 4.5. In order to contain both the flexibility and the mass distribution of the physical model, the numerical model is made up of elements of different length, stiffness and mass. The soil connection is modeled by two different line types, where one is more flexible and the other has a higher bending stiffness to simulate the physical setup. The physical model has a damping device at the top where the turbine normally would be, while in the numerical model the damping is distributed along the length of the model.

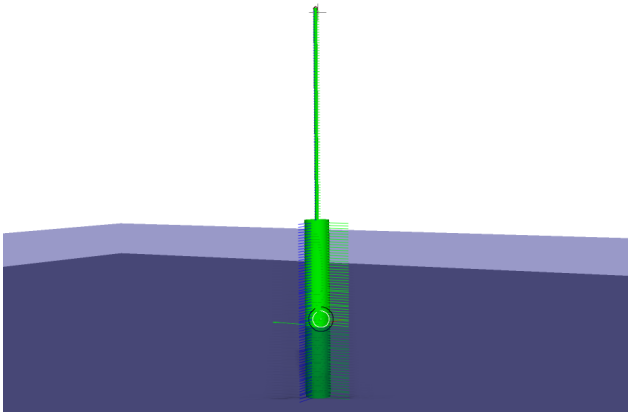

Figure 4.5: Numerical model in SIMA

In order to calculate the response in RIFLEX, two different approaches are used. The first approach used is to give the nodal loads as input. This is done by calculating the loads in MATLAB, and then assigning them to the nodes defined in the numerical model. The loads are written into ASC files, which are then given as input to RIFLEX. RIFLEX will then calculate the response.

Figure 4.6: Nodal loads given as input to RIFLEX to calculate the response

The second approach is to give the wave elevation as input to RIFLEX. The wave elevation from the experiment is linearized before given as input, due to RIFLEX treating the wave elevation as linearized.

Figure 4.7: Wave elevation given as input to RIFLEX to calculate the response

The result files from the simulations are written in time steps of $dt = 0.05$ s. The experimental data is therefore resampled to obtain the same time step for comparison with the numerical data.

4.3.1 Regular waves

For the regular waves, two different methods are tested: Morison method and generalized FNV theory. First, Morison equation with linear wave kinematics is tested in order to have a fully linear basic calculation to compare the non-linear results with. Further, stream function kinematics are implemented according to Rienecker & Fenton, resulting in valid wave kinematics all the way up to the actual wave surface. For both implementations of Morison, $C_M = 2$ and $C_D = 1$ are used. The generalized FNV theory is also implemented using stream function wave kinematics. The scripts used for the implementation of these methods can be found in the Appendix E.

Lastly, the wave elevation is given as an input to RIFLEX. RIFLEX applies the Morison equation with second order wave elevation with wave forces integrated to the wave surface. In this implementation, $C_M = 2$ and $C_D = 0.9$ are used by RIFLEX, meaning that the drag coefficient C_D deviates from the other implementations. However, since the system is highly mass dominated, this deviation will not have a noteworthy influence.

4.3.2 Irregular waves

In order to be able to calculate the wave loads of the irregular sea state, the waves are linearized [37]. This implies that the sea state can be composed by regular waves of many frequencies. This method is assumed to be fairly accurate as long as the waves are not too steep. However, in order to include extreme waves, a regular wave can be inserted. For regular waves, near exact computational methods can be used, such as the stream function theory. Both of these methods are applied to the measured wave elevation to be able to model the irregular sea state.

First, the measured wave elevation of the irregular wave tests is linearized to obtain linear stochastic waves. This is done as by Suja-Thauvin's wave linearization procedure [5]. For simplicity, the sampling frequency was set to 2 in this process, meaning that the linearized output has a time step of $dt = 0.0707$ s, which should still be sufficient for calculation of the excitation force while saving some computational effort. In order to determine the best filter to apply for linearizing the spectrum, the procedure compares the reconstructed 2nd order wave spectrum with the measured wave spectrum, as seen in Figure 4.8. Difference frequency is removed using a high-pass filter. The upper cut off frequency must be carefully evaluated, as the second order sum-frequencies will lie within the range of the linear waves [5]. After the high and low pass filters have been applied, an initial approximation $\zeta_{init}^{(1)}$ of the wave elevation is obtained. However, this approximation will contain some of the second order waves. The second order wave is therefore estimated from the initial approximation of the linear wave:

$$\zeta_1^{(2)} = -\frac{1}{g}\left[\frac{1}{2}\left(u^2 + w^2\right) + \zeta_{init}^{(1)} w_t\right] \tag{4.1}$$

where $\zeta_1^{(2)}$ is the second order wave, g is the gravitational acceleration, u and w are the particle velocities.

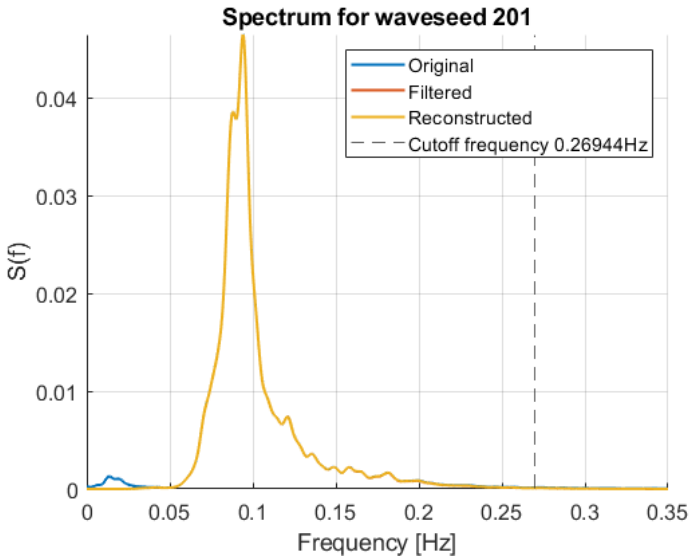

Figure 4.8: Linearization of measured wave elevation for wave seed 201

When obtaining kinematics from the linearized stochastic sea, a cut-off frequency should be applied [5]. This must be done because some kinematics used in non-linear hydrodynamic models can become unphysically large at the tail of the used wave spectra [38]. For deep water, this cut-off frequency is specified in the standard DNV-RP-C205 as

$$\omega_{DNV} = \sqrt{\frac{2g}{H_S}} \tag{4.2}$$

where the ω_{DNV} will be found in rad/s by the significant wave height H_S [17]. However, for intermediate water depths Suja-Thauvin and Krokstad in 2016 found that a cut-off frequency of $\omega_{cutoff} = 0.8 \cdot \omega_{DNV}$ gave the most accurate results [39]. The results are very sensitive to the cut-off frequency selected and uncertainties in the estimation of the input to the hydrodynamic models will be introduced. However, as pointed out by Suja-Thauvin [5], they will not affect the generation of the stream function wave or the Wienke slamming model. The stream function wave input is taken from the unfiltered wave elevation (the wave height and wave period), while the Wienke slamming model is only dependent on the wave elevation and the celerity from the stream function wave.

When the linear stochastic sea is obtained, some of the extreme waves have been degraded. To correct for this, a stream function wave is embedded into the linear stochastic sea state to achieve accurate wave kinematics around the extreme wave [37]. One such embedding can be seen in Figure 4.9. The stream function wave is generated by Fenton's own code, available on his home page [40].

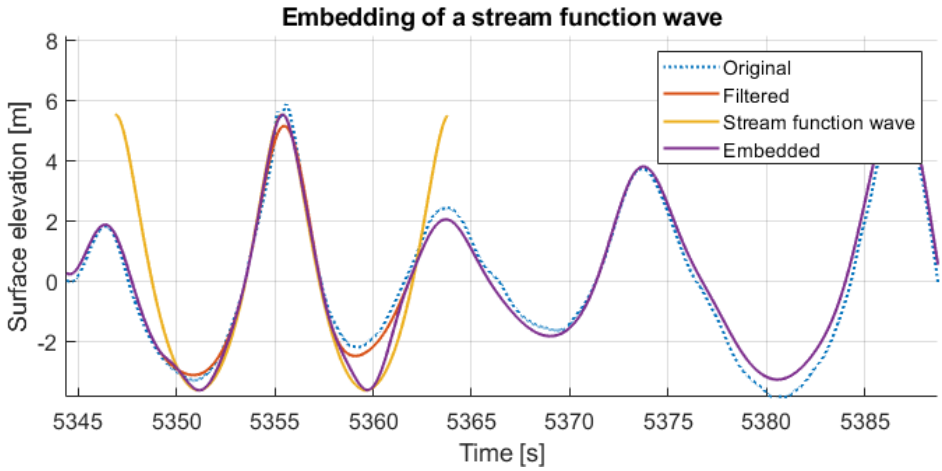

Figure 4.9: Embedding of the stream function wave into the linear stochastic sea

The blending parameters for embedding the stream function solution with the linear stochastic sea are given in Table 4.2. The blending parameter is a function of the time t, the time of the constrained peak T_0 and the period of the extreme wave T.

Table 4.2: Blending parameters [37]

Time	**Stream-function**	**Stochastic time history**
$\lvert t - T_0 \rvert > 0.75 \times T$	0	1
$0.5 \times T \leq \lvert t - T_0 \rvert \leq 0.75 \times T$	$0.5 + 0.5 \cos\left(4\pi \left(\frac{\lvert t-T_0 \rvert}{T} - 0.5\right)\right)$	$0.5 - 0.5 \cos\left(4\pi \left(\frac{\lvert t-T_0 \rvert}{T} - 0.5\right)\right)$
$\lvert t - T_0 \rvert < 0.5 \times T$	1	0

The non-filtered, original wave was used when extracting the wave height, wave period and time of peak. However, in the initial trials of embedding the stream function wave, it was found that using the actual time of peak T_0 from the original wave measurements caused poor embedding. Therefore, each embedding was evaluated and when needed, a small Δt was added to the time of peak T_0.

The stream function wave requires wave period and wave height as input, however, in the literature there are different ways of defining the necessary parameters from the measured wave. Suja-Thauvin reports that the wave period is taken as the trough to trough period of the extreme wave, and that the wave height is the measured wave height [5]. The wave height can be taken as the amplitude of the peak plus the upstream trough, as H_u shown in Figure 4.10, or as the peak plus the downstream trough, H_d. Another alternative is to use the average of H_u and H_d as the wave height. Lastly, the wave height can be taken as the maximum of H_u and H_d.

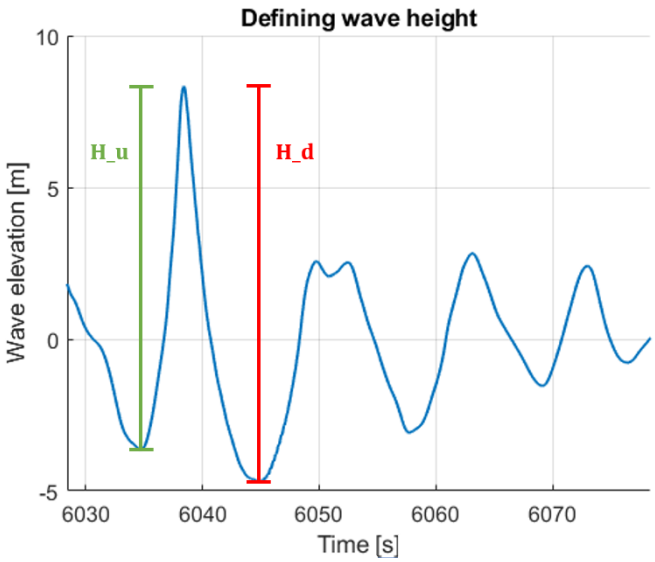

Figure 4.10: Wave height upstream (H_u) and downstream (H_d)

Burmester et al. obtain the wave height as the largest and smallest value of the wave elevation [12]. They estimate the wave length by assuming a breaking wave and apply

$$H_b = 0.142\lambda \tanh \frac{2\pi h}{\lambda} \tag{4.3}$$

where H_b is the breaking wave height (the height of the measured wave) and λ is the wave length [17].

A small study on which approach of wave height H fits the experimental data best is presented in the results.

After the kinematics are obtained, the nodal loads are calculated by the Morison equation, using $C_M = 2$ and $C_D = 1$. The script can be found in Appendix F.

4.3.3 Validation of stream function implementation

In order to validate the implementation of the stream function based on Fenton's work in 1999 [28], it is compared to data published by Rienecker and Fenton in 1981 [23]. This is to ensure that the implementation is done correctly. Rienecker and Fenton present values of kc^2/g obtained by using their method, which can be used to compare with values of kc^2/g obtained by the present method. k is the wave number and c is the wave celerity, both obtained by the stream function calculations, while g is the gravitational acceleration. As done by Suja-Thauvin, the data is calculated for a water depth of $h = 27$ m and a stream function of order $N = 16$ [41]. The obtained kc^2/g values can be seen in Table 4.3, as well as the comparison with the values from Rienecker and Fenton. The discrepancies between the values are found to be small.

Table 4.3: Comparison of kc^2/g [-] obtained by Rienecker and Fenton (1980) [23] and present implementation of Fenton (1999) formulation

Height [m]	**Period [s]**	**Rienecker & Fenton (1981)**	**Present implementation**	**diff [%]**
4.67	15.93	0.615059	0.615094	0.0057
6.82	15.69	0.631112	0.631188	0.0120
10.26	15.19	0.666501	0.669027	0.3790
13.35	14.69	0.706443	0.706493	0.0071
16.26	14.21	0.748231	0.748522	0.0388
17.58	14.05	0.764455	0.764574	0.0156
18.14	14.18	0.767725	0.761326	-0.8335

In addition, the stream function implementation is further validated against data collected by Suja-Thauvin [41]. He compared data published by Peeringa in 2005 [42] with data produced by codes implemented by both Dalrymple in 1996 [43] and Fenton [40]. The code by Fenton will be the same implementation as the one used in this work. The comparison case is a stream function wave of wave height $H = 10$ m, wave period $T = 10$ s and water depth $h = 20$ m. The stream function is of order $N = 12$. The comparison of the wave elevation, particle velocity and particle acceleration can be seen in Figure 4.11. The red dashed line shows the results obtained, while the lines in the legend are the data compared by Suja-Thauvin, including his results as the "present implementation". The comparison shows excellent match in both wave elevation, particle velocity and particle acceleration, indicating that the implementation has been successful.

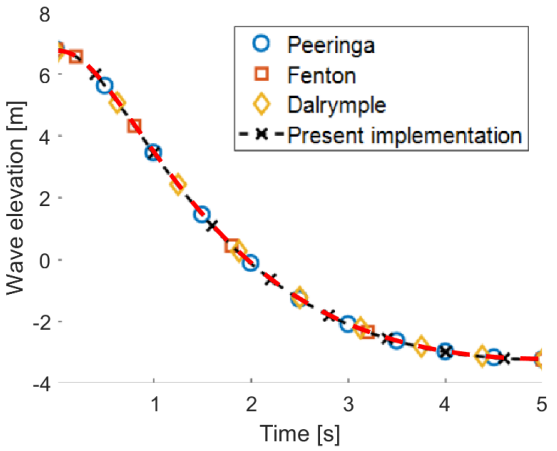

(a) Wave elevation

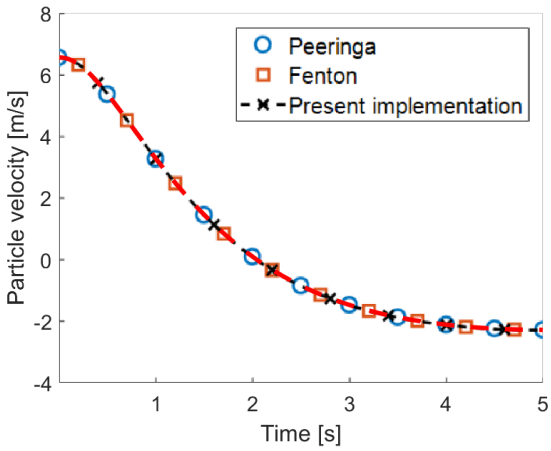

(b) Particle velocity

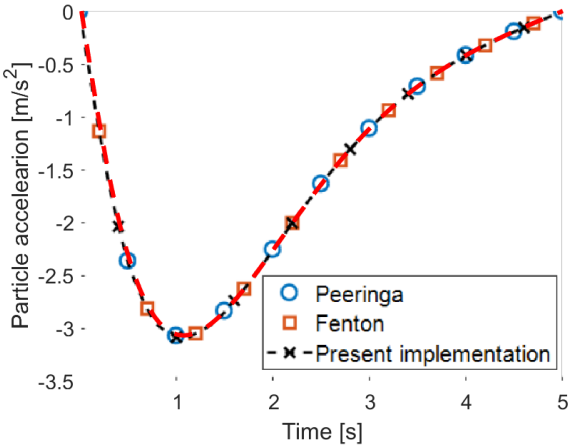

(c) Particle acceleration

Figure 4.11: Verification of the stream function implementation at the free surface compared to results by Suja-Thauvin [41]. Red line is implemented results. Note that in the legend, the present implementation here represents results obtained by Suja-Thauvin.

4.3.4 Implementation of Wienke slamming model

Several parameters must be decided in order to implement the Wienke slamming model. As mentioned in Section 3.6.3, the time of impact $t = 0$ s is defined by Wienke as when the impact wave hits the upstream side of the monopile, in other words, when the maximum surface elevation reaches the upstream side of the monopile [8]. Since the experimental wave is recorded at the center of the monopile, the time frame of the measurement is shifted by $t = R/c$, where R is the radius of the monopile and c is the wave celerity, to account for the discrepancy in the recording as suggested by Burmester et al. [12]. The wave celerity c is found from the embedded stream function wave for each event.

The curling factor λ_c was reported by Wienke as $\lambda_c = 0.5$ for a plunging breaker, however, Burmester et al. found in 2017 that the average curling factor in their test of irregular sea states on a flat seabed was $\lambda_c = 0.2813$ [12]. The curling factor is important in determining the area of impact of the slamming load, and since the sea state in question similar to the sea state investigated by Burmester et al., the curling factor of $\lambda_c = 0.2813$ is applied.

It was found that using the $dt = 0.0707$ s of the linearized data resulted in a rough and imprecise Wienke slamming load. The load time series of which the Wienke slamming model was to be applied to was therefore interpolated such that the new time interval was $dt = 0.01$ s. The dt was chosen to be as large as possible to be computationally efficient, while still capturing the impulse load. This was checked by calculating the area under the impulse load as seen in Figure 4.13a, ensuring that the area was somewhat stable. Burmester et al. used $dt = 0.0276$ s in their formulations, implying that $dt = 0.01$ s is sufficient.

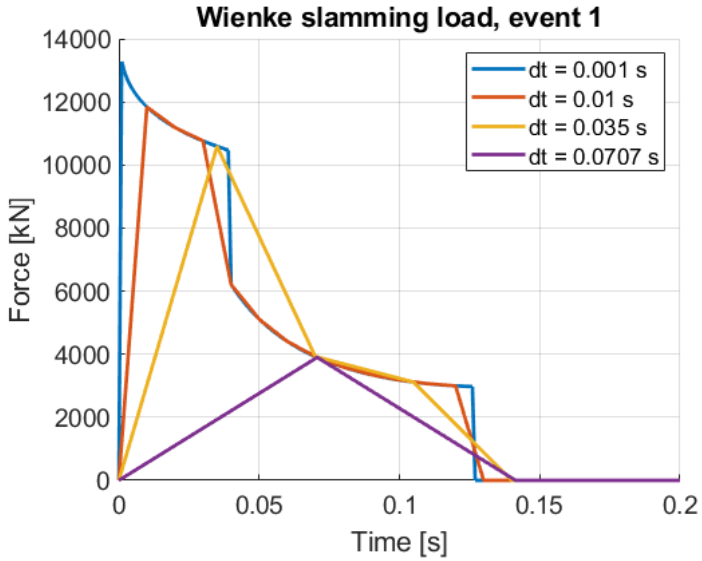

Figure 4.12: Comparison of different time steps in generation of the Wienke impulse load

The slamming load was then added to the load calculated by the Morison equation using the embedded wave kinematics. The slamming load was added to a node located at $z = 4.91$ m above the SWL, meaning that the point of impact was near the actual surface while ensuring it was submerged during the time of impact. The total load after implementing the Wienke slamming model can be seen in Figure 4.13b, where the time of maximum surface elevation and the shifted

time of impact also is indicated.

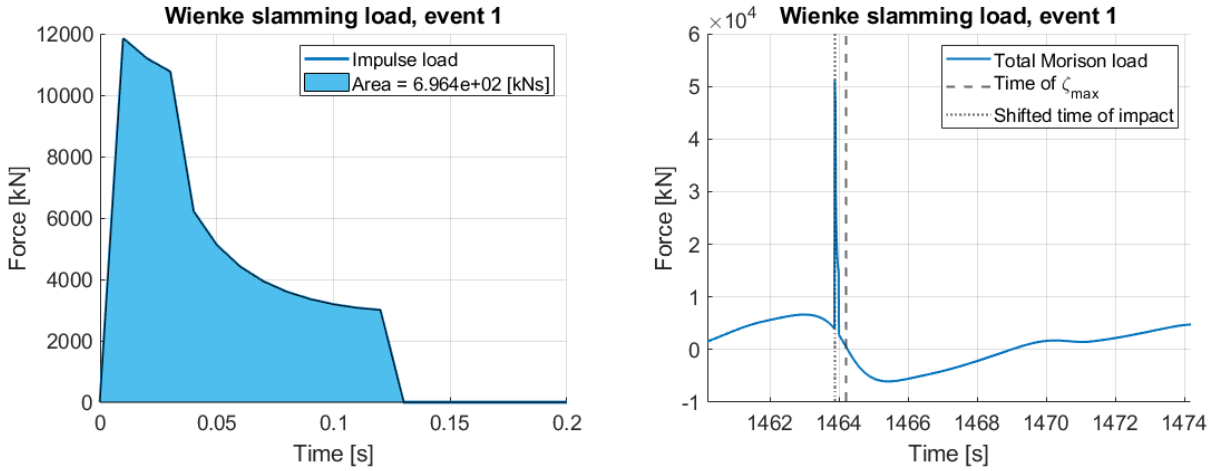

(a) Impulse load

(b) Total input load

Figure 4.13: Implementation of the Wienke slamming load

5 Results and discussion

In this section numerically obtained results are presented. The results are divided into three main parts and are compared to the experimental results and discussed. The three main parts are; eigenfrequencies and damping, regular waves and irregular waves.

5.1 Eigenfrequencies and damping

The damping ratio is estimated from the experimental decay test using Equation 3.58 for an increasing number of peaks to achieve convergence. The resulting convergence of the first damping ratio can be seen in Figure 5.21a and it converges to $\xi = 0.0114$. To identify the second damping ratio, the decay test is filtered to achieve only the second mode decay. The second damping ratio converges to $\xi = 0.0040$ which can be seen in Figure 5.21b.

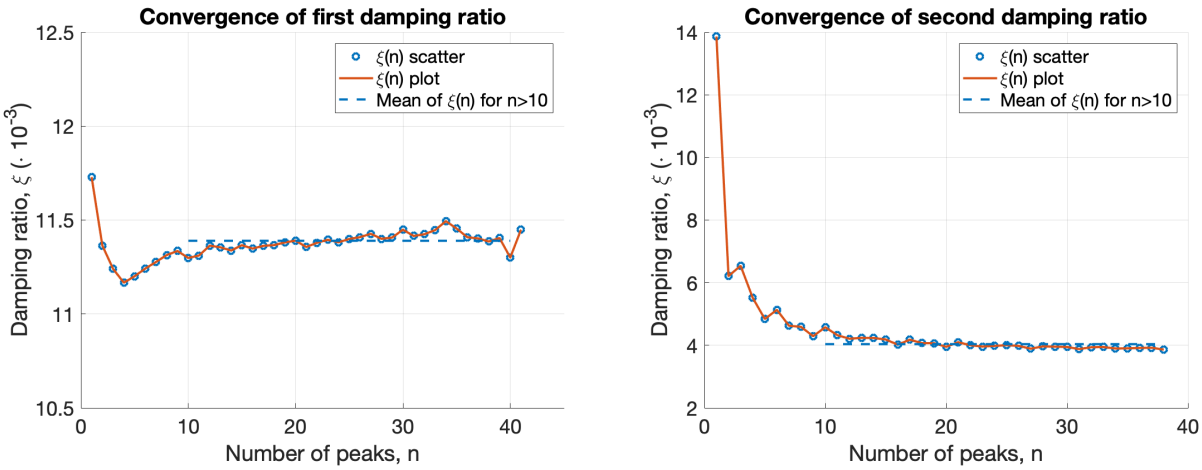

(a) 1^{st} damping ratio

(b) 2^{nd} damping ratio

Figure 5.1: Damping ratios calculated from experimental decay tests

The 1st and 2nd eigenfrequencies and damping ratio found from the decay test of the experimental model is summarized in Table 5.1.

Table 5.1: Eigenfrequencies and damping ratios calculated from the experimental decay test

	Eigenfrequency	**Damping ratio**
1^{st}	0.251 Hz	0.0114
2^{nd}	1.549 Hz	0.0040

The first damping ratio is somewhat larger than the damping ratio obtained by Suja-Thauvin in 2017, but comparing to the range presented by Devriendt et al., it is within the expected area for full-scale damping. The second damping ratio is lower than the one reported by Suja-Thauvin, and also falls a little below the range reported by Devriendt et al. The FFT of the experimental decay test of the model returned 0.25 Hz and 1.549 Hz as the first and second eigenfrequency, respectively.

By comparing to results obtained for a 4 MW monopile supported offshore wind turbine by Suja-Thauvin in 2017, one can see that the first eigenfrequency for the 10 MW turbine is lower than for the 4 MW one. This is due to the increase in top mass and height of turbine tower, which again is due to the lower rotational speed of the larger turbine resulting in lower 1-p and 3-p frequencies. The second eigenfrequency of the 10 MW turbine is higher than for the 4 MW turbine. The reason why the second damping ratio and second eigenfrequency are somewhat deviant is possibly that the 2nd mode is not being modelled exactly right.

In order to get an estimate of the contributions of linear and quadratic damping contributions, the damping coefficients are obtained by using Equation 3.59 and applying the least-square method to fit a straight line to the data. For both the 1st and 2nd eigenfrequency seen in Figure 5.2, the linear damping term is dominating. For the 1st eigenfrequency, in Figure 5.22a, the linear damping term is found to be approximately 0.07 while the quadratic damping term is close to zero. For the 2nd eigenfrequency seen in Figure 5.22b, the linear damping term is found to be approximately 0.15 and the quadratic damping term is small.

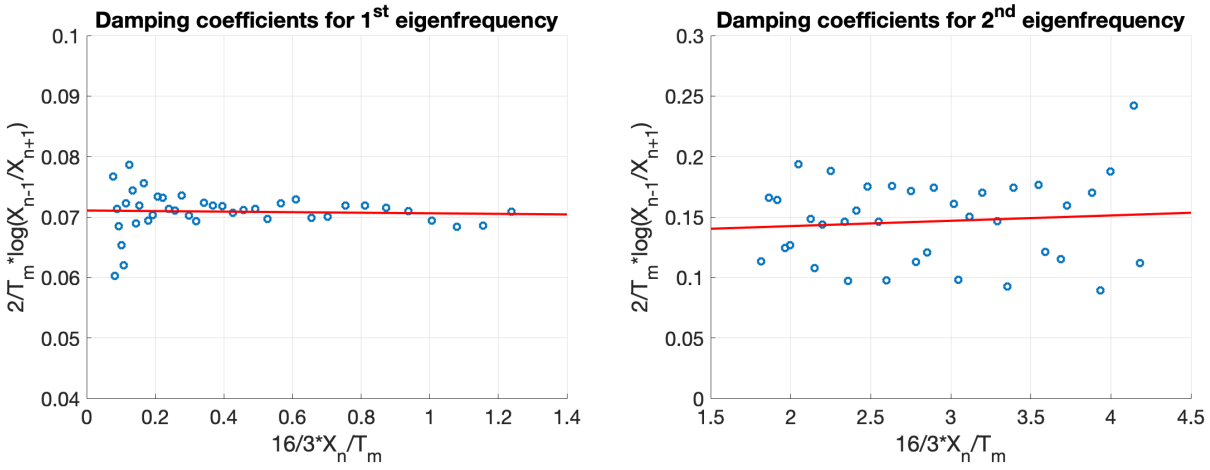

(a) 1^{st} damping coefficients

(b) 2^{nd} damping coefficients

Figure 5.2: Line fit on amplitudes from decay test to identify damping coefficients

Calculation of damping parameters are done using the eigenfrequencies and damping ratios extracted from the decay tests done on the model in the experiment. The mass damping coefficient is found to be $\alpha_1 = 0.0348$ while the stiffness damping coefficient is $\alpha_2 = 0.000414$. The resulting Rayleigh damping can be seen in Figure 5.3.

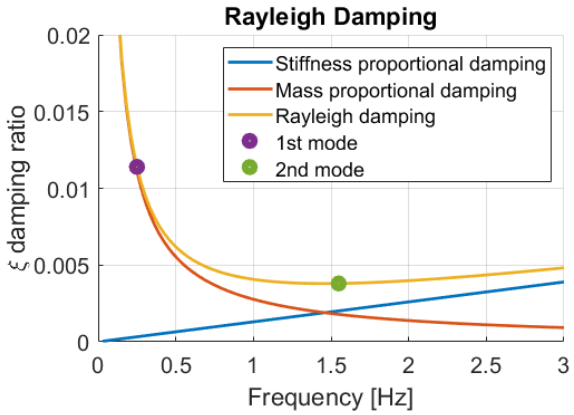

Figure 5.3: Rayleigh Damping

After identifying the mass and stiffness damping coefficients, they can be used as input to the simulation model of the monopile structure. Decay tests are performed in SIMA with the damping ratios provided from the section above. A short impulse load is applied near the water line of the model to induce the two first bending modes. Time series of the simulated and experiment decay are shown in Figure 5.4. The experimental and numerical first two eigenfrequencies are compared in Table 5.2. The numerically obtained 1st and 2nd eigenfrequencies are 0.255 Hz and 1.558 Hz, which are slightly larger than the experimental ones, but only by 1.6% and 0.57% respectively.

Table 5.2: Eigenfrequencies estimated from experiment and numerical decay tests on model

	Experimental	**Numerical**
1st eigenfrequency	0.251 Hz	0.255 Hz
2nd eigenfrequency	1.549 Hz	1.558 Hz

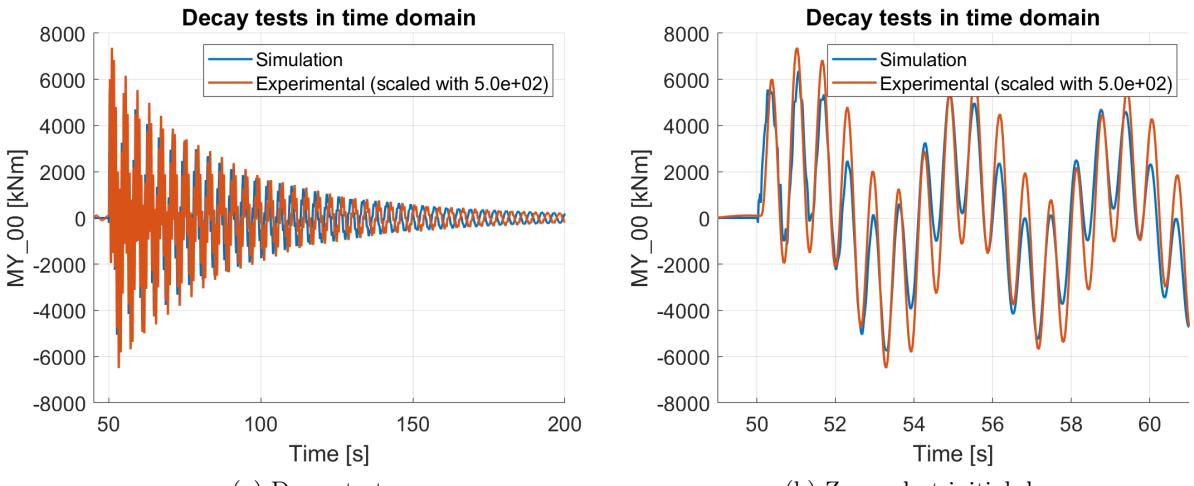

(a) Decay test

(b) Zoomed at initial decay

Figure 5.4: Decay test in time domain compared for simulation and experiment

The decay shape of the monopile structure can be seen for the simulation in Figure 5.5 and for the experiment in Figure 5.6. The decay shape from the simulation is found by the displacement of the nodes in both horizontal and vertical direction. The decay shape contains both the 1st and the 2nd mode shape.

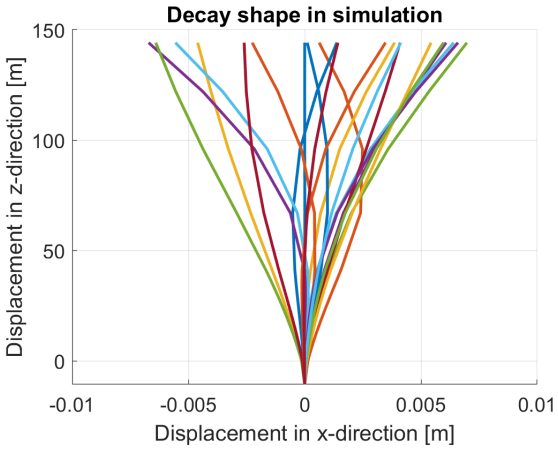

Figure 5.5: Simulated decay shape

The decay shape of the experimental model is found by the accelerometers placed at five different locations on the model. The 1st and 2nd mode shape is separated by band pass filtering around the 1st and 2nd eigenfrequency. If one look only on the outer forms of oscillation in the 2nd mode shape, it looks as expected. However, for some of the oscillations in-between, there seems to be something off with the results from the accelerations at 117 meters. However, much investigation has been done, but the cause of this has not yet been discovered.

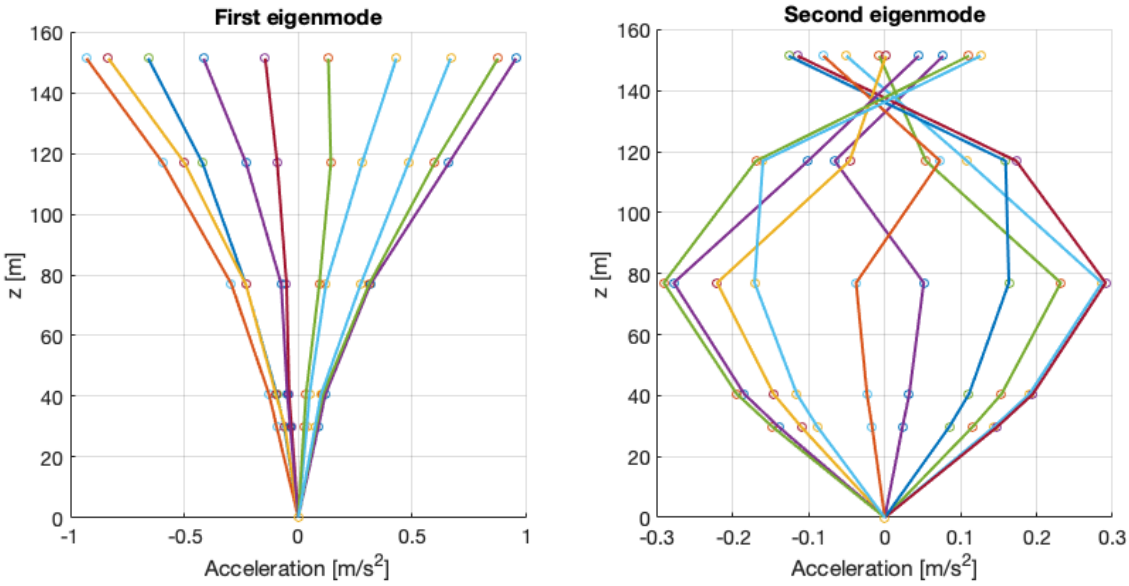

(a) 1st mode shape

(b) 2nd mode shape

Figure 5.6: Mode shapes from accelerometers

5.2 Regular waves

In this section results from experimental and numerical test of regular waves are presented. Two different steepnesses are presented; $s = 1/40$ indicated by $S40$ and $s = 1/22$ indicated by $S22$. In order to make the legend for the plots in this section easier, a list of appreviations used is presented and explained below.

- **EX** - Experiment
  Results from experiment with regular wave tests in wave tank.
- **MW** - Morison with wave input
  Results are obtained using filtered wave elevation from experiment as input to RIFLEX, who applies Morison equation using second order wave with integration of wave forces to wave surface to calculate the wave load.
- **ML** - Morison with linear wave kinematics
  The Morison equation is applied using linear wave kinematics up to the mean water level. A fully linear wave is found using the wave height and wave periods used in the experiments.
- **MSF** - Morison with stream function wave kinematics
  A stream function wave is fitted to the experimental wave, and wave kinematics are obtained and utilized in the Morison equation. This implies that the wave forces are integrated to the actual wave surface.
- **FNV** - FNV method
  The wave forces are obtained using the generalized FNV method, using stream function wave kinematics.
- **SFW** - Stream function wave
- **LW** - Linear wave/Airy wave

5.2.1 Wave elevation

Three different methods of wave elevations are compared to the measured wave elevation in the regular wave tests. The wave elevation of the shortest wave with steepness $s = 1/40$ is investigated in Figure 5.7. The wave is linear and all of the different wave theories returns approximately the same wave elevation as the regular wave measured in the experiment.

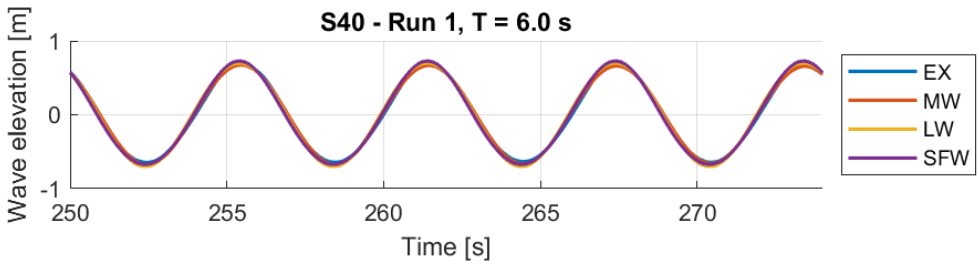

Figure 5.7: Comparison of wave theories and the measured wave elevation for a period of $T = 6$ s and steepness $s = 1/40$

The same comparison is performed for the longest wave of same steepness $s = 1/40$ in Figure 5.8. As seen from the measured wave elevation from the experiment, the wave is no longer linear. The wave crests has gotten higher and the troughs are shallower and wider. The first order linear wave (ML) does not account for any non-linearities, and therefore underestimates the wave crests and overestimate the wave troughs. By adding the second order wave correction to the linear wave (ML) the error from the measured wave decreases. The second order correction adds to the wave crests and removes in the wave troughs, due to its period of oscillation being twice the one of the linear wave. These correction results in a better approximation of the actual measured wave, however, the crests are still lower and the troughs are deeper than the measurements. The stream function wave (SFW) provides the best accuracy with the measured wave elevation. The wave troughs match the measurements, while the wave crests are still slightly lower.

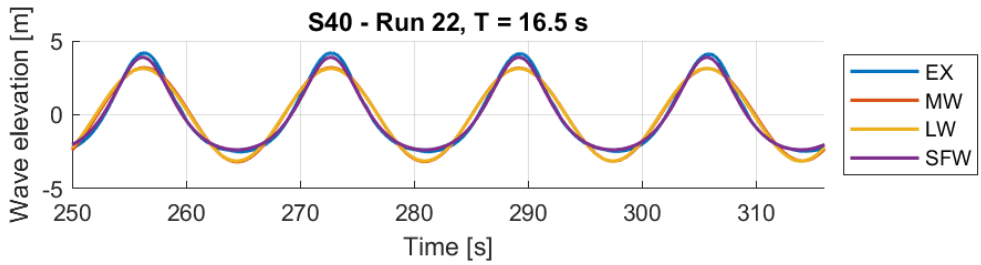

Figure 5.8: Comparison of wave theories and the measured wave elevation for a period of $T = 16.5$ s and steepness $s = 1/40$

In order to investigate the accuracy of the second order linear wave and the stream function wave further, the wave elevation of a wave of higher steepness is analyzed. In Figure 5.9 and Figure 5.10 two wave elevations of steepness $s = 1/22$ is shown. The stream function wave provides a good estimate of the measure wave elevation, especially when taking into considerations the variation of the measured wave elevation. For such a steep and nonlinear wave, it becomes evident that the first and second order linear wave theories are not able to accurately describe the measured wave. In Figure 5.9 one can see the beginning formation of a secondary peak in the wave trough, which becomes even more distinct in Figure 5.10.

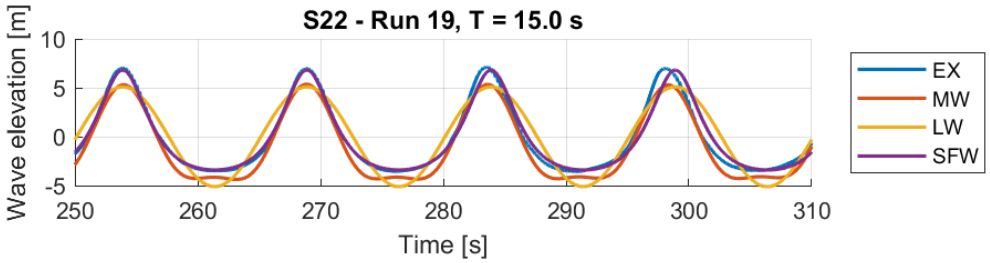

Figure 5.9: Comparison of wave theories and the measured wave elevation for a period of $T = 15$ s and steepness $s = 1/22$

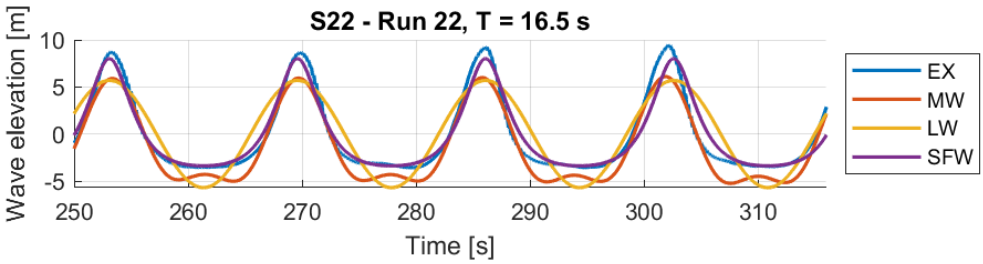

Figure 5.10: Comparison of wave theories and the measured wave elevation for a period of $T = 16.5$ s and steepness $s = 1/22$

This is further confirmed by Figure 3.4, where this regular sea state will be outside of the Stokes second order wave validity range, meaning that the Ursell number will be above the limit of $Ur = 26$. By plotting the wave period T against the Ursell numbers Ur of both $s = 1/40$ and $s = 1/22$ in Figure 5.11, one can see that the occurrence of the secondary peak occurs when the Ursell number is lager than 26. In this figure, it is indicated that this will occur for the waves of steepness $s = 1/22$ when the period is lager than $T > 14.5$ s, which seems to be confirmed in Figure 5.9.

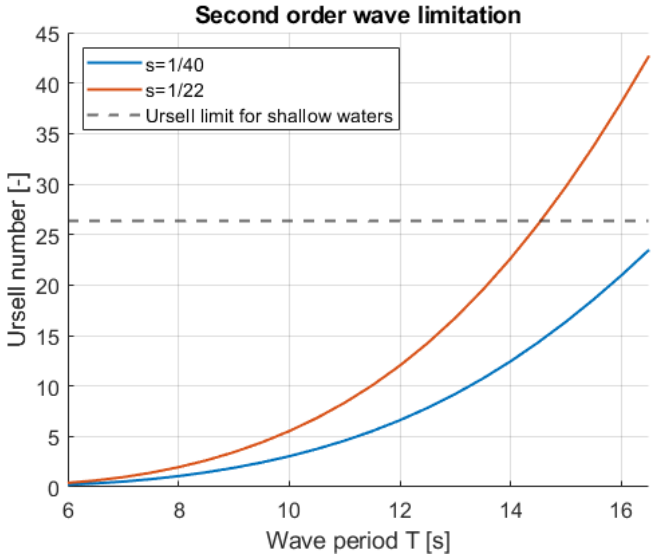

Figure 5.11: Comparison of Ursell numbers

When estimating the wave elevation using linear and stream function kinematics, the wave input is estimated from the input to the wave test. This implies that the period is taken as $T = [6 : 0.5 : 16.5]$ s and the wave height is estimated using the steepness $s = H/\lambda$. In Figure 5.12 and Figure 5.13 the measured mean wave amplitude (blue), the mean wave amplitude of the second order wave elevation found by giving the linearized measured wave elevation in to SIMA (red) and the theoretical wave amplitude, $H/2$, (yellow) are compared. The mean wave amplitude is calculated as the mean peaks value during 20 wave periods. The wave amplitude correspond well for shorter waves, while for longer waves there are some discrepancies.

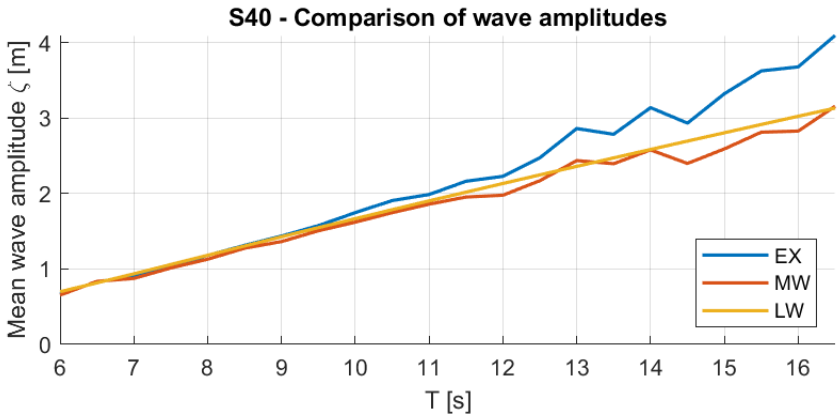

Figure 5.12: Comparison of measured and recreated wave amplitude for steepness $s = 1/40$

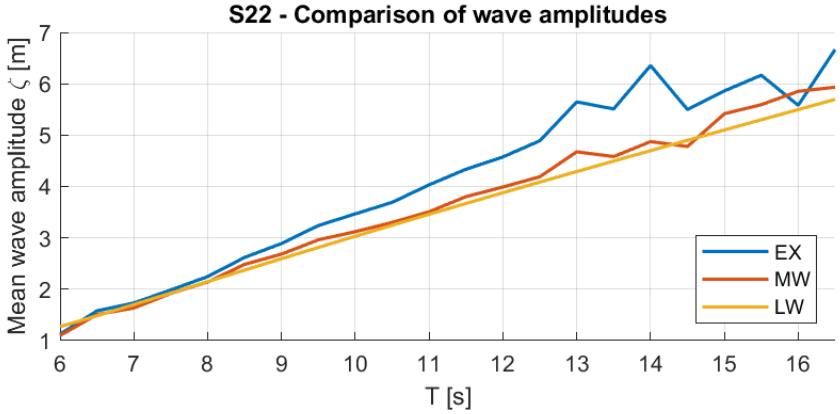

Figure 5.13: Comparison of measured and recreated wave amplitude for steepness $s = 1/22$

In Figure 5.12, the wave amplitude is compared to the theoretical linear wave amplitude for waves of steepness $s = 1/40$. The theoretical wave amplitude is the one used for generation of the linear and the stream function waves. It is found that the experimental wave amplitude is higher for the longer wave periods than the theoretical amplitude. This may be due to the wave generated in the wave tank is not exact to the theoretical wave and may be more non-linear and therefore gain higher wave amplitude. The second order wave amplitude follows the trend of the measured wave only closer to the theoretical line. This is because it is generated by giving the linearized measured wave as input to SIMA. Figure 5.13 shows the wave amplitude for waves of steepness $s = 1/22$. The measured wave amplitude deviates more from the linear wave amplitude than for the waves of lower steepness. This is possibly due to the generated wave in the wave tank is more non-linear due to the higher steepness. The second order wave amplitude no longer follows the exact trend of the measured wave amplitude. This is due to the linearization of the measured wave ends up quite different from the very non-linear wave.

For long, steep waves only the stream function is able to accurately describe the wave elevation. For waves of steepness $s = 1/40$ the second order wave elevation seems to be sufficient, but for the longest waves of steepness $s = 1/22$ the second order correction gets too large such that small peaks occur in the wave troughs.

5.2.2 Structural response

Two different measurements of the response of the model are investigated; the shear force at mudline level and the mudline bending moment. The numerical results obtained using the different methods are compared to the experimental results.

In Figure 5.14, the test with wave steepness $s = 1/40$ and $T = 6.0$ s are shown. All the methods for estimating the wave elevation returns the same as the measured wave elevation in the experiment, which is a linear, regular wave. The shear force at mudline reveals some higher frequency response in the measurements which is not captured in the simulations, however, the amplitude is captured by all methods. There is a slight phase difference present. The mudline bending moment also indicates correct amplitude, however, a slightly larger phase difference between the simulations and the measurements can be seen. The phase shift is discussed later.

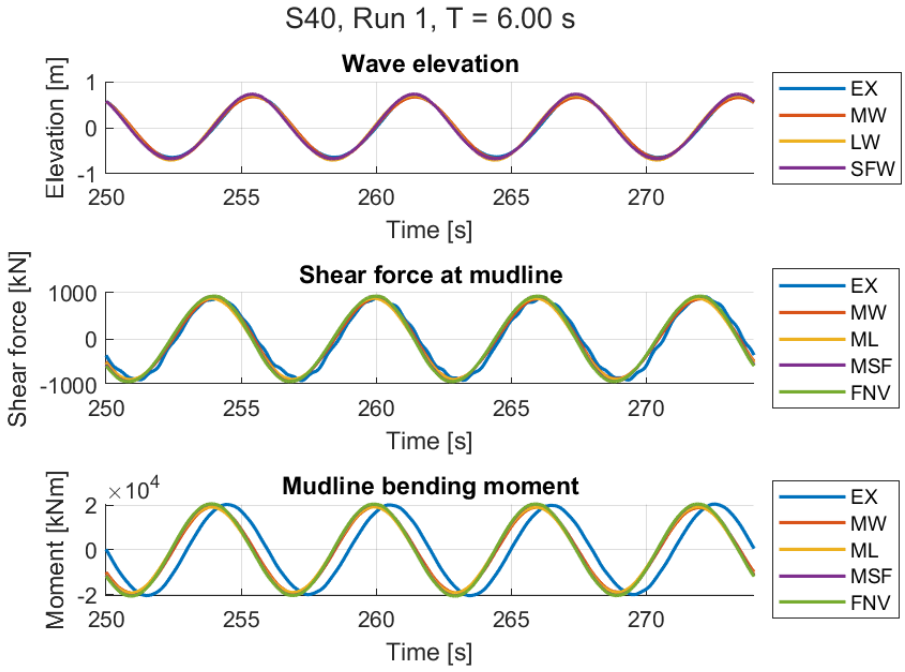

Figure 5.14: Wave elevation and mudline shear force in regular wave tests compared for simulation and experiment with $T = 6$ s and $\zeta_A = 0.7$ m

In Figure 5.15 and Figure 5.16 tests of the same steepness $s = 1/40$ with increasing periods of $T = 12$ s and $T = 16.5$ s are shown. The wave elevation becomes increaslingly non-linear. At $T = 12$ s in Figure 5.15, the linear wave elevation is no longer able to fully capture the measured wave elevation, however, the second order wave elevation and the stream function wave are. The wave period $T = 12$ s is approximatly three times the first eigenfrequency of the model, which is why there is ressonance present in the mudline bending moment. The higher order response present in the shear force measurements is not captured. The Morison with linear kinematics does no longer capture the measured response. In Figure 5.16, the wave elevation is best captured by the stream function wave and the second order wave elevation.

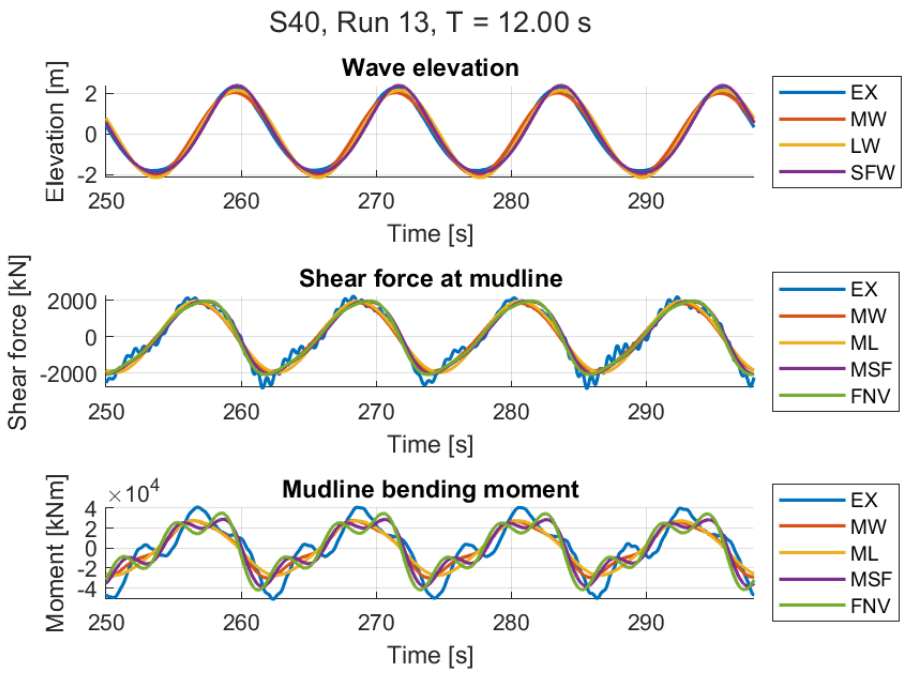

Figure 5.15: Wave elevation and mudline shear force in regular wave tests compared for simulation and experiment with $T = 12$ s and $\zeta_A = 2.13$ m

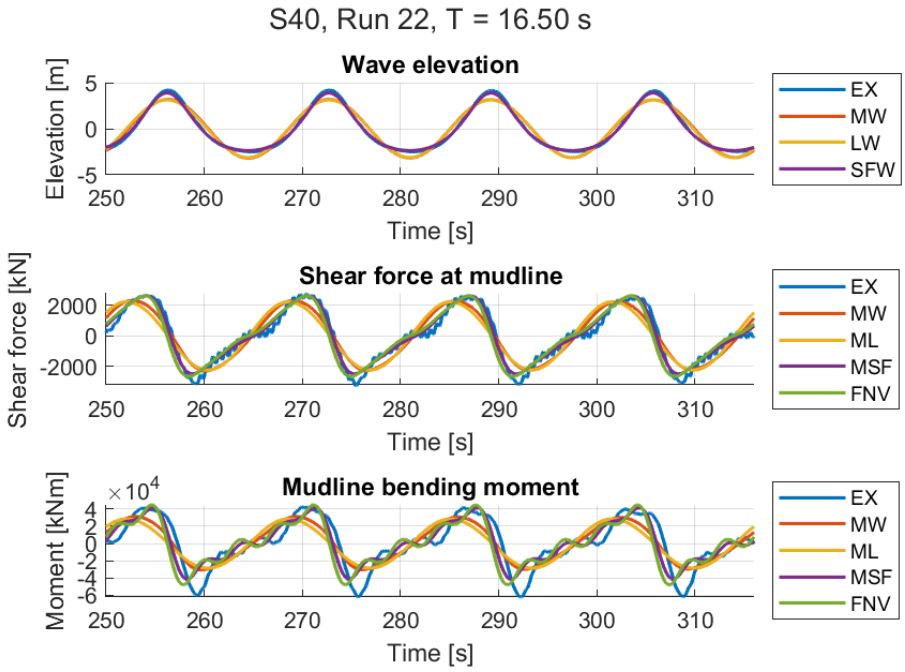

Figure 5.16: Wave elevation and mudline shear force in regular wave tests compared for simulation and experiment with $T = 16.5$ s and $\zeta_A = 3.13$ m

Moving onto waves of higher steepness $s = 1/22$ with the same wave period of $T = 16.5$ s it becomes evident that the wave elevation is only captured by the stream function wave. In the troughs, the second order correction of the second order wave elevation becomes too large, causing a small peak in the troughs.

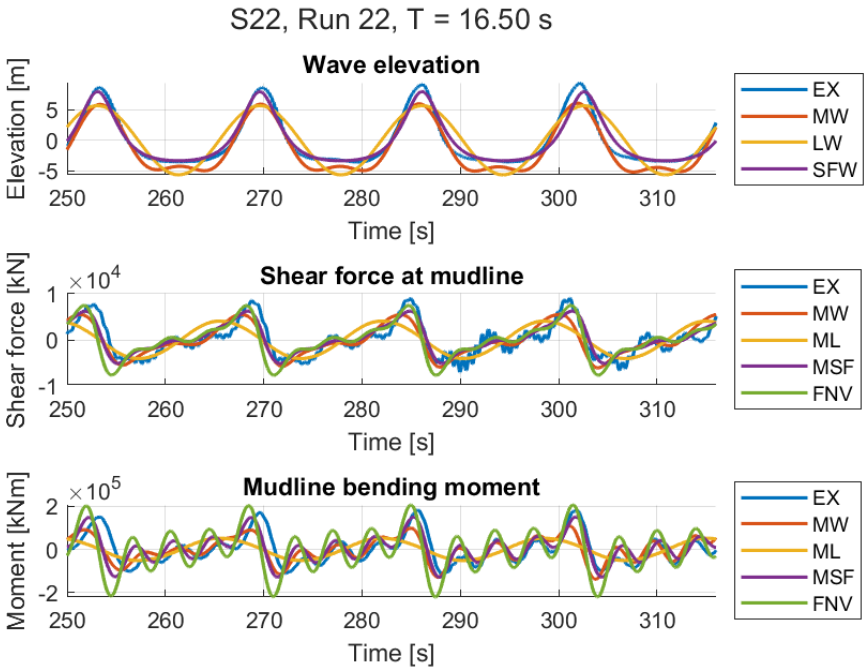

Figure 5.17: Wave elevation and mudline shear force in regular wave tests compared for simulation and experiment with $T = 16.5$ s and $\zeta_A = 5.7$ m

For the shortest, most linear waves, all the methods are able to predict the response. However, a phase shift is present between the measurements and the numerical methods. This shift is especially evident in the mudline bending moment, but a slight phase difference can also be seen in the shear force. Generally, such phase differences can be due to diffraction effects, which are neglected in the Morison calculations. Referring to the figure illustrating the importance of diffraction forces Figure 3.10, one can see that none of the regular waves used are of periods $T < 5.5$ s. However, the second order wave will oscillate with half the period of the first order wave. This means that for the second order wave, diffraction may be of great importance. The expected phase difference due to diffraction effects can be found using the MacChamy-Fuchs diffraction theory, where the phase angle is given as a function of D/λ, where D is the diameter and λ is the wave length [44]. For the shortest waves, this value is $D/\lambda = 0.16$, which corresponds to a phase angle of 11°. The phase difference in the bending moment in Figure 5.14 corresponds to a phase shift of 55°, while the phase shift in the shear force is approximately 20°. This implies that the MacChamy-Fuch diffraction theory does not explain the phase shift alone. Much investigation has been done, but the total reason of the phase shift, and why it is not the same in the moment and shear force response, is not known.

In order to investigate the frequencies present, an FFT is performed of the steady state mudline shear force seen in Figure 5.17. In 5.18a, the 1ω, 2ω etc frequencies can be seen. These are further

investigated later. One can also observe some energy in the measurements from the experiment around the 2nd eigenfrequency, which is not captured by the calculated responses.

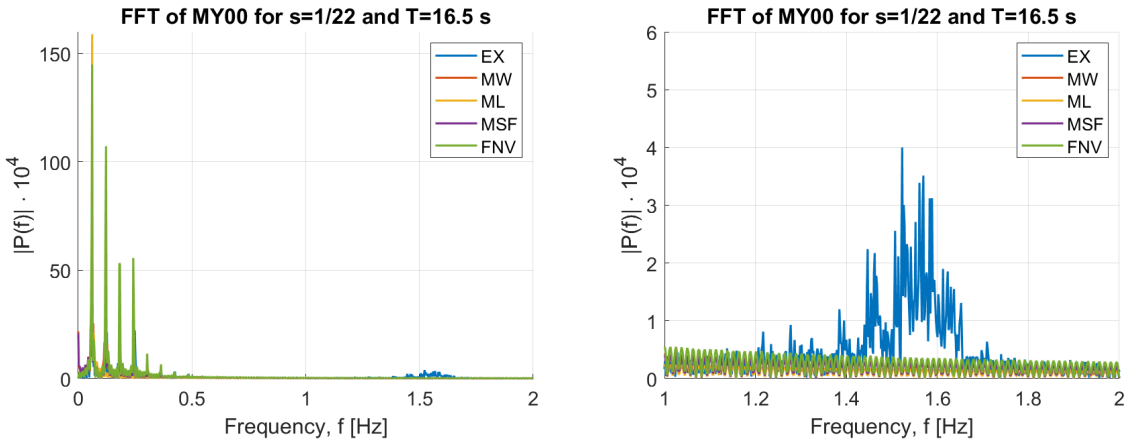

(a) Total frequency area

(b) Zoomed at 2nd eigenfrequency

Figure 5.18: Fast Fourier transformation of the steady state mudline shear force for $s = 1/22$ and $T = 16.5$ s

None of the numerical methods are able to capture the response of the 2nd mode, which is present in the shear force from the experiment. The 2nd mode is not excited in the numerical model. Generally, the 2nd mode can be excited by impulse loads (such as slamming). The exact reason why the 2nd mode is excited in the experiment is unknown, and it is therefore not expected that it will be represented in the numerical methods.

In Figure 5.19 and Figure 5.20, the mudline bending moment from the regular wave test of steepness 1/40 and 1/22 is shown. The bending moment is split into contributions from the different harmonics $1\omega = M_{y1}$, $2\omega = M_{y2}$, $3\omega = M_{y3}$ and $4\omega = M_{y4}$. The bending moment amplitude is taken as the average of 20 peaks in steady state and is normalized using the wave amplitude. The results using stream function kinematics and linear kinematics are normalized using the theoretical wave amplitude, while the experimental results and the results obtained using the actual wave elevation as input are normalized using the measured wave elevation. The peaks present are due to $2f_0$, $3f_0$ and $4f_0$ effects of the first eigenperiod of the structure of 4 s.

For increasingly longer and steeper waves, it becomes evident that the Morison using linear kinematics no longer predicts the measured response, which is expected as the waves become less linear. The mudline bending moment RAOs reveals that the linear Morison (ML) estimates the correct first harmonic response, but no 2nd or 4th harmonic response. There is however some 3rd harmonic response. This is due to the drag term of the Morison equation which results in some response oscillating with a third of the wave period due to the velocity being multiplied with itself. For uneven numbers, they will add while for even numbers they will cancel. However, as the load in this case is mass dominated, the response is small and not representative of the measurements.

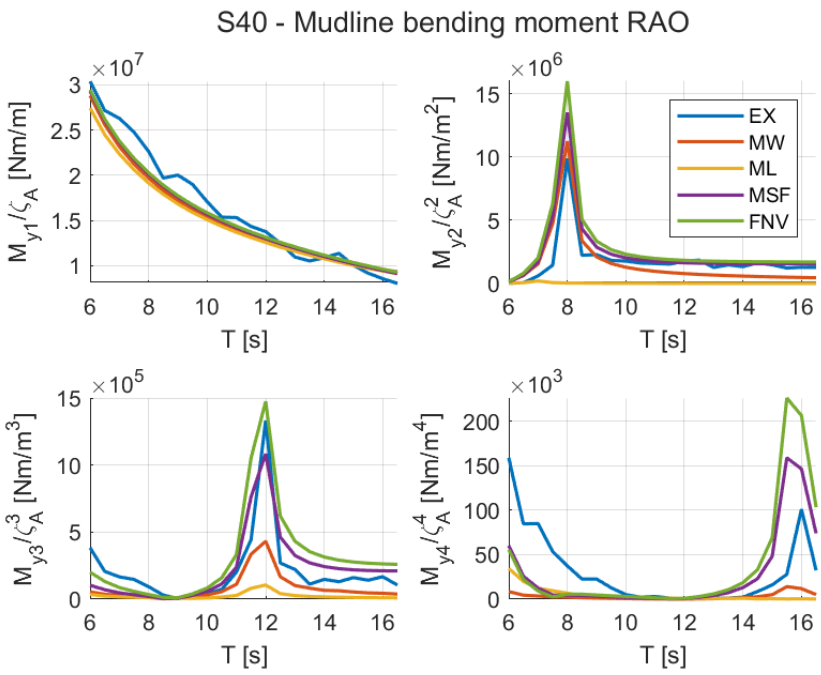

Figure 5.19: Mudline bending moment normalized using the wave amplitude for steepness 1/40

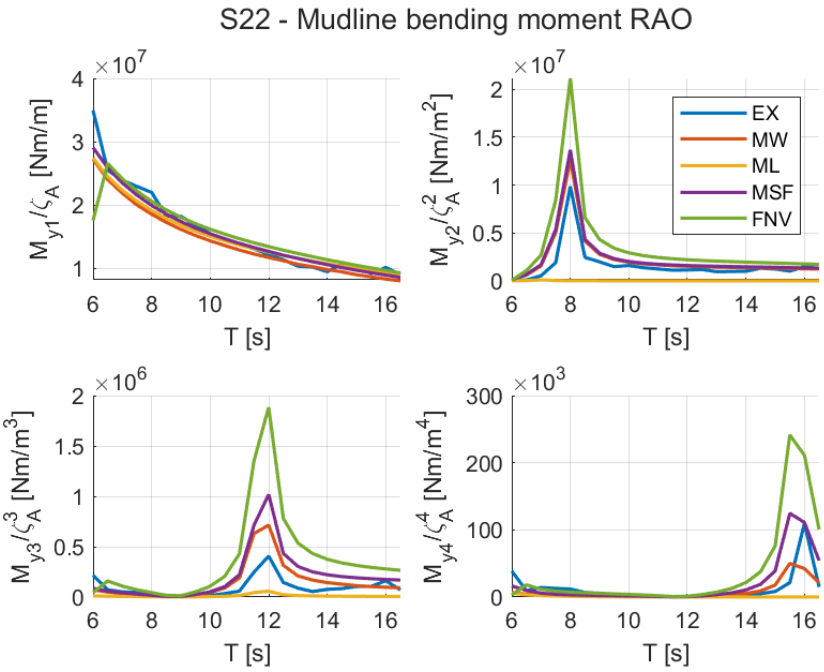

Figure 5.20: Mudline bending moment normalized using the wave amplitude for steepness 1/22

For the waves of steepness $s = 1/40$, the 1st harmonic mudline bending moment generally is underestimated by the numerical methods. Due to the moments being normalized by the wave amplitude, the estimated 1st hamonic moment is the same for the waves of steepness $s = 1/22$. For the steeper waves, the 1st harmonic moment from the numerical methods corresponds well with the measurements. It is therefore reason to believe that the discrepancies between the measurements and the numerical methods for the 1st harmonic moment with $s = 1/40$ are due to experimental uncertainty. The 2nd harmonic mudline bending moment is overestimated by all the numerical methods for both steepnesses (except for the linear Morison which do not contribute). The Morison with second order wave (MW) provides the best estimate, but still overestimates the RAO with approximately $20 - 30\%$. For the waves of steepness $s = 1/22$, the FNV severely overpredicts the 2nd harmonic moment, resulting in a 2nd harmonic moment more than double the amplitude of the measurements.

The 3rd harmonic moment amplitude is accurately predicted by the FNV method for steepness $s = 1/40$, while the Morison equation using stream function kinematics (MSF) underpredicts with about 20%. For waves of this steepness, the 4th harmonic moment also is overpredicted. However, whether or not measurements of this order accurately represent the reality is questioned, and moments of this order are therefore only touched upon. The instruments used for measurement in the experiment must endure loads of order $O(10^7)$ to measure the 1st harmonic moments. This means that for the 4th harmonic moments of order $O(10^3)$ the uncertainties will be significant.

As Kristiansen and Faltisen reported, the FNV method severely overpredicts the higher harmonic moments when the steepness is increased from $s = 1/40$ to $s = 1/22$. The limit of FNV presented by them was $s = 1/40$. For waves above this steepness, the FNV is expected to overpredict 3rd and higher harmonic responses, due to local run-up effects causing a local wave propagating opposite to the incoming wave. This seems to be confirmed in Figure 5.20, where the FNV overpredicts all harmonics above 1st. For waves of this steepness, all the numerical methods (except linear Morison) overpredicts the higher harmonic moments. FNV underpredicts the 1st order moment for steepness $s = 1/22$ with period $T = 6$ s. The exact reason for this is not found, however, it is possibly due to cancellation effects from the added load term at MSL.

5.3 Irregular waves

In this section, results from experimental and numerical tests with irregular waves are presented. The experimental results are presented first, and are later used for comparison and evaluation of the numerical results.

5.3.1 Experimental results

The identification and analysis of events from the irregular wave tests were performed in the pre-project. The model response was found for a total of 22 events. The events are time intervals that contain high response and show signs of resonance. For all the events, the wave elevation and the total bending moment at the base are found. The moment is filtered into contributions from the 1st mode, 2nd mode and quasi-static. The quasi-static moment is defined as the residue after subtracting 1st mode and 2nd mode moment contribution from the total moment. These results can be seen for the first event in Figure 5.21, while all the events are shown in Appendix A.

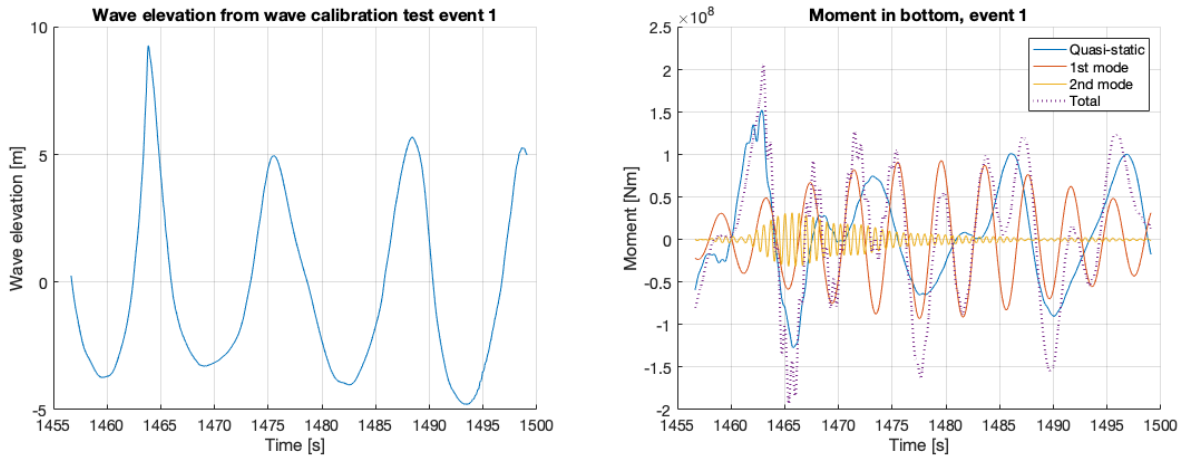

(a) Wave elevation

(b) Response

Figure 5.21: Wave elevation and moment in bottom in event 1

Figure 5.21a shows the full scale wave elevation in event 1, taken from the wave calibration test, meaning that it is the wave elevation at the exact location of the model. In Figure 5.21b, one can see the bending moment in the model base filtered as explained above. The purple, stapled line is the total moment, which is used to identify where the maximum bending moment will occur. For event 1, this is seen to be around 1463 seconds. The blue line is the quasi-static moment, whereas the red line is the 1st mode moment. The oscillations present are the ringing response. Finally, the yellow line represents the 2nd mode moment, which appears when there is excitation of the second mode of the model. The oscillations of the 2nd mode moment die out relatively quickly.

There is also available video from the test in the wave basin. This video can be used to characterize the wave as breaking or not, and to characterize the load as a slamming load or not. The wave is said to be breaking if there is foam present when it passes the model. The load is characterized as a slamming load if there is water spray present. In Figure 5.22, one can see snapshots both in front and back of the model. In Figure 5.22a, one can clearly see spray present, meaning that the load is a slamming load. In Figure 5.22b, one can observe foam on the wave as it passes the model,

and the wave is therefore characterized as breaking. Snapshots from all the events can be found in Appendix B.

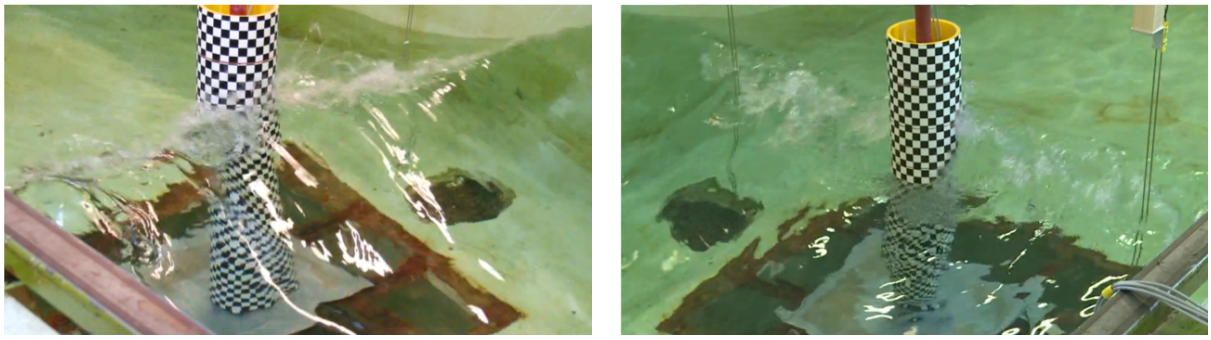

(a) Front of model (b) Back

Figure 5.22: Snapshots from video of event 1

In total 22 events were selected from test 6050 and analyzed. They are characterized in Table C.1. The steepness of the wave is calculated for every event, and the maximum moment and the contributions to this are found. In addition, using the video of the test, slamming and breaking can be determined. The mean steepness, absolute maximum moment and contributions are also calculated and shown in Table C.1 in Appendix C.

The contributions to the maximum bending moment at the base can also be illustrated as a bar diagram, as seen in Figure 5.23.

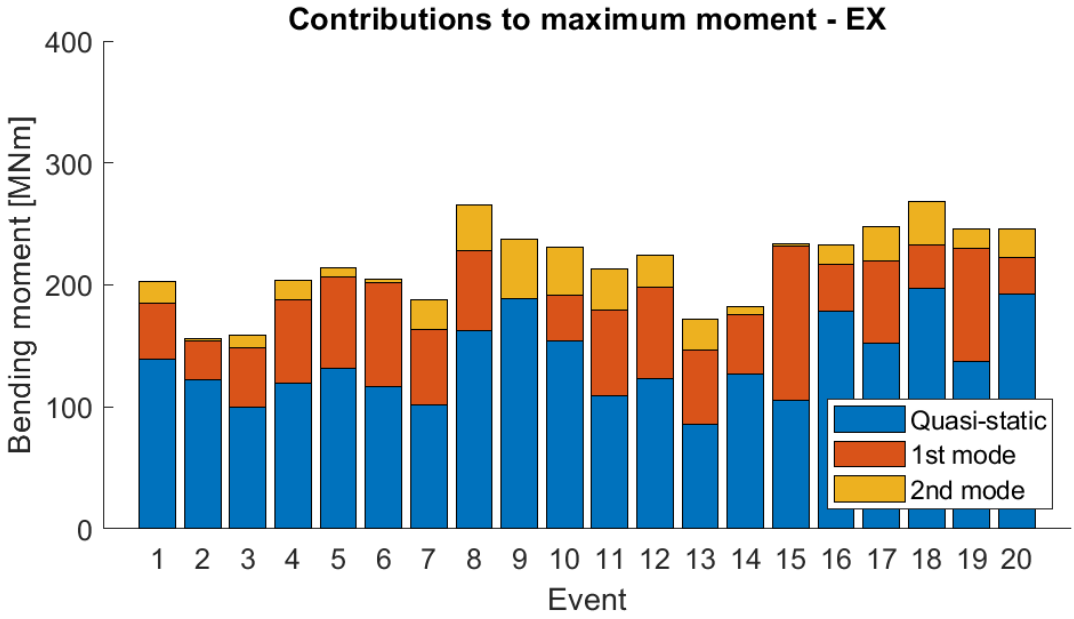

Figure 5.23: Contributions to maximum moment (The last two events are not shown)

There are analyzed in total 22 different events. The waves are in general very steep, the steepness varies from $3.7 - 27.8$ m/s. Most of the waves break as they pass the model in the wave basin, but not all. Generally, the steepest waves break, but this is not the case for all, as for example the wave in event 16, which has a steepness of 17 m/s but no breaking. It should be noted that some of the waves do break after passing the model, but the definition of breaking in this characterization is at the model position in the wave basin. For all events, except event 2, there is observed water spray, indicating that there is slamming.

The maximum bending moment at the model base varies from 156.4 MNm up to 273.8 MNm for the events. For around 65 % of the events, the maximum bending moment is positive. The largest contribution to the maximum moment comes from the quasi-static moment. The quasi-static moment accounts for about $50 - 80\%$ of the total maximum moment. The first mode contributes up to 53%, but generally, the contribution is around $20 - 30\%$. Finally, the second mode contributes from 1% up to 19% of the total maximum moment for the 22 events investigated. For event 9, the contribution from the 1st mode became negative, due to opposite signs of the total moment and the 1st mode moment.

Similar to the studies done by Suja-Tauvin in 2017 [6], it is found that the structure experience both ringing and excitation of the second mode in addition of the quasi-static response. The contributions of 1st, 2nd and quasi-static are similar as to the one derived in this report, even though the diameter and height of the turbine foundation is increased. It is also found that the largest responses occur when the second mode of the structure is triggered by a breaking wave on top of a ringing response, same as the results obtained by Suja-Tauvin.

5.3.2 Numerical results

The numerical results are presented, compared with the experimental results and discussed in this section. The number of events investigated is reduced from 22 to 20, meaning that the last two events presented in the section above are not included. Selected figures are shown and discussed, however, time series of responses in all 20 events can be found in Appendix D. The legends in this section are simplified with the following abbreviations:

- **EX** - Experiment
  Results from experiment with irregular wave tests in wave tank.
- **ML** - Morison with linear kinematics
  The linear kinematics are obtained using filtered wave elevation from the experiment, and is applied up to mean sea level.
- **MSF** - Morison with stream function wave kinematics
  A stream function wave is fitted to the experimental wave, and wave kinematics are obtained and utilized in the Morison equation. This implies that the wave forces are integrated to the actual wave surface.
- **MSFW** - Morison with stream function kinematics and Wienke slamming model
  The Morison load is the same as for MSF, however, now the Wienke slamming model is added.

5.3.2.1 Embedding of stream function waves

A study on how to select proper wave height for input to the generation of the stream function wave is performed on the first six events. The use of Goda's breaking criteria failed as an option of H because it resulted in an unphysical wave (above the breaking limit set by the stream function code), and is therefore excluded in the consideration of which definition of wave height to use. In Figure 5.24, the four different options presented in section 4.3.2 are presented as percentages of the original wave elevation. The elevations are taken from the time instant of maximum wave elevation for the six first events.

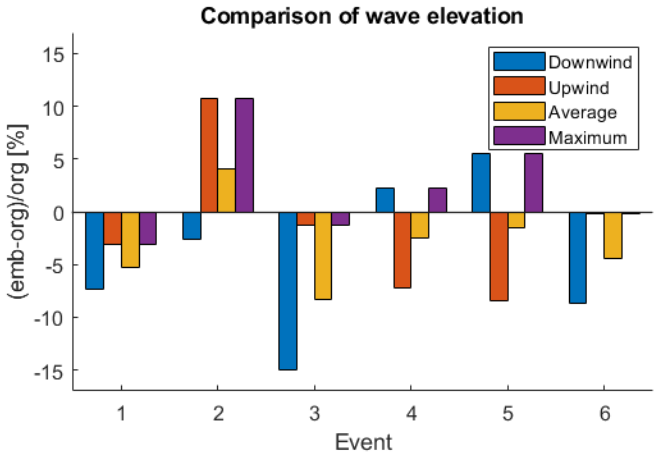

Figure 5.24: Different options of how to give input to stream function wave

In Figure 5.24, it becomes clear that using the wave height measured by the downwind trough causes an underestimation of the wave elevation for 4/6 events. The use of the upwind trough also cases underestimation of the wave elevation for 4/6 events. Using the average between the up- and downwind trough leads to the underestimation becoming smaller. However, in order to be on the conservative side (and thus overestimate the wave elevation rather than underestimating it), the maximum of the up- and downwind trough should be used.

Using the maximum H of the up- and downwind wave trough in the original time series to generate a stream function wave of which to embed to the filtered wave elevation is done in Figure 5.25. An order of $N = 10$ of the stream function wave was found to be sufficient in the present implementations.

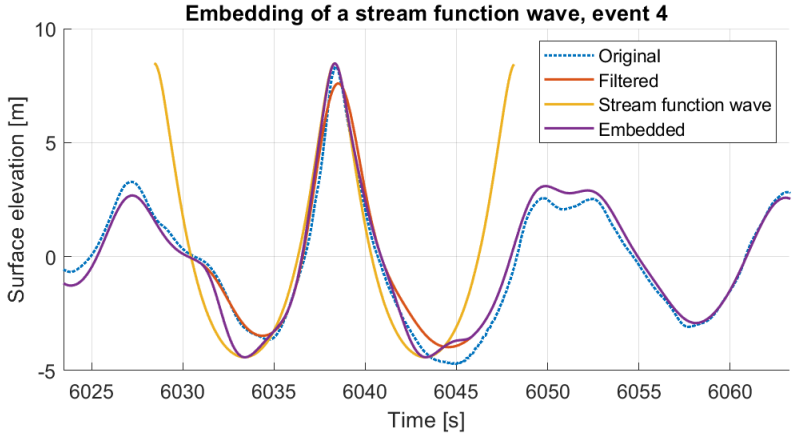

Figure 5.25: Embedding of a stream function wave in event 4

5.3.2.2 Morison using linear kinematics

The first method tested is the Morison equation using linear kinematics. The kinematics is extracted from the linearized and filtered measured wave elevation (the filtered wave in Figure 5.25), and is applied up to the mean sea level. In the Morison equation, a mass coefficient of $C_M = 2$ and drag coefficient of $C_D = 1$ are used. The resulting mudline bending moment obtained by this method can be seen in Figure 5.26. The maximum moment consists of quasi-static moment only, nor 1st or 2nd mode of the structure are excited, and the measured response is therefore not matched. Comparing with the experimental results in Figure 5.23, it is clear that this method overall underpredicts the quasi-static contribution. The results obtained by this method also predicts similar quasi-static contribution to the maximum moment in all events, whereas in the measurements they are more different from each other. This may be due to only applying the hydrodynamic load model up to mean sea level. The waves in the irregular sea state are non-linear, where the peaks are much higher than the troughs, while the assumption to apply the loads only to the mean sea level generally is more applicable for more linear sea. These findings confirm those of Suja-Thaivin in 2018 and Paulsen et al. in 2013, that linear kinematics are not suitable to simulate extreme waves [5][9].

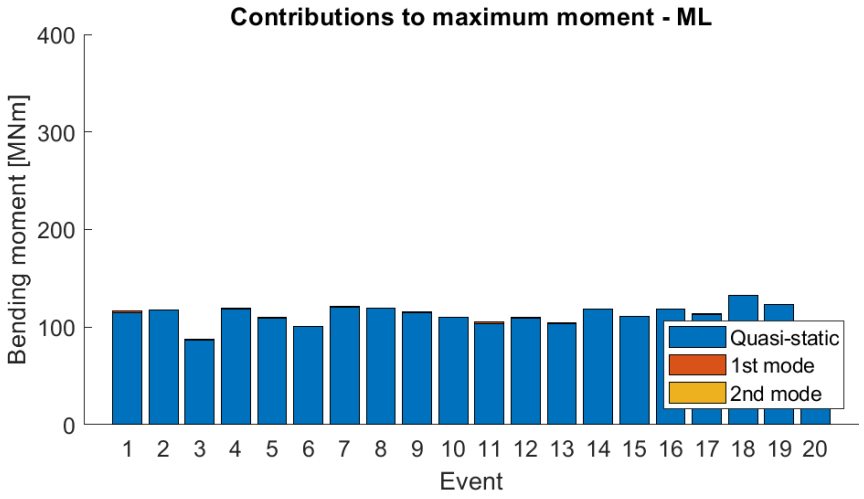

Figure 5.26: Moment contributions of maximum moment using Morison with linear kinematics

5.3.2.3 Morison using stream function kinematics

Moving on, the Morison equation is applied using stream function kinematics obtained in the embedding of a stream function wave, which corresponds to the embedded wave elevation seen in Figure 5.25. The kinematics are now integrated up to the free sea surface. The quasi-static moment contributions are larger than for the results obtained using the linear wave because of the embedded stream function wave and the kinematics being integrated all the way to the free surface. The 1st mode is now excited for all 20 events, indicating that the nonlinear stream function kinematics are able to produce 1st mode response. This corresponds with the findings of Suja-Thauvin in 2018 [5].

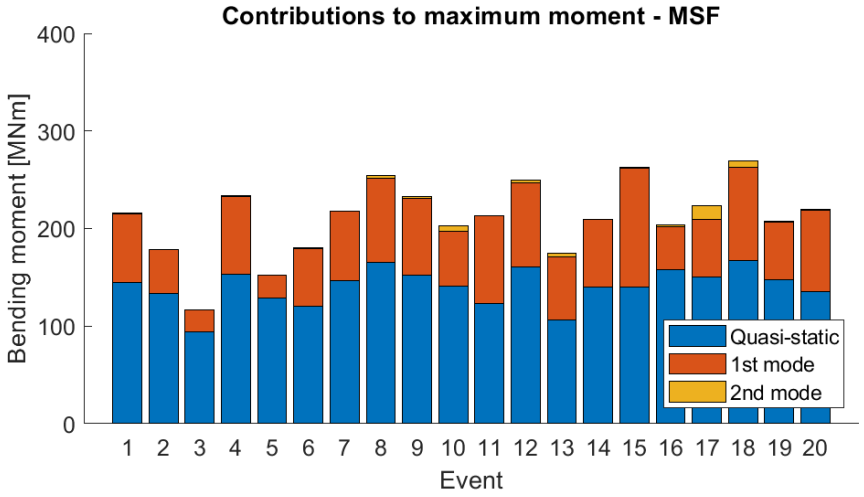

Figure 5.27: Moment contributions of maximum moment using Morison with stream function kinematics

5.3.2.4 Morison using stream function kinematics and Wienke slammning model

Finally, the Wienke slamming model is added to the Morison load calculated by stream function kinematics. The quasi-static and 1st mode contributions are the same as in Figure 5.27, but now there is contribution from the 2nd mode as well. Some of the quasi-static and 1st mode contributions vary slightly, but this is most likely due to the fact that the addition of the slamming model may shift the time of maximum moment. This confirms that the Wienke slamming model has the ability to trigger 2nd mode response. As seen in Figure 5.27, the contribution from the 2nd mode is quite extensive, and often accounts for more of the total moment than the 1st mode contribution.

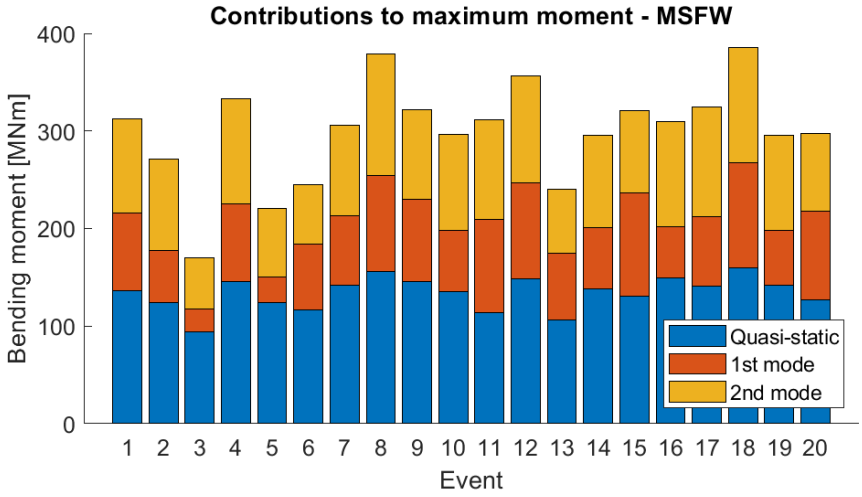

Figure 5.28: Moment contributions of maximum moment using Morison with stream function kinematics and Wienke slamming model

In Figure 5.29 and Figure 5.30, the time series of two different events are shown. In Figure 5.29, it can be observed that the embedded wave elevation (containing the stream function wave) marked "Emb" in the figure does not quite match the measured wave elevation. The wave period and time of peak look like a good match, but the wave elevation peak in the measurements is higher than for the embedded wave elevation. The embedded wave elevation in Figure 5.30 is a much better match for the measured wave. The reason for this may be found in Table C.1, where it is stated that the wave in event 1 is breaking, while the wave in event 4 is not. The wave in event 1 is also much steeper than the wave in event 4, which may affect the embedding.

The decomposed response of the mudline bending moment can also be seen in Figure 5.29 and Figure 5.30. For both events, the passing of the steep waves excites 1st mode response, so-called ringing response. The addition of the slamming load causes the 2nd mode to be excited as well.

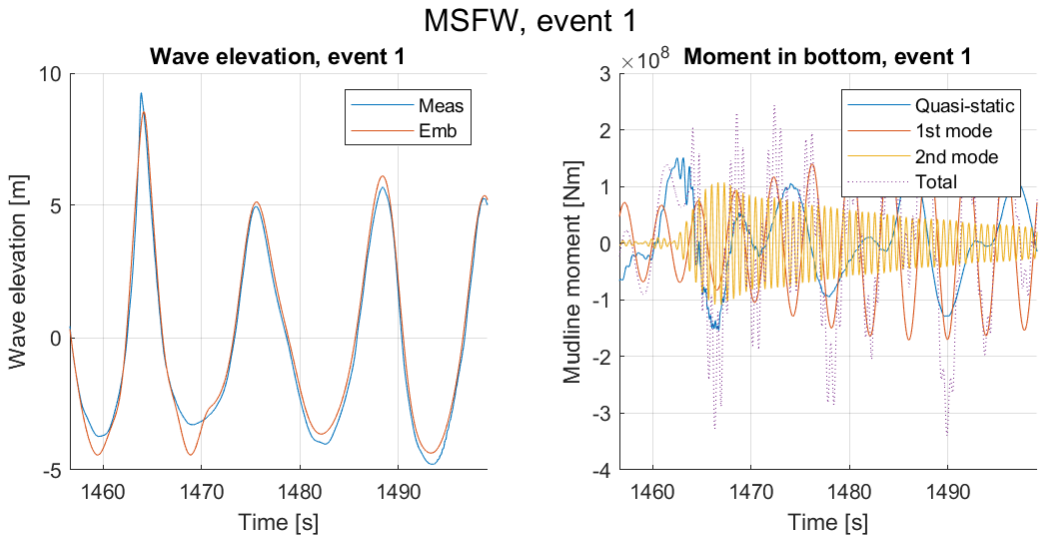

Figure 5.29: Event 1 recreated by Morison equation with stream function kinematics and Wienke slamming model

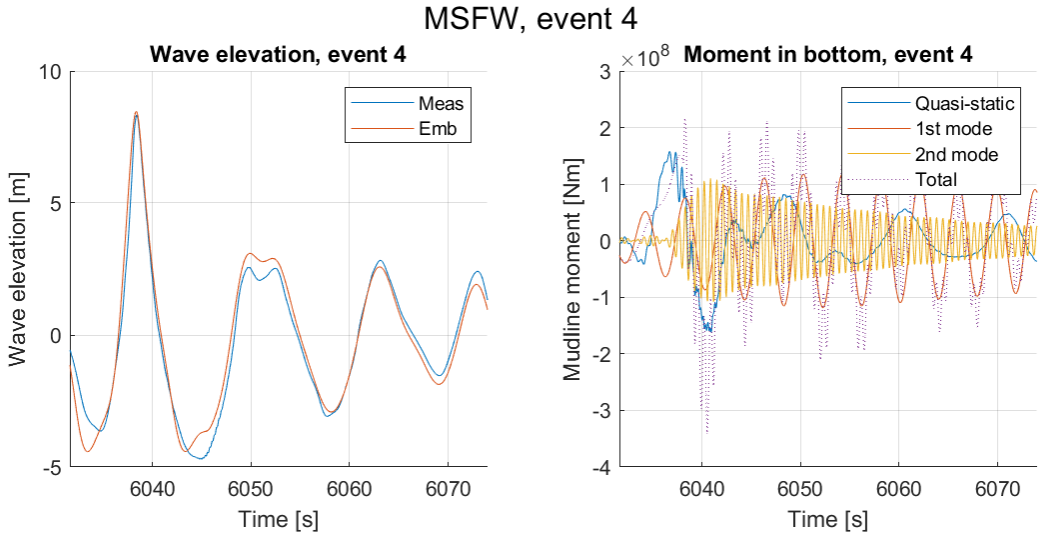

Figure 5.30: Event 4 recreated by Morison equation with stream function kinematics and Wienke slamming model

In order to investigate the addition of the Wienke slamming model, the numerical excitation force is compared to the measured mudline shear force for event 1 and 4 in Figure 5.31. The numerical excitation force is calculated by the Morison equation using stream function kinematics and adding the Wienke slamming load. For both events, the time of impact for the Wienke load is delayed compared to the measurements. This may indicate that using the time of the wave peak as the time of impact may not be the best approach for this setup.

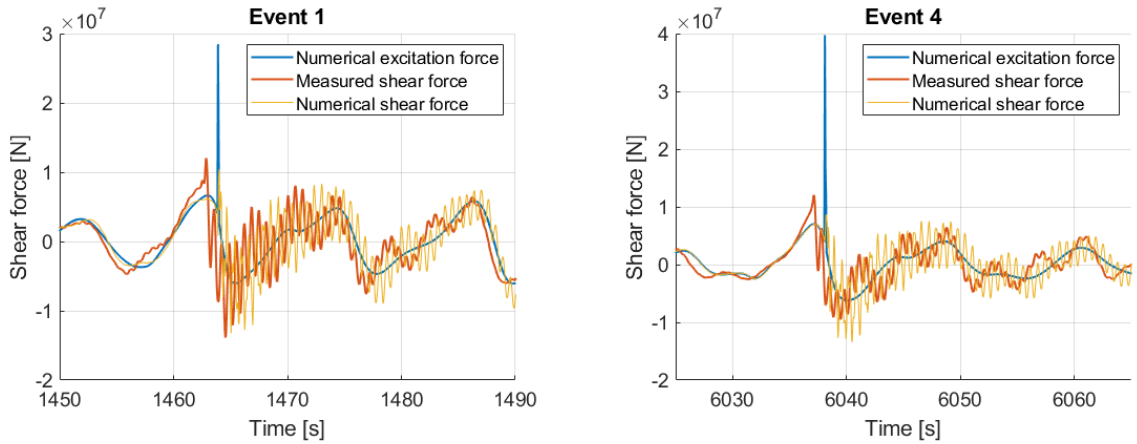

(a) Event 1

(b) Event 4

Figure 5.31: Comparing the measured shear force with the numerical Morison excitation force with Wienke slamming force for two different events

5.3.2.5 Comparison of methods

In Figure 5.32 and Figure 5.33, the three different numerical methods are compared to the measurements.

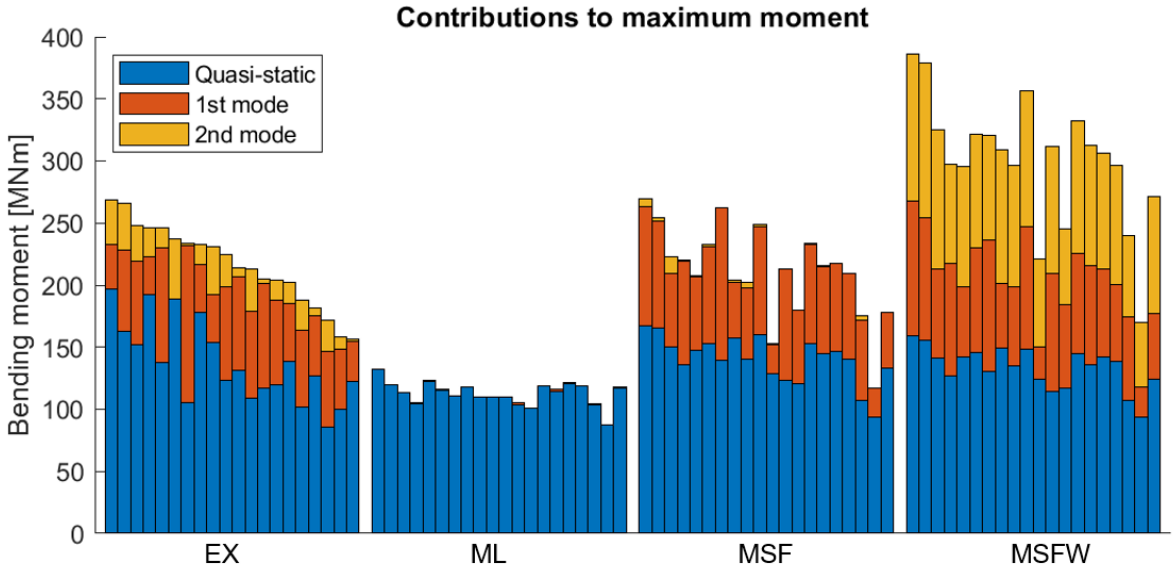

Figure 5.32: Moment contributions of maximum moment in descending order from maximum total moment in the measurements

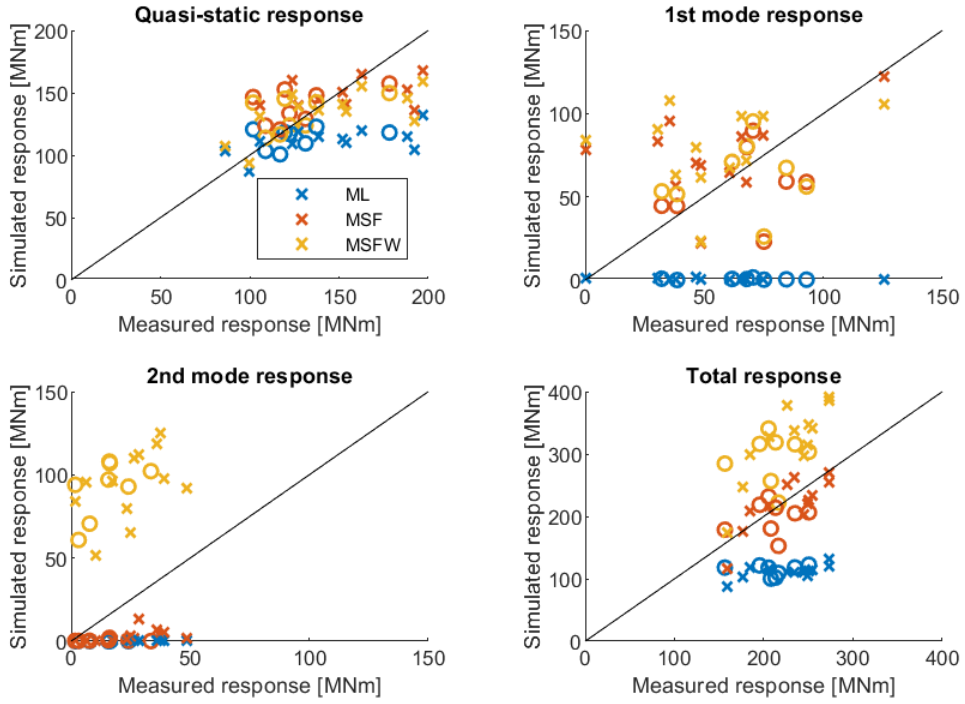

Figure 5.33: Comparison of simulated and measured response. "X" indicate that the measured wave is breaking, while "O" indicates a non-breaking measured wave.

Figure 5.32 shows that all the methods provide a reasonable quasi-static response, however, the linear Morison method underestimates, especially for some of the higher quasi-static responses. This can also be seen in "Quasi-static response" in Figure 5.33, where the linear Morison method (ML) response complies with the measurements for the lower responses, while underestimating the higher ones. In total the quasi-static response is underestimated for 17/20 events. The quasi-static response from the linear Morison method is found to be similar for all events, while there are more spread in the measured quasi-static response. This is possibly due to the linearization and filtration of the measured wave elevation when given as input to the linear Morison model, and due to the loads only being integrated up the to still water level.

The two other methods, Morison with stream function kinematics (MSF) and Morison with stream function kinematics and Wienke slamming (MSFW) provides a better estimate of the quasi-static response, due to the embedded stream function wave and the integration of the wave loads up to the free surface. The simulated quasi-static response is larger than the measured one for 12/20 and 9/20 events for MSF and MSFW, respectively. The discrepancies between the estimated response for the two methods are due to the time of maximum response being shifted when the Wienke slamming model is added. The quasi-static response produced by these two methods seems to provide a conservative estimate for the lower measured responses, and slightly unconservative estimate for the higher ones.

The Morison with linear kinematics does not provide any 1st mode response. The Morison with stream function kinematics generally provides a conservative 1st mode response, especially for the events with a breaking wave, which is indicated by "X" in Figure 5.33. In the 20 events investigated, the 1st mode response is overestimated in 14 of them. This deviates with the results obtained by Suja-Thauvin in 2018 [5], as he observed that the 1st mode response generally was underestimated by the numerical methods.

The 2nd mode is significantly overestimated by the numerical model in all 20 events. In the measured response, none of the 2nd mode responses are above 50 MNm, while in the simulations, none of them er below 50 MNm. The simulated 2nd mode response being significantly larger than the measured one complies with the findings of Suja-Thauvin [5].

The total response in Figure 5.33 summarize the findings in the decomposed response. The linear Morison method underestimates the total response, due to the lack of contribution in 1st and 2nd mode response as well as underestimate the quasi-static response in some of the events. The Morison with stream function kinematics (MSF) ends up providing a reasonably well estimate of the total response, even though it does not have noteworthy contribution in the 2nd mode. For 8/20 events, the MSF method provides slightly conservative estimate of the total response. This is due to the 1st mode response being overestimated. However, even if this method can provide a conservative estimate of the total response, the stress distribution along the monopile may be inaccurate due to the lack of 2nd mode response [5].

The addition of the Wienke slamming model to the Morison with stream function kinematics therefore results in a total response significantly larger than the measured total response. The total response is overestimated for 20/20 events. There does not seem to be any clear correlation between the total simulated response and whether or not the experimental wave is breaking. For the highest responses, the wave is generally breaking, but this is also seen for some of the lower responses, so it does not open up for a clear conclusion. However, as noted previously, the 1st mode response is generally overestimated when the wave is breaking.

6 Conclusions

In this thesis, experimental data on a 9-diameter monopile foundation supporting a 10 MW wind turbine subjected to irregular sea have been studied. The experimental data have been compared to numerical methods. The experimental decay test performed on the model was studied to identify the eigenfrequencies and damping ratios of the 1st and 2nd mode of the model. These parameters were used to tune the numerical model of the model used in the experiments. The 1st and 2nd modes of the experimental model were found to have eigenfrequencies of $f_1 = 0.250$ Hz and $f_2 = 1.549$ Hz, and damping ratios of $\xi_1 = 1.14\%$ and $\xi_2 = 0.40\%$. The numerically obtained 1st and 2nd eigenfrequencies are slightly larger than the experimental ones, by 1.6% and 0.57% respectively, while the damping in the numerical model was tuned to match the decay tests.

The scope of this thesis was to study the dynamic response of monopile wind turbines subjected to nonlinear wave loads. First, regular wave tests of steepnesses $s = 1/40$ and $s = 1/22$ were studied. The wave elevation was modelled by a Stokes second order wave, a linear wave and a stream function wave for wave periods ranging from $T = 6$ s to $T = 16.5$ s with intervals of $\Delta T = 0.5$ s. For waves of steepness $s = 1/40$, the Stokes second order wave and the stream function wave were able to match the measured wave. However, for waves of steepness $s = 1/22$, the Stokes second order validity range was exceeded, causing secondary peaks in the wave troughs. This was further confirmed by comparing the Ursell number of the different waves with the Ursell limit $Ur = 26$ for shallow waters. It was found that the longest wave of steepness $s = 1/22$ will exceed this limit. This implies that in order to describe all the waves of steepness $s = 1/22$ accurately, stream function waves must be used. The stream function wave in question was of order $N = 10$.

The response of the shear force and bending moment at the mudline was investigated, and four different numerical methods were compared to the response measured in the experiment. The response was filtered around the first four harmonics, resulting in contributions consisting mainly of 1ω, 2ω, 3ω and 4ω. All methods provided a fairly accurate 1st harmonic response. For the waves of steepness $s = 1/40$, the Morison model using second order kinematics provided the best estimate of the 2nd harmonic moment. However, this method severely underestimated the 3rd harmonic moment, which the FNV method and the Morison model with stream function kinematics captured better. For the waves of steepness $s = 1/22$, the finite-depth FNV method severely overestimates both 2nd and 3rd harmonic moments, while the Morison model using second order kinematics and the Morison model using stream function kinematics overestimated somewhat less. However, it should be noted that the second order wave elevation is not accurately described for the longest waves. The FNV method is expected to overestimate 3rd harmonic loads for steepnesses $s > 1/40$, which seems to be confirmed in these investigations [15]. None of the proposed numerical methods were able to capture the correct response in both 2nd and 3rd harmonic for waves of steepness $s = 1/40$ and $s = 1/22$.

20 different high-response events are identified from the measurements of an 3 hour irregular sea state of $H_s = 8.6$ m and $T_p = 11$ s. The response is filtered around the 1st and 2nd eigenfrequency, where the response will consist mainly of 1st and 2nd mode, respectively, and the residue is said to be the quasi-static response. The largest responses are found to occur when there is an excitation of the 2nd mode on top of a ringing response. The quasi-static response accounts for around $50-80\%$ of the maximum response, the 1st mode contribution is generally around 30% while the 2nd mode contribution reaches up to 20%. The wave in each event is characterized as breaking or not using video of the tests, and using calculations of the steepness. Considerable contributions of the 2nd mode response are seen even when the wave is not characterized as breaking. The events are

recreated by three different numerical methods, and the results are compared to the measurements. The first method is the Morison equation using linear kinematics obtained from the filtered wave elevation. This method provides only a quasi-static contribution to the response, which is somewhat underestimated compared to the measured quasi-static response. The next method is the Morison equation using stream function kinematics obtained from an embedded stream function wave, which was able to excite the 1st mode response. This type of response is identified as ringing due to the passing of the steep wave. In order to excite the 2nd mode, the Wienke slamming model is added.

The quasi-static response is found to be underestimated by the linear Morison model in 17/20 events, while the total response is underestimated for all events. This is due to the integration of the loads up to SWL only, and possibly due to the linearization and filtration of the measured wave elevation when given as input to the model. The Morison model with stream function kinematics proves a better estimate for the quasi-static response, but still underestimates for some of the highest measured responses, in total 8/20 events. The 1st mode response is overestimated for 14/20 events. In the case of overestimation of the 1st mode response, the wave is generally breaking. Only the Morison model with Wienke slamming model provides a contribution of the 2nd mode response, however, it is very overestimated. Due to the large 2nd mode contribution, the Morison with Wienke slamming model ends up overestimating the total response for all events. The Morison with stream function kinematics, and no slamming model, provides a fairly good match of the total response even though it does not have any 2nd mode contribution. This is due to the generally overestimated 1st mode response. Even though the total response estimated by this method ends up close to the measured one, the balance between the 1st and 2nd mode is not captured. This can lead to inaccurate stress distribution, as pointed out by Suja-Thauvin [5].

6.1 Further work

Recommended further work is to do a parameter study of the implementation of the Wienke slamming model, such as the time of impact, curling factor λ_c and time step dt. The video recordings from the experiment could be used in order to estimate the exact time of slamming, independent of whether it is the time of maximum wave elevation or not. Breaker type could also be decided from the video recording of the slamming events, which could be used to adjust the curling factor λ_c for each event.

Based on the most promising load model for regular and irregular wave tests, one could also examine comparisons for different damping coefficients. If the results are found to be acceptable, the numerical model may be used to perform a parametric study to understand the effects of having a more realistic second mode shape and of different design parameters.

References

[1] B. Verheugt, "Efficient Response Simulation Strategies for Jacket-based Offshore Wind Turbines - An integrated approach combining model reduction and nonlinear irregular wave theory," Ph.D. dissertation, Norwegian University of Science and Technology, 2014.

[2] M. Thys, E. E. Bachynski, and F. H. Dadmarzi, "Model Test Report: Wave loads and response," SINTEF Ocean AS, Tech. Rep., 2019.

[3] O. Faltinsen, *Sea loads on ships and offshore structures*. Cambridge University Press, 1990.

[4] F. H. Dadmarzi, E. E. Bachynski, and M. Thys, "Validation of Hydrodynamic Loads on a large-diameter monopile in regular waves," in *ASME 2019 38th International Conference on Ocean, Offshore and Arctic Engineering*, no. OMAE2019-95929. Glasgow, Scotland: OMAE2019, 2019.

[5] L. Suja-Thauvin, J. R. Krokstad, and E. E. Bachynski, "Critical assessment of non-linear hydrodynamic load models for a fully flexible monopile offshore wind turbine," *Ocean Engineering*, vol. 164, no. May, pp. 87–104, 2018. [Online]. Available: https://doi.org/10.1016/j.oceaneng.2018.06.027

[6] L. Suja-Thauvin, J. R. Krokstad, E. E. Bachynski, and E. J. de Ridder, "Experimental results of a multimode monopile offshore wind turbine support structure subjected to steep and breaking irregular waves," *Ocean Engineering*, vol. 146, no. December, pp. 339–351, 2017. [Online]. Available: https://doi.org/10.1016/j.oceaneng.2017.09.024

[7] C. Devriendt, W. Weijtjens, M. El-Kafafy, and G. De Sitter, "Monitoring resonant frequencies and damping values of an offshore wind turbine in parked conditions," *IET Renewable Power Generation*, vol. 8, no. 4, pp. 433–441, 2014.

[8] J. Wienke and H. Oumeraci, "Breaking wave impact force on a vertical and inclined slender pile—theoretical and large-scale model investigations," *Coastal Engineering*, vol. 52, no. 5, pp. 435–462, 2005. [Online]. Available: http://www.sciencedirect.com/science/article/pii/S0378383904001735

[9] B. T. Paulsen, H. Bredmose, H. B. Bingham, and S. Schløer, "Steep Wave Loads From Irregular Waves on an Offshore Wind Turbine Foundation: Computation and Experiment," 2013. [Online]. Available: https://doi.org/10.1115/OMAE2013-10727

[10] E. Bachynski, M. Thys, and V. Delhaye, "Dynamic response of a monopile wind turbine in waves: Experimental uncertainty analysis for validation of numerical tools," *Applied Ocean Research*, vol. 89, no. August 2018, pp. 96–114, 2019. [Online]. Available: https://doi.org/10.1016/j.apor.2019.05.002

[11] H. Bredmose, P. Slabiak, L. Sahlberg-Nielsen, and F. Schlütter, *Dynamic Excitation of Monopiles by Steep and Breaking Waves: Experimental and Numerical Study*, 2013, vol. 8. [Online]. Available: https://doi.org/10.1115/OMAE2013-10948

[12] S. Burmester, E.-J. de Ridder, C. Wehmeyer Ramboll Esbjerg, E. Asp, and P. Gujer, "Comparing different approaches for calculating wave impacts on a monopile turbine foundation." ASME, 2017. [Online]. Available: https://doi.org/10.1115/OMAE2017-61182

[13] H. Bredmose, M. Dixen, A. Ghadirian, T. J. Larsen, S. Schløer, S. J. Andersen, S. Wang, H. B. Bingham, O. Lindberg, E. D. Christensen, M. H. Vested, S. Carstensen, A. P. Engsig-Karup,

O. S. Petersen, H. F. Hansen, J. S. Mariegaard, P. H. Taylor, T. A. Adcock, C. Obhrai, O. T. Gudmestad, N. J. Tarp-Johansen, C. P. Meyer, J. R. Krokstad, L. Suja-Thauvin, and T. D. Hanson, "DeRisk - Accurate Prediction of ULS Wave Loads. Outlook and First Results," *Energy Procedia*, vol. 94, no. January, pp. 379–387, 2016. [Online]. Available: http://dx.doi.org/10.1016/j.egypro.2016.09.197

[14] O. Faltinsen, J. Newman, and T. Vinje, "Nonlinear wave loads on a slender vertical cylinder," *Journal of Fluid Mechanics*, vol. 289, pp. 179–198, 1995. [Online]. Available: https://doi.org/10.1017/S0022112095001297

[15] T. Kristiansen and O. M. Faltinsen, "Higher harmonic wave loads on a vertical cylinder in finite water depth," *Journal of Fluid Mechanics*, vol. 833, pp. 773–805, 2017. [Online]. Available: https://doi.org/10.1017/jfm.2017.702

[16] A. P. Engsig-Karup, H. B. Bingham, and O. Lindberg, "An efficient flexible-order model for 3D nonlinear water waves," *Journal of Computational Physics*, vol. 228, no. 6, pp. 2100–2118, 2009. [Online]. Available: http://www.sciencedirect.com/science/article/pii/S0021999108006190

[17] DNV GL, "DNV-RP-C205: Environmental Conditions and Environmental Loads," 2010.

[18] B. Pettersen, *Pensumhefte Marin Teknikk 3 Hydrodynamikk*. Akademika, 2017.

[19] T. L. Andersen and P. Frigaard, *Lecture notes for the course in water wave mechanics*, dce lectur ed. Aalborg: Department of Civil Engineering, Aalborg University, 2007.

[20] D. Myrhaug, *Hydrodynamikk, kapittel 5: Uregelmessig sjø*. NTNU, Akademika, 2017.

[21] L. H. Holthuijsen, *Waves in oceanic and coastal waters*. Cambridge: Cambridge University Press, 2007.

[22] M. Brorsen, *Non-linear Waves*. Aalborg: Department of Civil Engineering, Aalborg University, 2007.

[23] M. M. Rienecker and J. D. Fenton, "A Fourier approximation method for steady water waves," *Journal of Fluid Mechanics*, vol. 104, pp. 119–137, 1981. [Online]. Available: https://doi.org/10.1017/S0022112081002851

[24] S. P. Neill and M. R. Hashemi, "Fundamentals of Ocean Renewable Energy: Chapter 5 - Wave Energy," in *E-Business Solutions*. Academic Press, 2018, pp. 107–140. [Online]. Available: http://www.sciencedirect.com/science/article/pii/B9780128104484000057

[25] D. Myrhaug, "Oceanography : wind, waves," Trondheim, 2006.

[26] L. Skjelbreia and J. Hendrickson, "FIFTH ORDER GRAVITY WAVE THEORY," *Coastal Engineering Proceedings*, vol. 1, no. 7 SE - Conference Proceedings, 1 1960. [Online]. Available: https://icce-ojs-tamu.tdl.org/icce/index.php/icce/article/view/2169

[27] R. G. Dean, "Stream function representation of nonlinear ocean waves," *Journal of Geophysical Research (1896-1977)*, vol. 70, no. 18, pp. 4561–4572, 9 1965. [Online]. Available: https://doi.org/10.1029/JZ070i018p04561

[28] J. D. Fenton, "Numerical methods for nonlinear waves," in *Advances in Coastal and Ocean Engineering*, ser. Advances in Coastal and Ocean Engineering. World Scientific, 7 1999, vol. Volume 5, pp. 241–324. [Online]. Available: https://doi.org/10.1142/9789812797544_0005

[29] J. R. Morison, J. W. Johnson, and S. A. Schaaf, "The Force Exerted by Surface Waves on Piles," *Journal of Petroleum Technology*, vol. 2, no. 05, pp. 149–154, 1950. [Online]. Available: https://doi.org/10.2118/950149-G

[30] A. Mockute, E. Marino, C. Lugni, and C. Borri, "Comparison of nonlinear wave-loading models on rigid cylinders in regular waves," *Energies*, vol. 12, no. 21, 2019. [Online]. Available: https://doi.org/10.3390/en12214022

[31] J. F. Manwell, J. G. McGowan, A. L. Rogers, A. L. Manwell, and A. L. McGowan, *Wind Energy Explained: Theory, Design and Application*, 2010.

[32] C. M. Larsen, *Marine dynamics : TMR 4182 marine dynamics : Department of Marine Technology, Faculty of Engineering Science and Technology, NTNU*, Trondheim, 2012, vol. UK-2012-10.

[33] I. Langen, *Dynamisk analyse av konstruksjoner*, R. Sigbjörnsson, Ed. Trondheim: Tapir, 1979.

[34] S. Steen, *Experimental methods in marine hydrodynamics : compendium*, rev. ed. ed., N. t.-n. u. M. senter and N. t.-n. u. I. f. m. teknikk, Eds. Trondheim: Akademika forlag Kompendieforlaget, 2014.

[35] E. E. Bachynski, C. Pakozdi, A. Ostman, and C. T. Stansberg, "Computational Fluid Dynamics Reproduction of Nonlinear Loads on a Vertical Column During Extreme Irregular Wave Events," *Journal of Offshore Mechanics and Arctic Engineering*, vol. 140. [Online]. Available: https://doi.org/10.1115/1.4040442

[36] MARINTEK, "MARINTEK Fact sheet SIMA," 2014. [Online]. Available: https://www.sintef.no/globalassets/upload/marintek/software/sima.pdf

[37] P. J. Rainey and T. R. Camp, "Constrained non-linear waves for offshore wind turbine design," *Journal of Physics: Conference Series*, vol. 75, p. 12067, 2007. [Online]. Available: http://dx.doi.org/10.1088/1742-6596/75/1/012067

[38] T. B. Johannessen, "On the Use of Linear and Weakly Nonlinear Wave Theory in Continuous Ocean Wave Spectra: Convergence With Respect to Frequency," pp. 211–217, 6 2008. [Online]. Available: https://doi.org/10.1115/OMAE2008-57355

[39] L. Suja-Thauvin and J. R. Krokstad, "Simplified Bottom Fixed Offshore Wind Turbine in Extreme Sea States," Rhodes, Greece, p. 8, 2016. [Online]. Available: https://www.onepetro.org/conference-paper/ISOPE-I-16-468

[40] J. D. Fenton, "John Fenton's Homepage," 2020. [Online]. Available: http://johndfenton.com/

[41] L. Suja-Thauvin, "Response of Monopile Wind Turbines to Higher Order Wave Loads," Ph.D. dissertation, NTNU, 2019. [Online]. Available: https://ntnuopen.ntnu.no/ntnu-xmlui/handle/11250/2641679

[42] J. M. Peeringa, "Stream Function program user manual," ECN-C–05-028, Tech. Rep. February, 2005. [Online]. Available: https://publicaties.ecn.nl/PdfFetch.aspx?nr=ECN-C--05-028

[43] R. A. Dalrymple, "Stream Function Wave Theory," 1996. [Online]. Available: http://homepages.cae.wisc.edu/~chinwu/Coastal_Java/streamless.html

[44] R. G. Dean and R. A. Dalrymple, *Water Wave Mechanics for Engineers and Scientists*. WORLD SCIENTIFIC, 1 1991, vol. Volume 2. [Online]. Available: https://doi.org/10.1142/1232

Appendices

A Events: Wave elevation and response from experiment

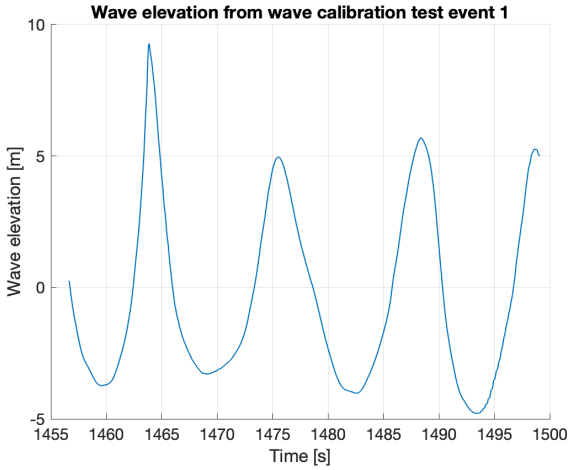

(a) Event 1: Wave elevation

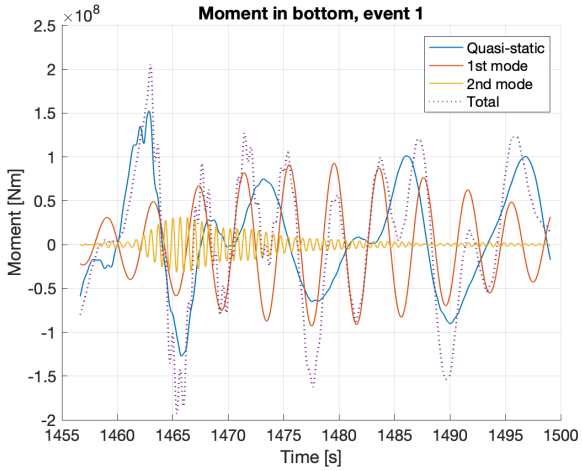

(b) Event 1: Response

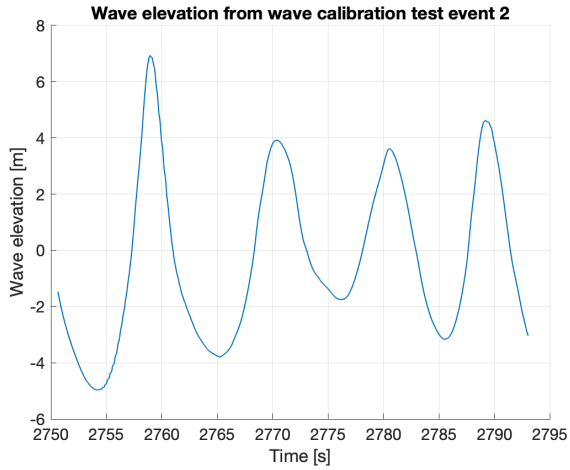

(c) Event 2: Wave elevation

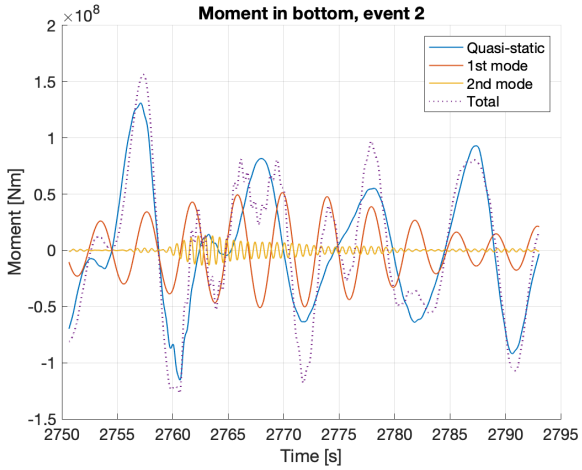

(d) Event 2: Response

Figure A.1: Wave elevation and response for events

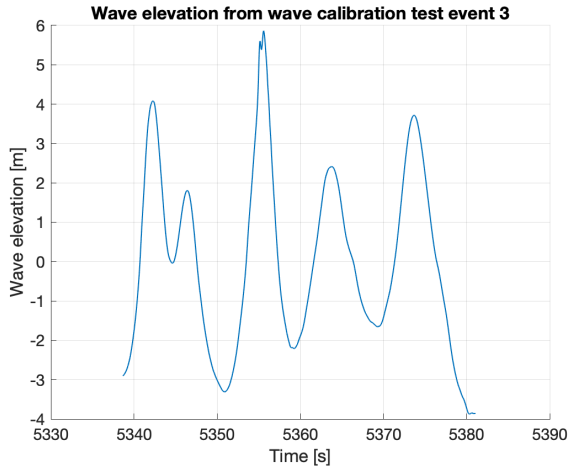

(e) Event 3: Wave elevation

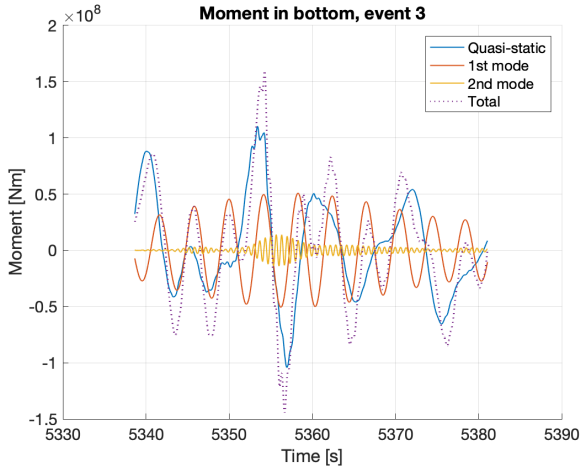

(f) Event 3: Response

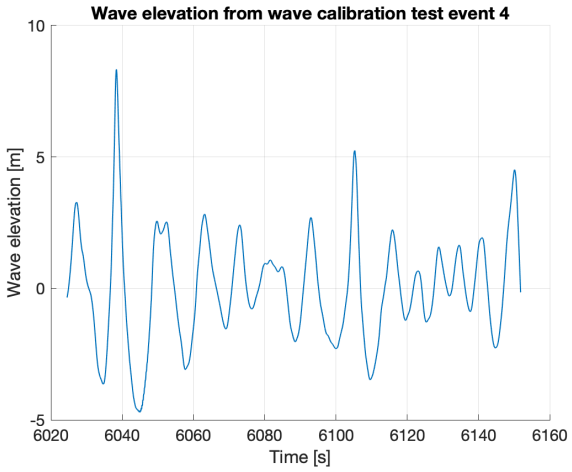

(g) Event 4: Wave elevation

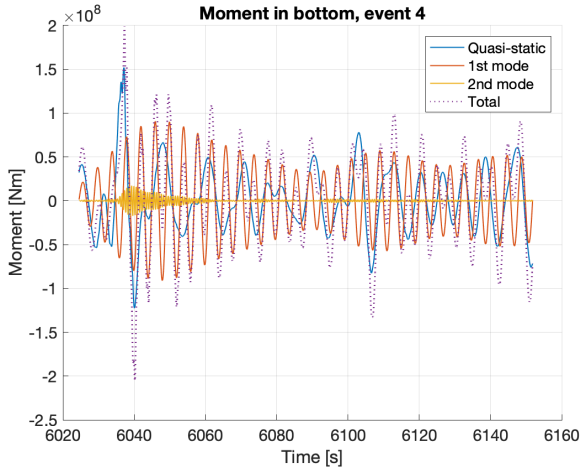

(h) Event 4: Response

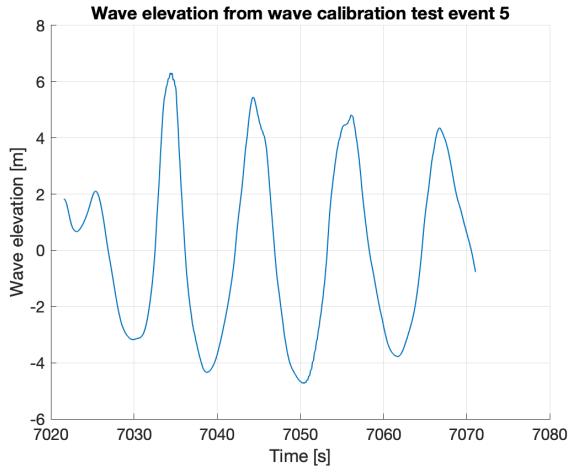

(i) Event 5: Wave elevation

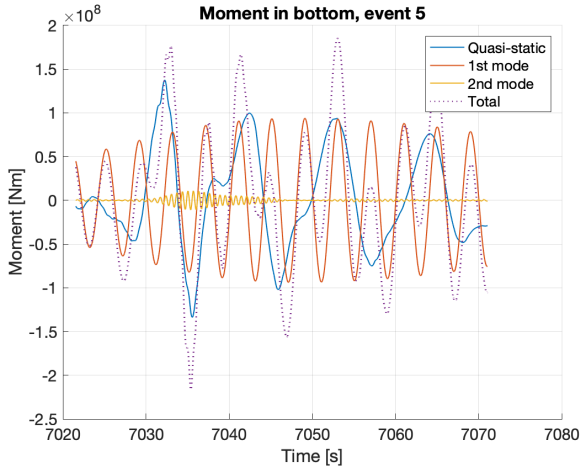

(j) Event 5: Response

Figure A.1: Wave elevation and response for events (cont.)

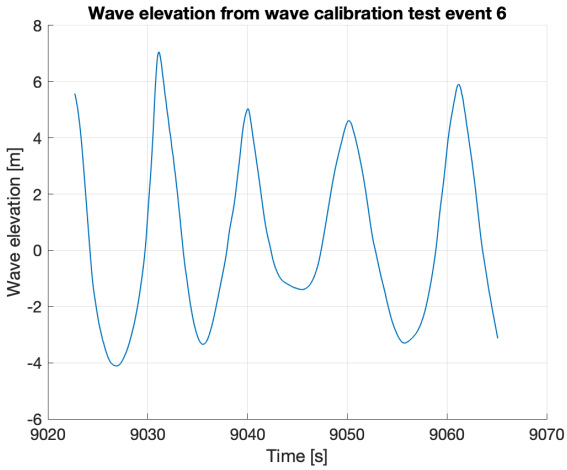

(k) Event 6: Wave elevation

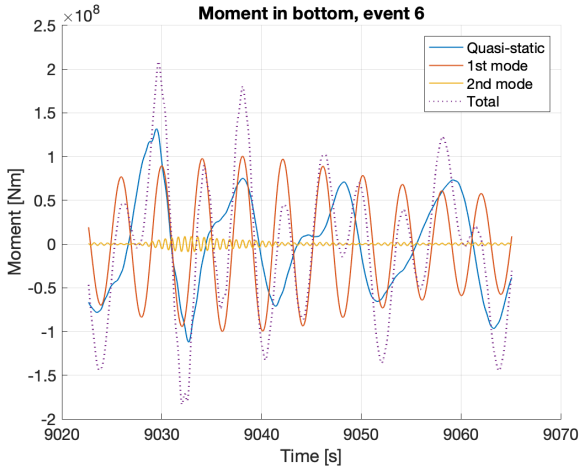

(l) Event 6: Response

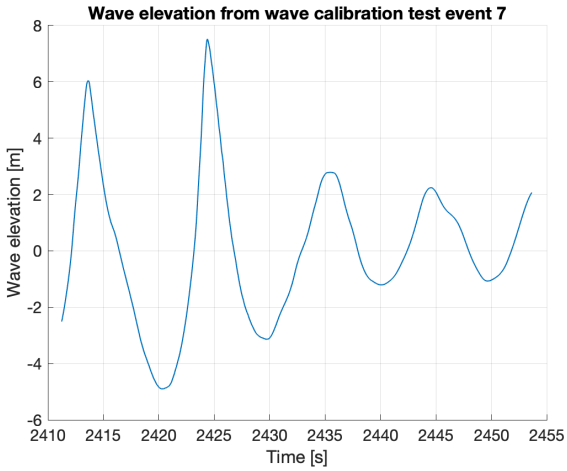

(m) Event 7: Wave elevation

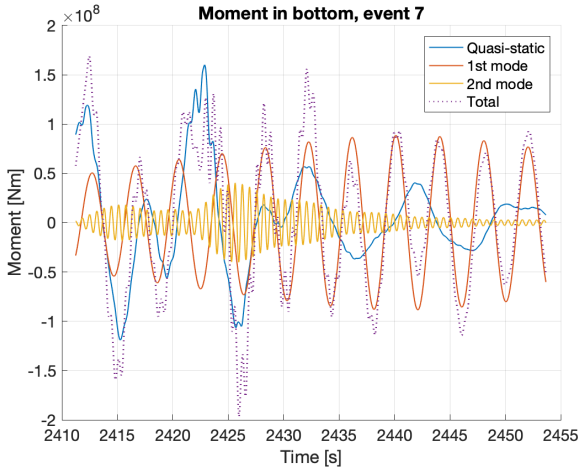

(n) Event 7: Response

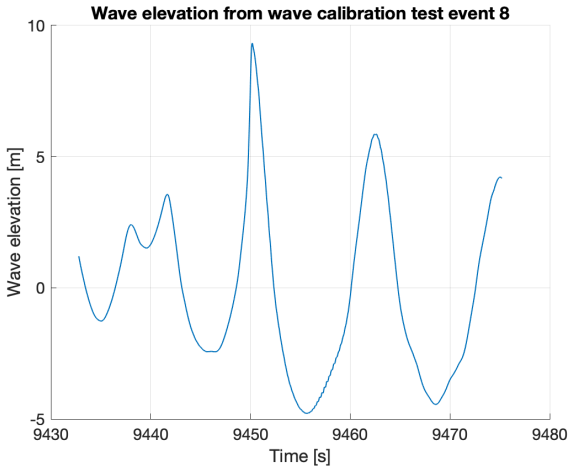

(o) Event 8: Wave elevation

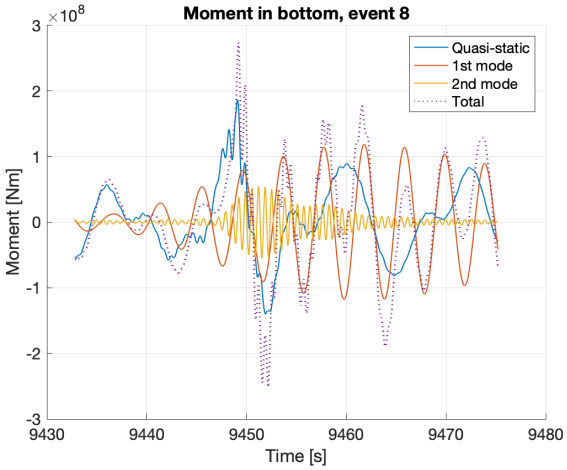

(p) Event 8: Response

Figure A.1: Wave elevation and response for events (cont.)

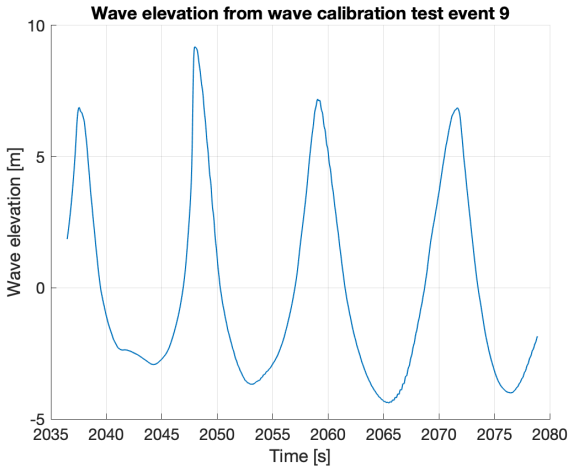

(q) Event 9: Wave elevation

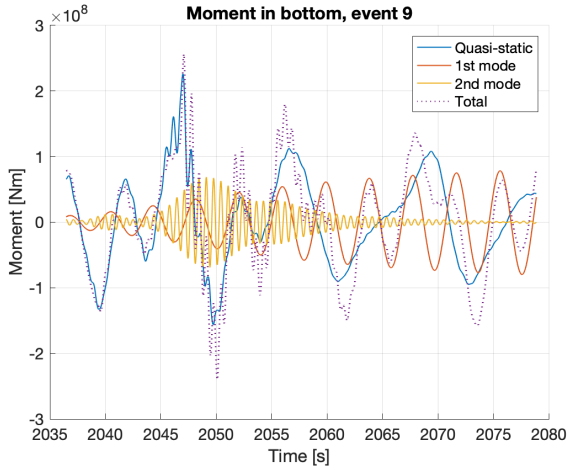

(r) Event 9: Response

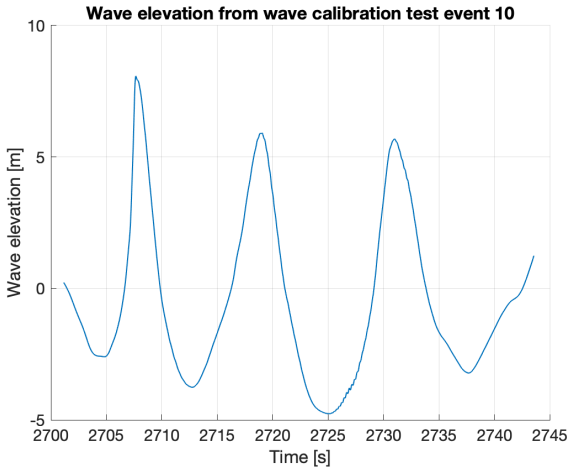

(s) Event 10: Wave elevation

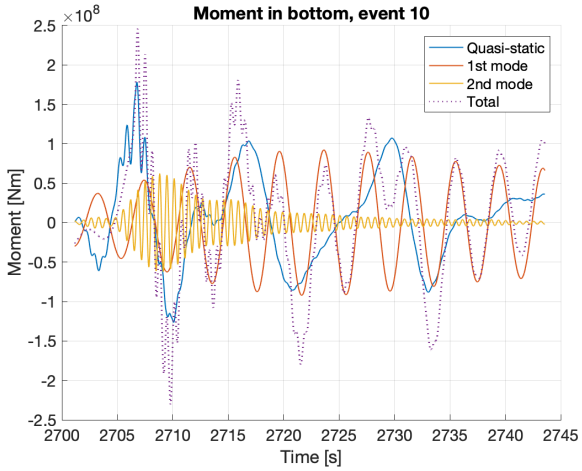

(t) Event 10: Response

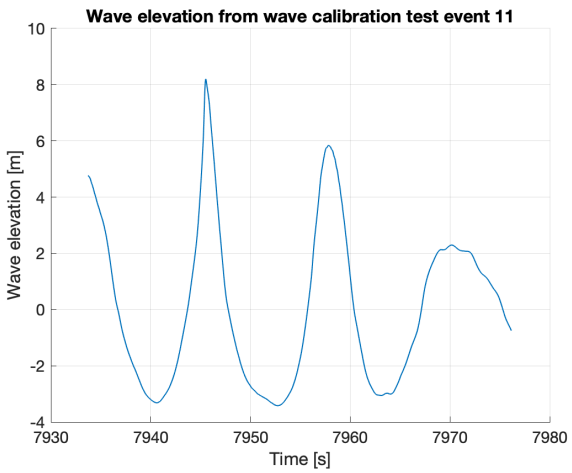

(u) Event 11: Wave elevation

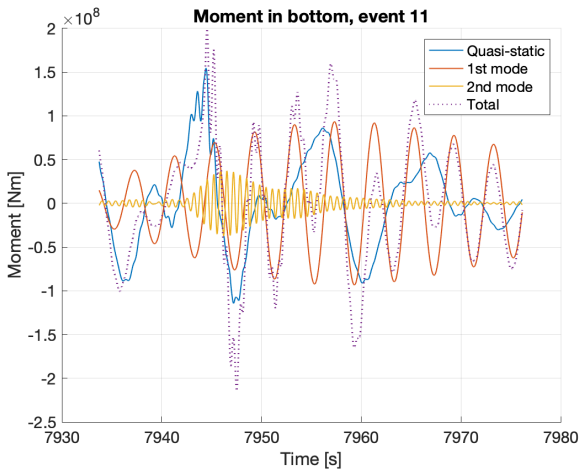

(v) Event 11: Response

Figure A.1: Wave elevation and response for events (cont.)

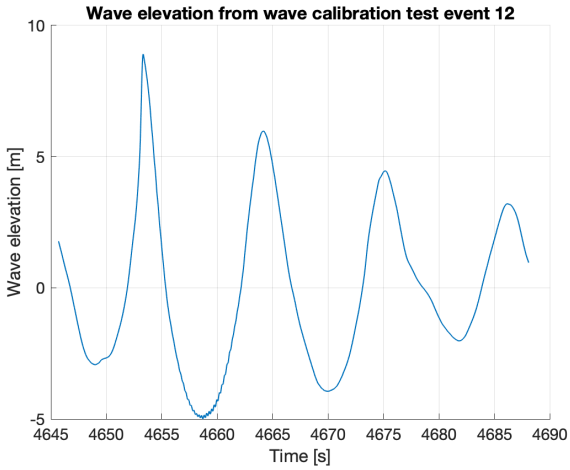

(w) Event 12: Wave elevation

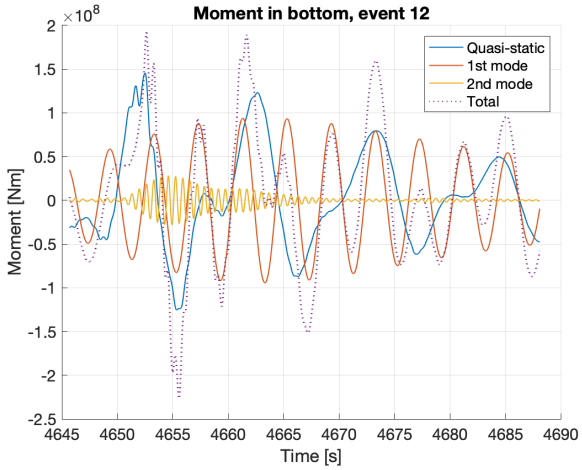

(x) Event 12: Response

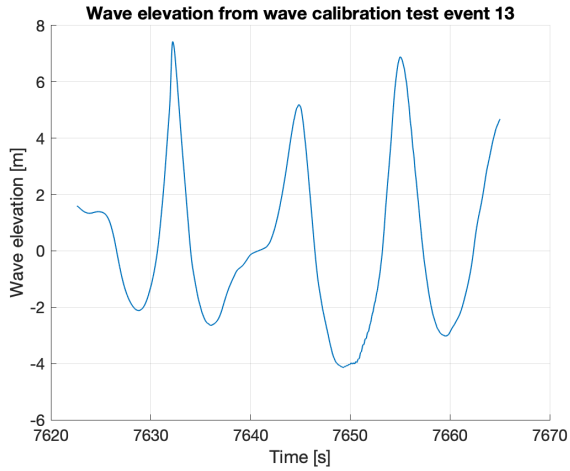

(y) Event 13: Wave elevation

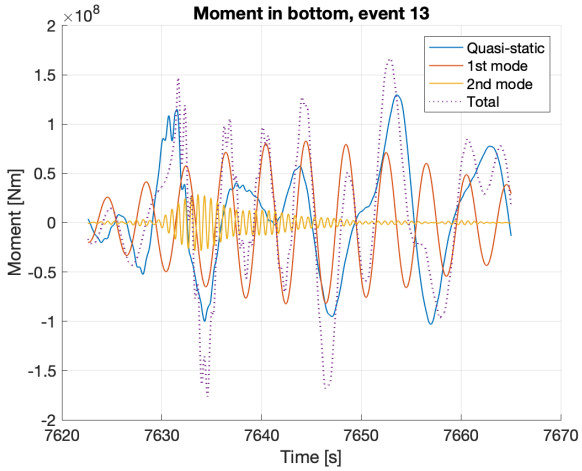

(z) Event 13: Response

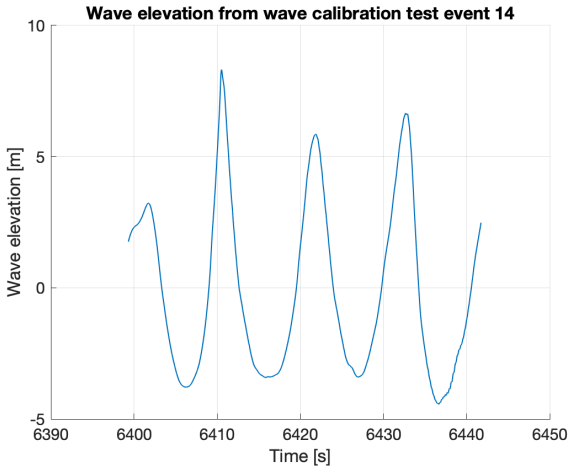

() Event 14: Wave elevation

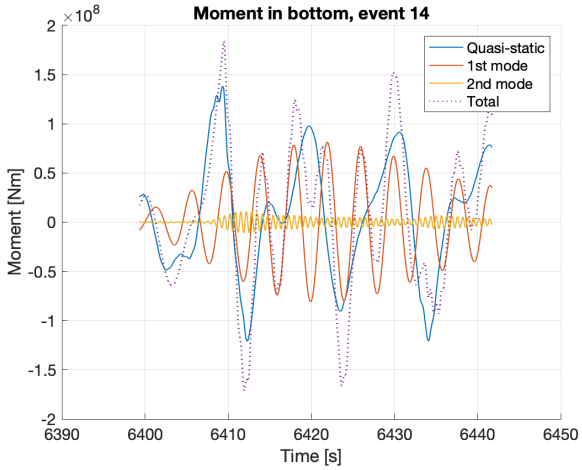

() Event 14: Response

Figure A.1: Wave elevation and response for events (cont.)

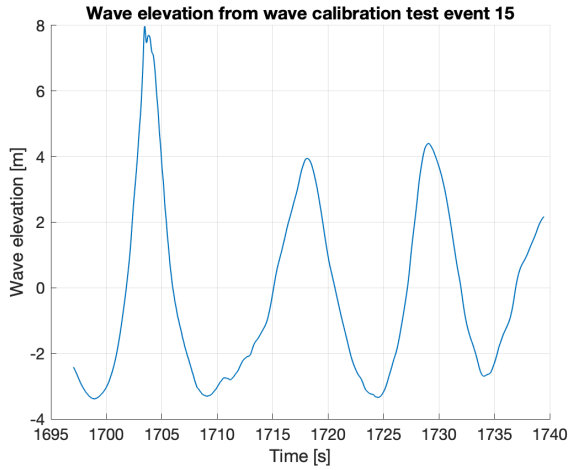

() Event 15: Wave elevation

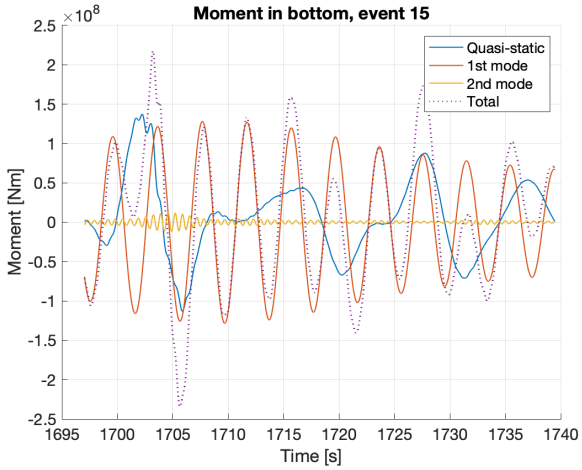

() Event 15: Response

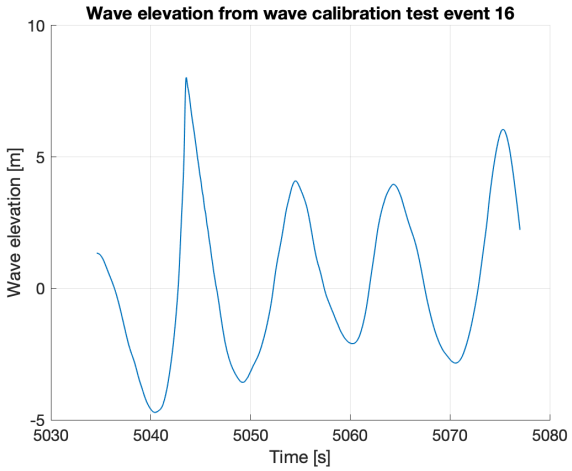

() Event 16: Wave elevation

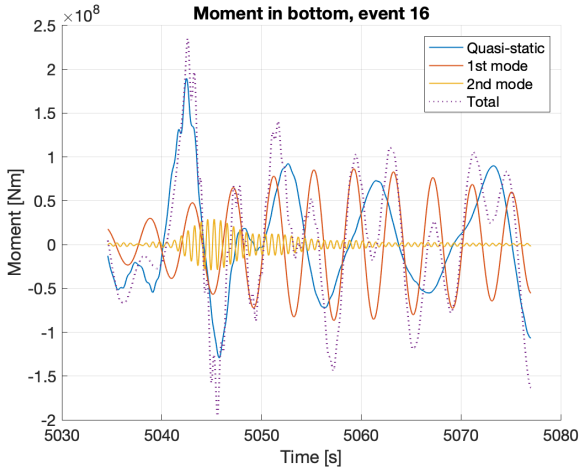

() Event 16: Response

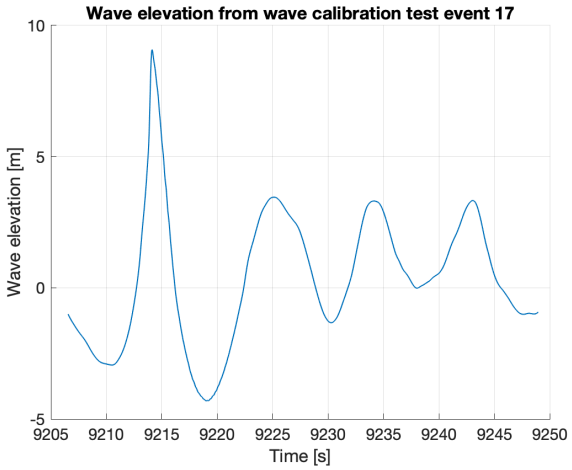

() Event 17: Wave elevation

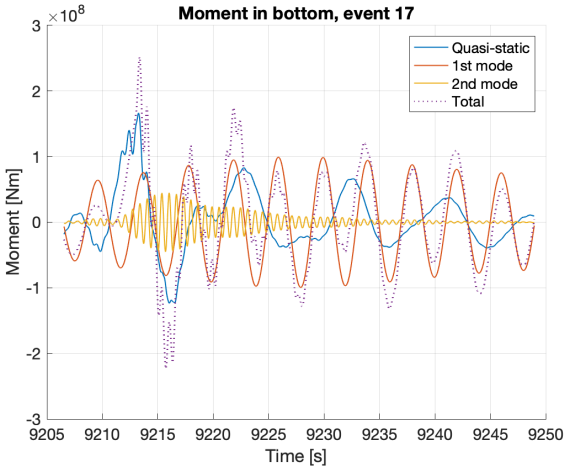

() Event 17: Response

Figure A.1: Wave elevation and response for events (cont.)

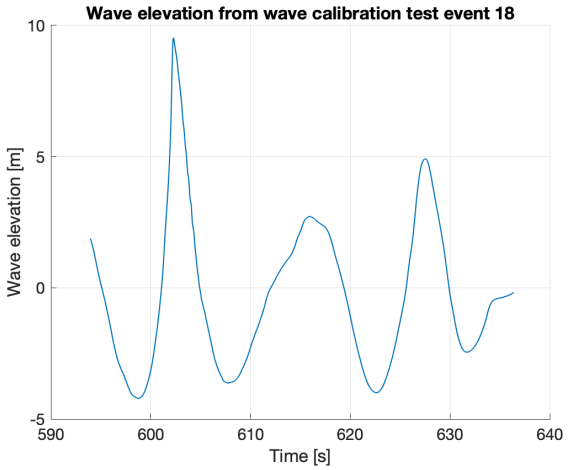

() Event 18: Wave elevation

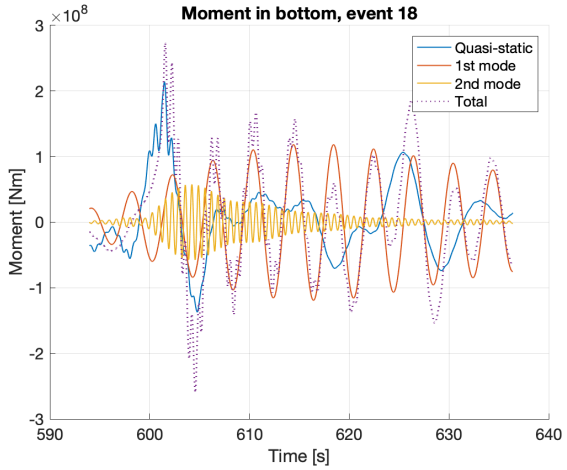

() Event 18: Response

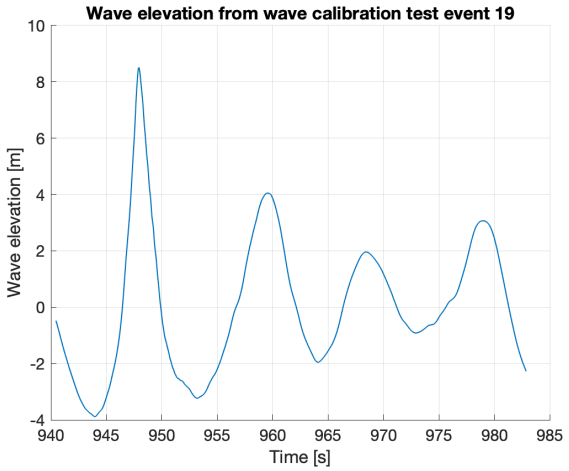

() Event 19: Wave elevation

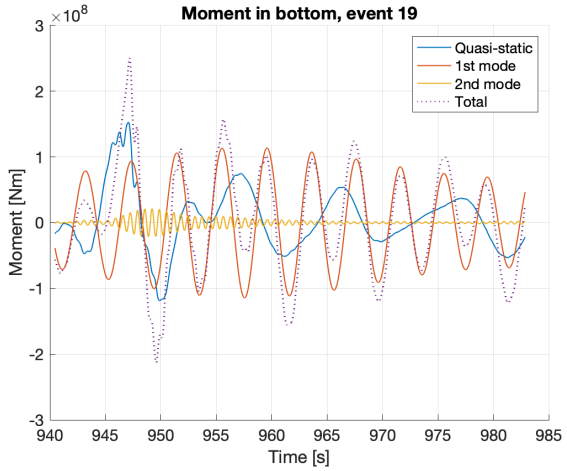

() Event 19: Response

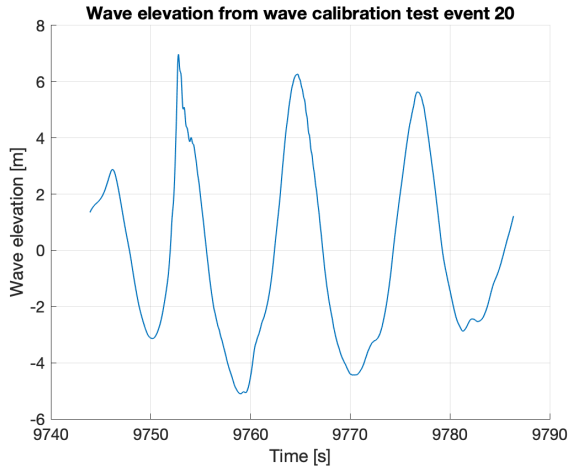

() Event 20: Wave elevation

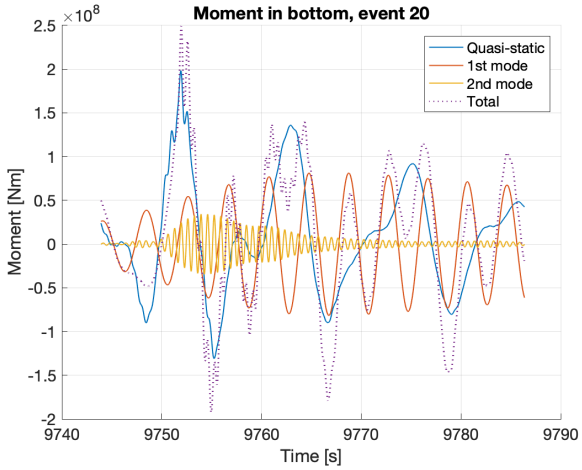

() Event 20: Response

Figure A.1: Wave elevation and response for events (cont.)

B Events: Video snapshots from experiment

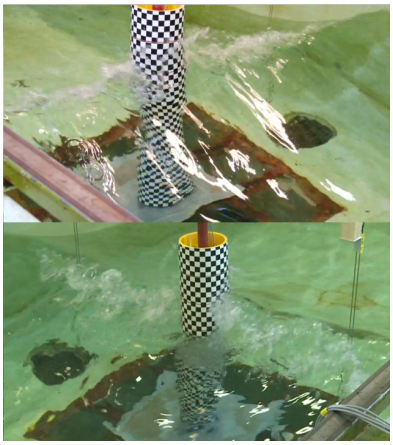

(a) Event 1

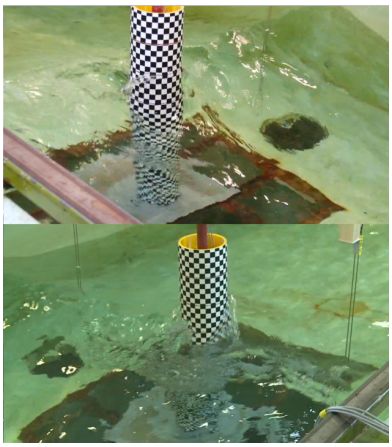

(b) Event 2

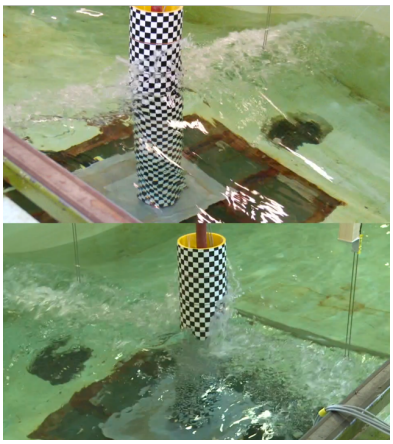

(c) Event 3

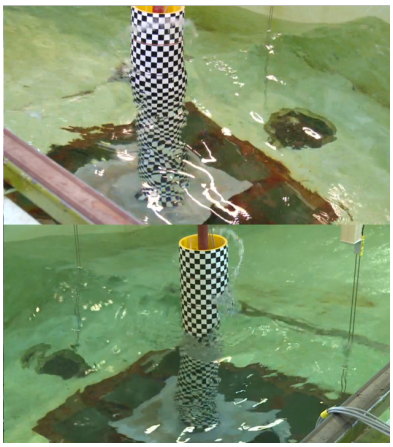

(d) Event 4

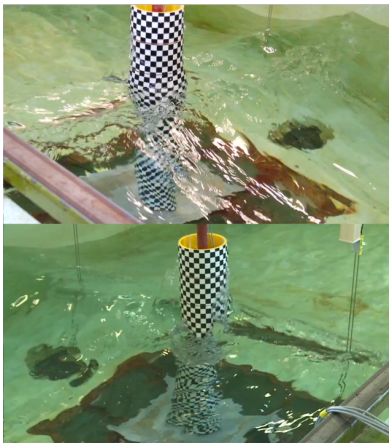

(e) Event 5

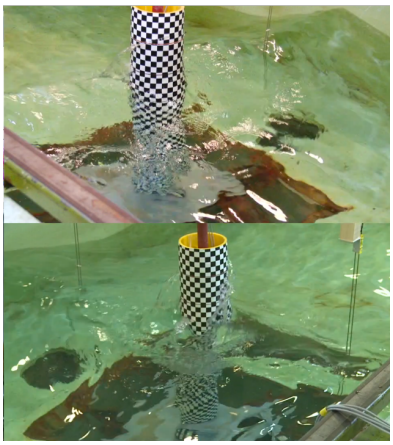

(f) Event 6

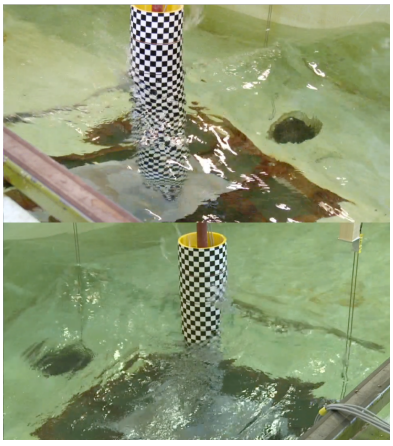

(g) Event 7

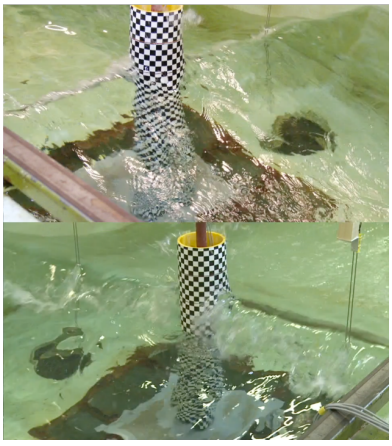

(h) Event 8

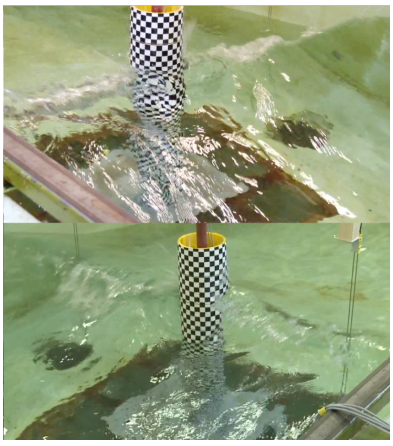

(i) Event 9

Figure B.1: Video snapshot of events

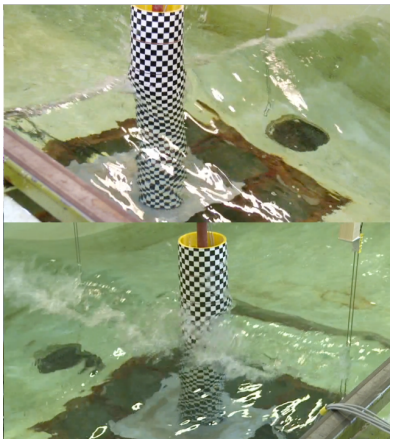

(j) Event 10

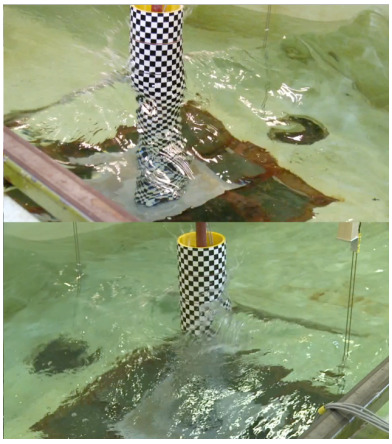

(k) Event 11

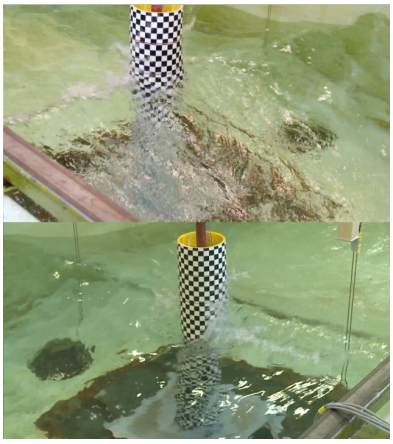

(l) Event 12

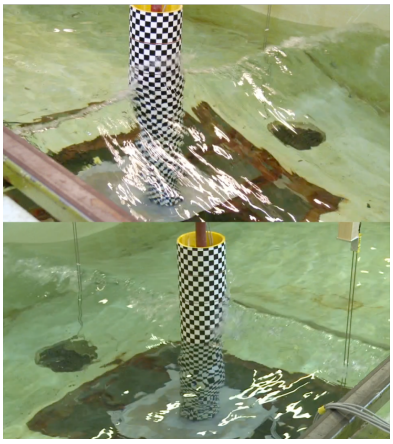

(m) Event 13

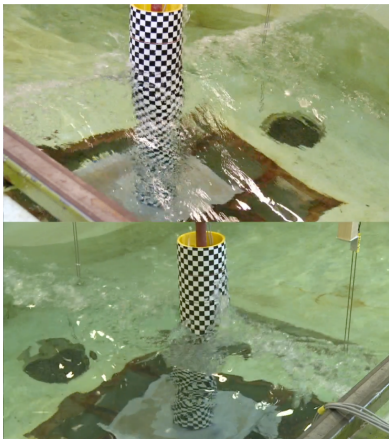

(n) Event 14

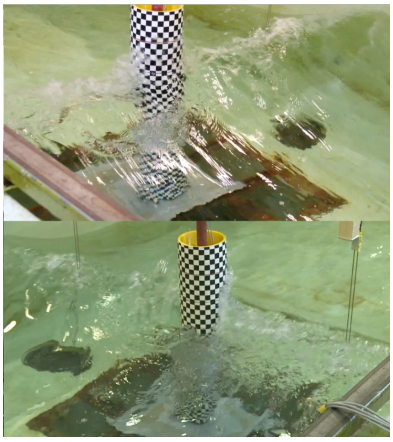

(o) Event 15

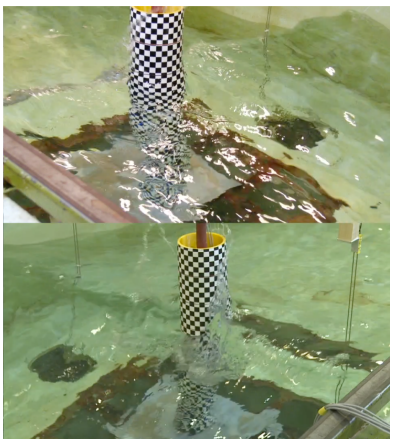

(p) Event 16

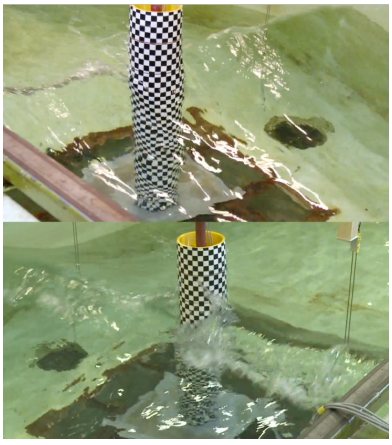

(q) Event 17

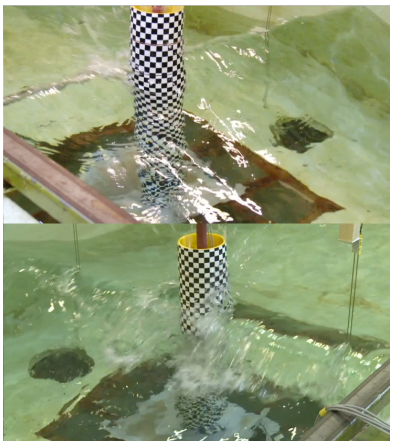

(r) Event 18

Figure B.1: Video snapshot of events (cont.)

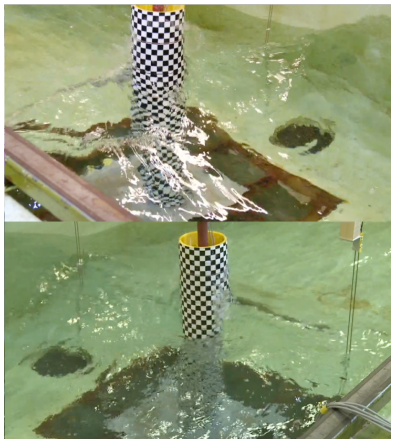

(s) Event 19

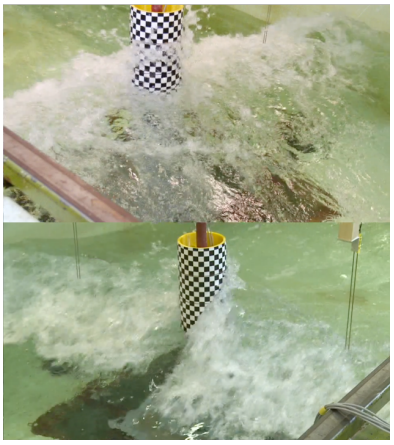

(t) Event 20

Figure B.1: Video snapshot of events (cont.)

C Events: Characterization from experiment

Table C.1: Event characterization from experiment

						Contribution		
Event	**seed**	**Steepness** [m/s]	**Slamming**	**Breaking**	**Max moment** [Nm]	**Quasi-Static** [%]	**1st mode** [%]	**2nd mode** [%]
1	201	10.04	Yes	Yes	2.060E+08	67.3	22.7	8.5
2	201	5.85	No	No	1.564E+08	78.7	20.2	1.0
3	201	3.67	Yes	Yes	1.599E+08	62.1	30.1	6.7
4	201	6.74	Yes	No	-2.054E+08	58.4	33.4	7.8
5	201	5.20	Yes	No	-2.165E+08	60.6	34.8	3.8
6	201	7.59	Yes	No	2.089E+08	58.1	39.3	2.2
7	202	9.36	Yes	No	-1.967E+08	51.8	30.2	16.4
8	203	12.60	Yes	Yes	2.738E+08	61.3	23.6	13.9
9	205	27.83	Yes	Yes	2.562E+08	80.7	-1.1	19.1
10	205	12.95	Yes	Yes	2.460E+08	65.3	15.1	16.8
11	207	6.67	Yes	No	-2.144E+08	50.4	33.1	15.7
12	208	14.87	Yes	Yes	-2.265E+08	54.6	33.3	11.9
13	208	5.18	Yes	Yes	-1.765E+08	49.0	35.0	14.9
14	209	5.53	Yes	Yes	1.844E+08	70.0	25.9	3.4
15	210	5.30	Yes	Yes	-2.346E+08	44.0	53.6	2.3
16	210	17.00	Yes	No	2.349E+08	77.3	15.9	6.8
17	210	13.61	Yes	Yes	2.517E+08	59.9	26.9	11.5
18	214	13.04	Yes	Yes	2.733E+08	72.9	12.8	13.3
19	216	6.64	Yes	No	2.506E+08	55.6	36.9	6.3
20	216	13.09	Yes	Yes	2.494E+08	76.6	12.5	9.0
21	217	9.65	Yes	No	2.344E+08	60.9	33.2	5.5
22	218	19.93	Yes	Yes	-2.528E+08	49.5	30.9	18.8
Mean		**10.56**			**2.231E+08**	**63.6**	**27.2**	**9.8**

D Events: Results from numerical estimations

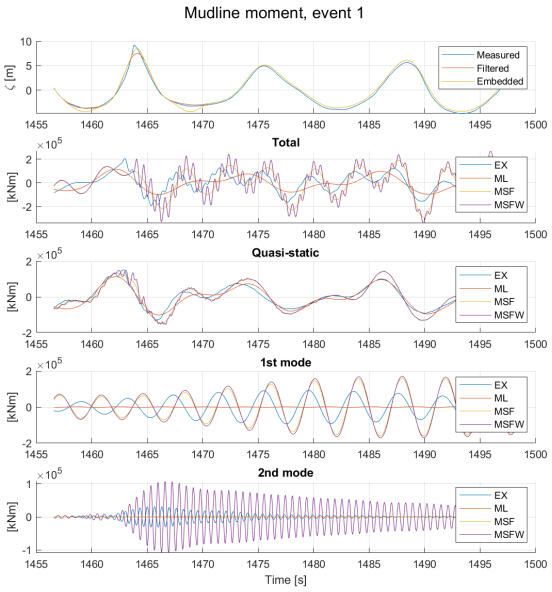

(a) Event 1

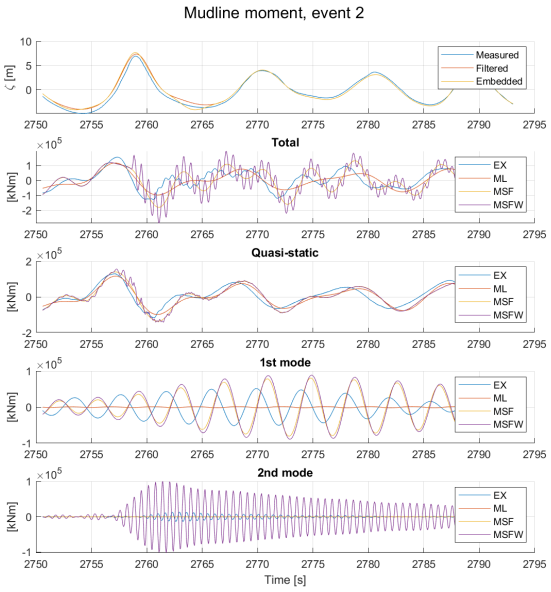

(b) Event 2

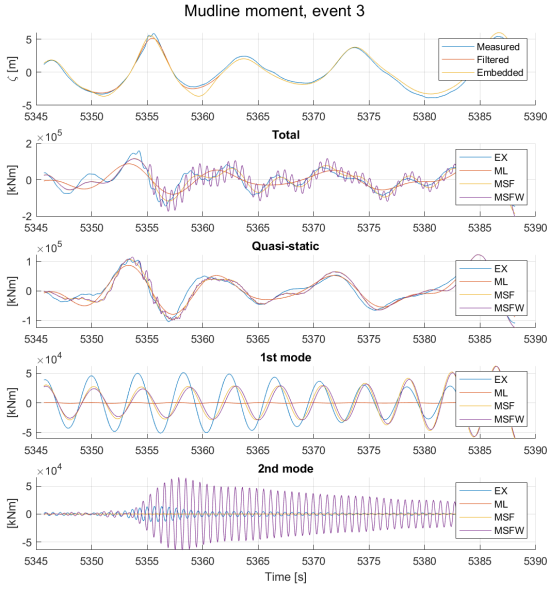

(c) Event 3

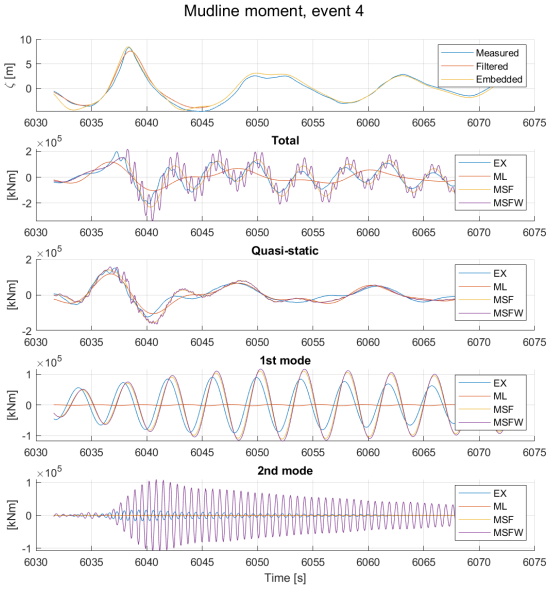

(d) Event 4

Figure D.1: Measured and simulated wave elevation and response

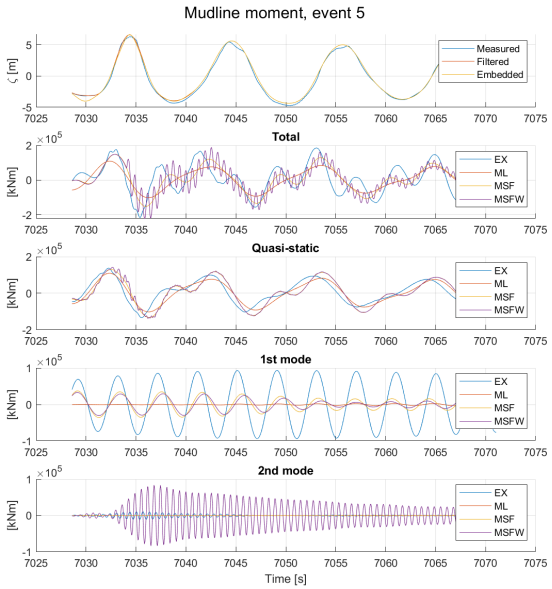

(e) Event 5

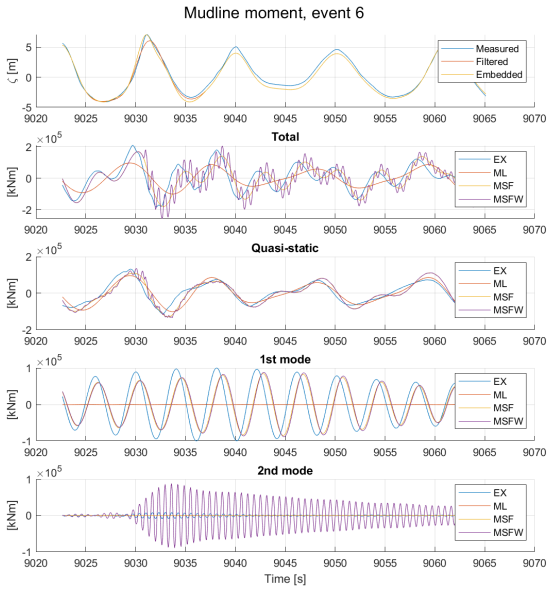

(f) Event 6

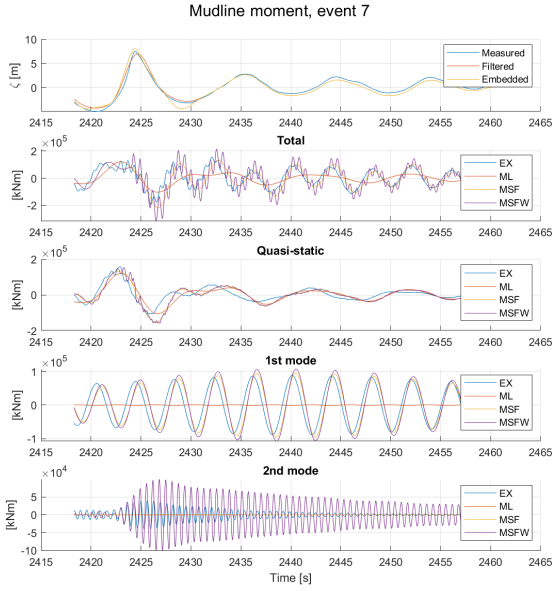

(g) Event 7

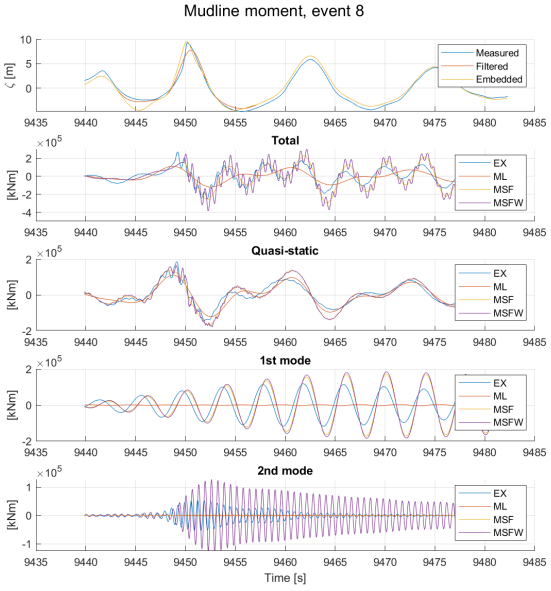

(h) Event 8

Figure D.1: Measured and simulated wave elevation and response (cont.)

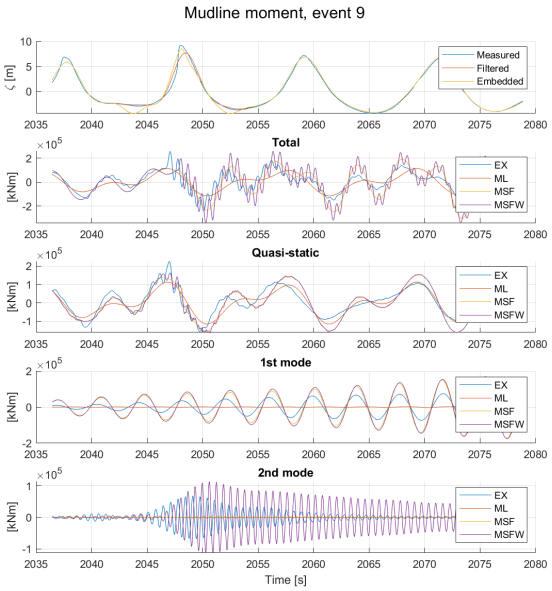

(i) Event 9

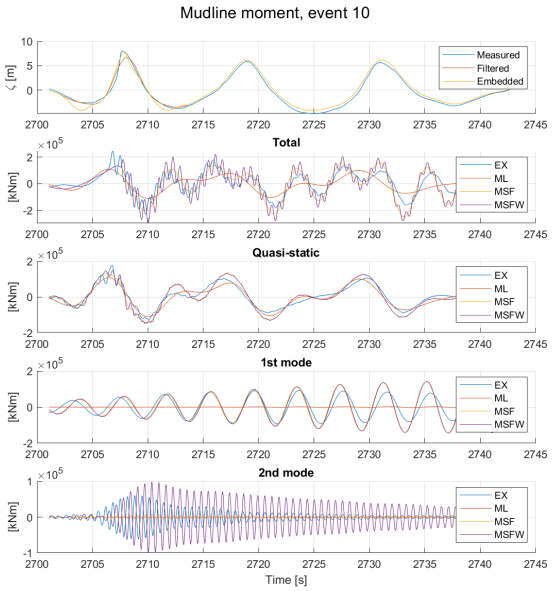

(j) Event 10

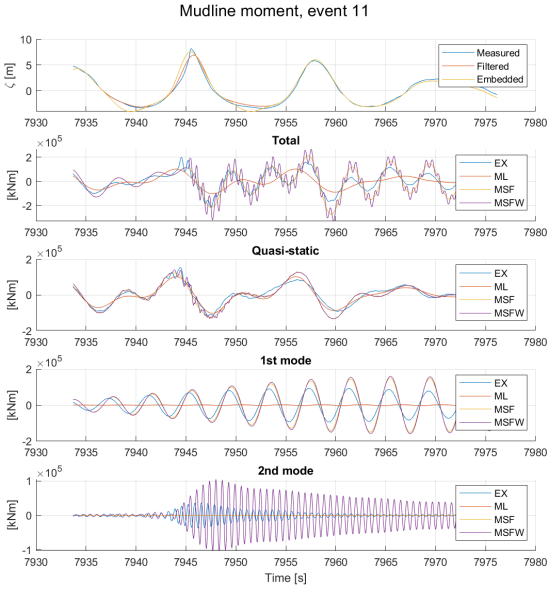

(k) Event 11

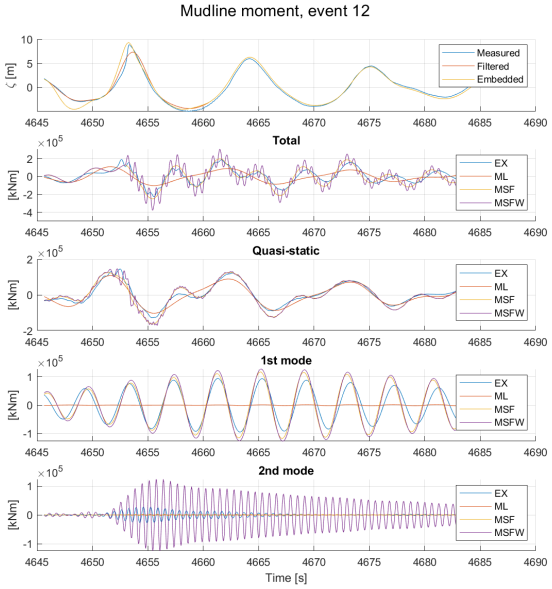

(l) Event 12

Figure D.1: Measured and simulated wave elevation and response (cont.)

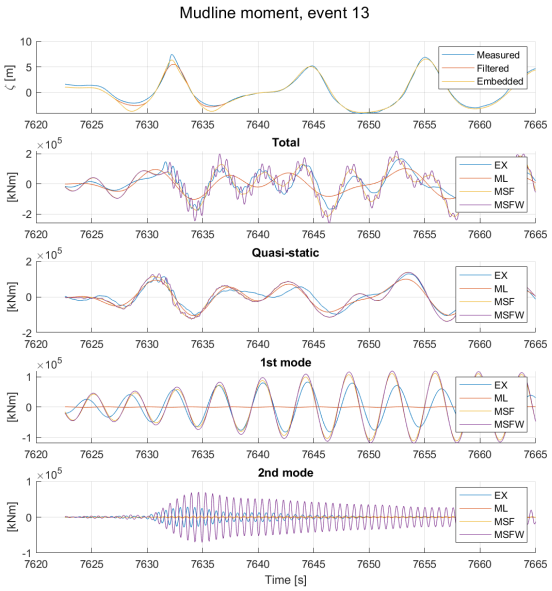

(m) Event 13

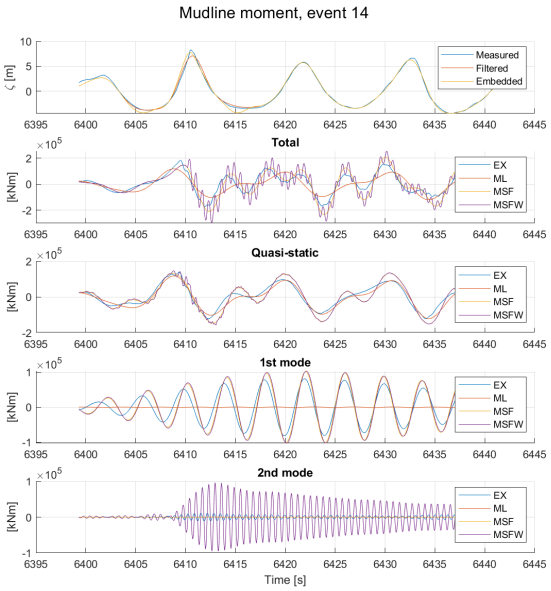

(n) Event 14

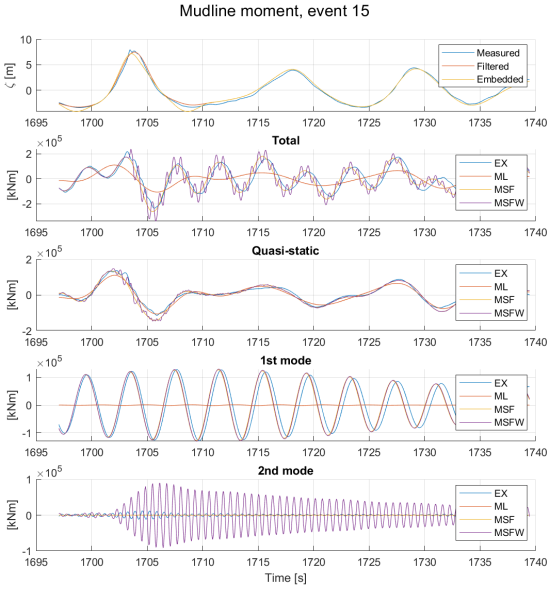

(o) Event 15

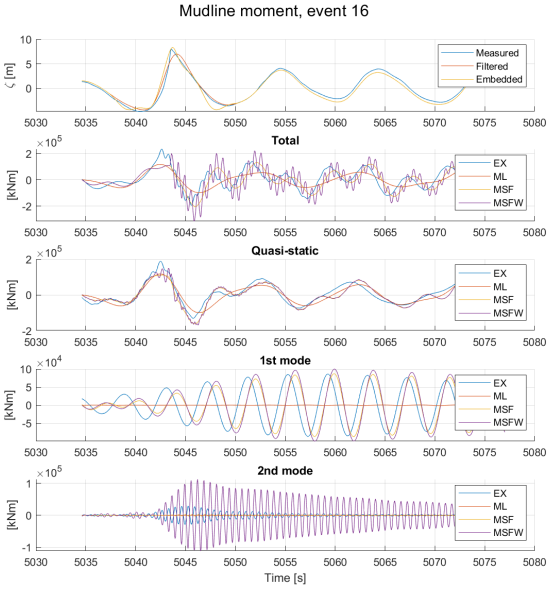

(p) Event 16

Figure D.1: Measured and simulated wave elevation and response (cont.)

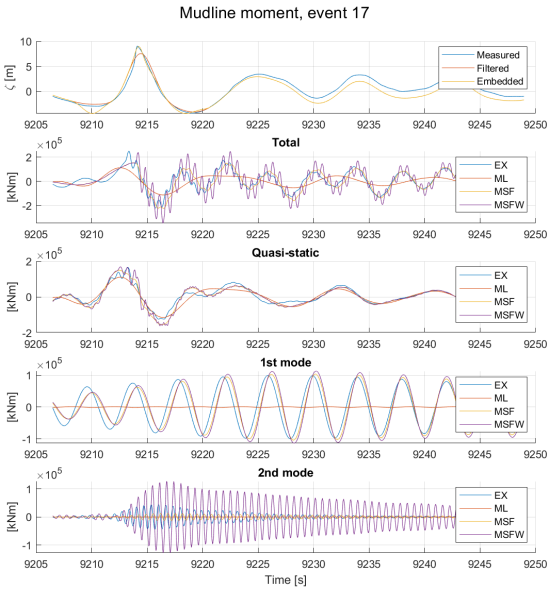

(q) Event 17

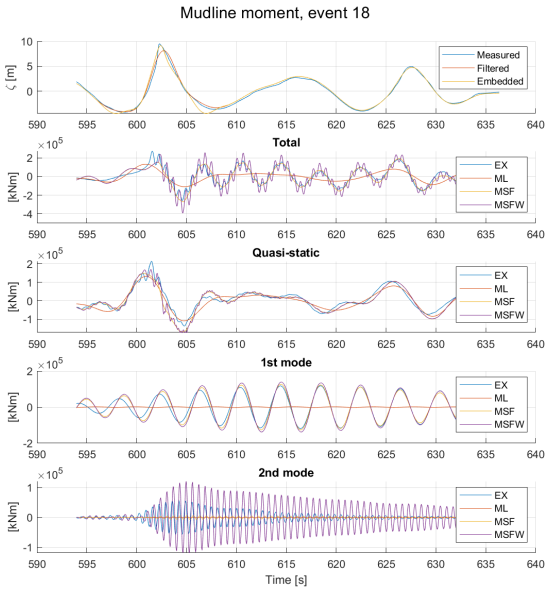

(r) Event 18

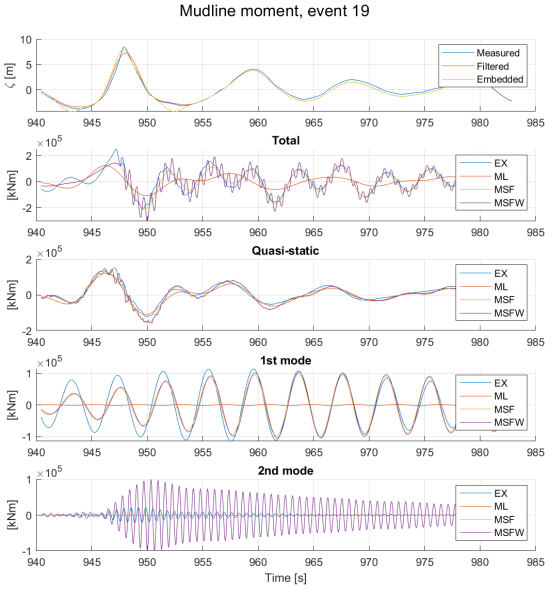

(s) Event 19

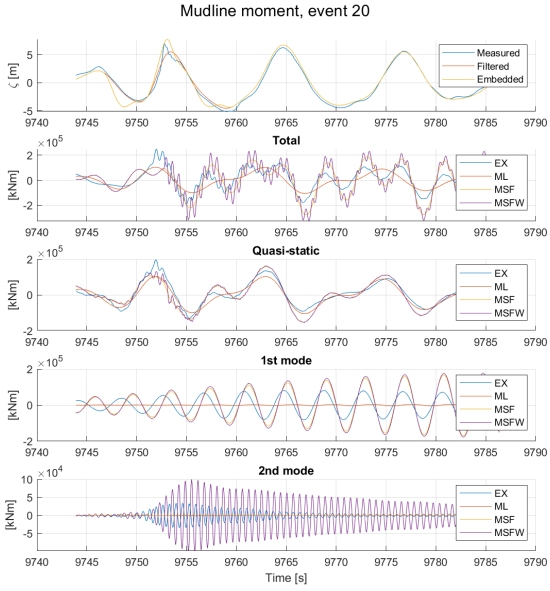

(t) Event 20

Figure D.1: Measured and simulated wave elevation and response (cont.)

E Scripts: Regular wave input

Morison_reg.m

```
%========================================================================
%   NAME:       Morison_reg.m
%
%   PURPOSE:    Generate nodal load force files for regular wave tests
%
%   BY:         Elise Moen 02.06.20,
%
%   COMMENT:    User can select between linear kinematics or stream
%               function kinematics and write to input file. Altering
%               between steepness S40 and S22 must be done manually
%
%========================================================================

%% Choose run and options
%========================================================================
iMethod = 2; % 1 - Linear, 2 - Stream function
iInputfile = 1;
for r = 1:22;

    %% Input data
    %========================================================================
    Hvec = [1.398,1.632,1.872,2.118,2.364,2.610,2.854,3.096,3.334,3.572,3.806,...
        4.036,4.266,4.494,4.720,4.944,5.168,5.390,5.610,5.830,6.048,6.264]; %S40
    %  Hvec =[2.5430,2.9655,3.4034,3.8493,4.2977,4.7448,5.1887,5.6281,6.0629,6.4929,...
    %
        6.9185,7.3399,7.7574,8.1714,8.5823,8.9903,9.3956,9.7986,10.1994,10.5982,10.9953,11.3907];
         %S22
    Tvec = [6:0.5:16.5];

    D = 9; % Diameter (m)
    a = D/2; % Radius (m)
    h = 27; % Water depth (m)
    rho = 1025; % Sea water density (kg/m^3)
    g = 9.81; % Gravitational acceleration (m/s^2)
    T = Tvec(r); % Wave period (s)
    H = Hvec(r); % Wave height (m)
    zeta_a = H/2; % Wave amplitude (m)
    omega = 2*pi/T; % Circual frequency
    Cm = 2; % Mass coefficient
    Cd = 1; % Drag coefficient

    z_sima = [103.9:0.98:108.8 109.3:0.98:114.2 114.7:0.98:119.6 120.1:0.98:125
        125.5:0.98:130.4 130.9:0.98:135.8 136.3:0.98:141.2 141.7:1.225:144.15];
    z = -(z_sima-117.64);
    nnode = length(z)-1;
    dt = 0.01; % Time step
    Np = 60;
    t = [0:dt:Np*T]; % Length of time series
    x = 0; % At centre of model

    %% Wave kinematics

    if iMethod == 1; % Linear wave kinematics
        lambda = 10; % Inital value
        err = 1; % Initial value
        while(err > 0.00001)
```

```
54              lambda1 = (g/(2*pi)*T^2)*tanh(2*pi*h/lambda);
55              err = abs(lambda-lambda1);
56              lambda = lambda1;
57          end
58          k = 2*pi/lambda; % Wave number
59
60          % Load and filter wave elevation
61          charidw = '8900';
62          loadname = [charidw '_' num2str(r) '.mat']
63          load(loadname);
64          scale = 50;
65          Wave_elev = Datawseed(:,13)*scale;
66          dt_old = (Datawseed(2,1)-Datawseed(1,1))*sqrt(scale);
67          Timewseed = [0:(Datawseed(2,1)-Datawseed(1,1)):(length(Datawseed(:,1))-1)*(
                Datawseed(2,1)-Datawseed(1,1))];
68          Time = Timewseed'*sqrt(scale);
69
70          fs = 1/T;
71          fhigh=fs*1.2;
72          flow=fs*0.8;
73
74          Wave_elev_f = bpass(Wave_elev,dt_old,flow,fhigh);
75          Timer = 0:dt:Time(end);
76
77          zeta = interp1(Time, Wave_elev_f, Timer);
78
79          for tt=1:length(t)
80              for zz=1:nnode
81                  u(zz,tt) = omega*zeta_a.*cosh(k*(z(zz)+h))./(sinh(k*h)).*sin(omega*t(tt)-
                        k*x);
82                  dudt(zz,tt) =omega^2*zeta_a.*cosh(k*(z(zz)+h))/(sinh(k*h)).*cos(omega*t(
                        tt)-k*x);
83              end
84          end
85          DUDT = dudt;
86      elseif iMethod ==2; % Stream function kinematics
87          d = h;
88          LorTandU = [T 0 1];
89          N = 10;
90          Hsteps = 20;
91          Npos = T*10;
92          plt = 0;
93          [eta,B,Ubar,k,Q,R] = fenton(H,d,LorTandU,N,Hsteps,Npos,plt)
94          c = Ubar;
95
96          % Stream function wave elevation
97          eta2 = flip(eta(2,:));
98          whole_wave = [eta(2,:) eta2(2:end-1)]-h;
99          zeta_temp = zeros(length(whole_wave)*Np,1);
100         for i=0:Np-1
101             zeta_temp(i*length(whole_wave)+1:((i+1)*length(whole_wave)))=whole_wave(1:end
                    );
102         end
103         time_temp=eta(1,:)/c;
104         dt_temp = time_temp(end)-time_temp(end-1);
105         time_temp1 = [time_temp(1):dt_temp:Np*T];
106
107         zeta = interp1(time_temp1(1:length(zeta_temp)),zeta_temp,t); % Sample to same as
                rest
108
```

```
109         for tt = 1:length(t);
110             for zz = 1:nnode;
111                 for j = 1:N;
112                     u_temp(j) = j*B(j)*cosh(j*k*(z(zz)+h))/cosh(j*k*h)*cos(j*k*(x-c*t(tt)
                            ));
113                     w_temp(j) = j*B(j)*sinh(j*k*(z(zz)+h))/cosh(j*k*h)*sin(j*k*(x-c*t(tt)
                            ));
114 
115                     dudt_temp(j) = j*B(j)*cosh(j*k*(z(zz)+h))/cosh(j*k*h)*j*k*c*sin(j*k*(
                            x-c*t(tt)));
116                     dudx_temp(j) = j*B(j)*cosh(j*k*(z(zz)+h))/cosh(j*k*h)*j*k*(-1)*sin(j*
                            k*(x-c*t(tt)));
117                     dudz_temp(j) = j*B(j)*j*k*sinh(j*k*(z(zz)+h))/cosh(j*k*h)*cos(j*k*(x-
                            c*t(tt)));
118                 end
119                 u(zz,tt) = c - Ubar + sqrt(g/k)*sum(u_temp);
120                 w(zz,tt) = sqrt(g/k)*sum(w_temp);
121                 dudt(zz,tt) = sqrt(g/k)*sum(dudt_temp);
122                 dudx(zz,tt) = sqrt(g/k)*sum(dudx_temp);
123                 dudz(zz,tt) = sqrt(g/k)*sum(dudz_temp);
124 
125                 DUDT(zz,tt) = dudt(zz,tt) + u(zz,tt)*dudx(zz,tt) + w(zz,tt)*dudz(zz,tt);
126             end
127         end
128     end
129 
130     %% Calculate Morison load
131 
132     for tt = 1:length(t);
133         % Calculate force per length in z-direction for writing nodal force
134         for zz = 1:nnode;
135             dz(zz) = z(zz)-z(zz+1);
136             if iMethod ==2 ;
137                 if z(zz)<=zeta(tt) && z(zz-1)<zeta(tt) % fully submerged
138                     dz1(zz)=0.5*(abs(z(zz)-z(zz-1))+abs(z(zz+1)-z(zz)));
139                 elseif z(zz)<=zeta(tt) && z(zz-1)>zeta(tt) % partly submerged
140                     dz1(zz)=0.5*(abs(z(zz+1)-z(zz)))+abs(z(zz)-zeta(tt));
141                 elseif z(zz)<zeta(tt) && z(zz+1)>z(end)
142                     dz1(zz)=0.5*(abs(z(zz)-z(zz-1)));
143                 else
144                     dz1(zz)=0;
145                 end
146                 dF_Morison_z(zz,tt) = (rho*pi*a^2*Cm*DUDT(zz,tt)+rho*a*Cd*abs(u(zz,tt))*u
                        (zz,tt))*dz1(zz);
147 
148             elseif iMethod ==1;
149                 if z(zz)<=0 && z(zz-1)<0 % fully submerged
150                     dz1(zz)=0.5*(abs(z(zz)-z(zz-1))+abs(z(zz+1)-z(zz)));
151                 elseif z(zz)<= 0 && z(zz-1)>0 % first node
152                     dz1(zz)=0.5*(abs(z(zz)-z(zz+1)));
153                 elseif z(zz)<= 0 && z(zz+1)>z(end) % last node
154                     dz1(zz)=0.5*(abs(z(zz)-z(zz-1)));
155                 else
156                     dz1(zz)=0;
157                 end
158                 dF_Morison_mass(zz,tt) = rho*pi*a^2*Cm*DUDT(zz,tt)*dz1(zz);
159                 dF_Morison_drag(zz,tt) = rho*0.25*a*Cd*abs(u(zz,tt))*u(zz,tt)*dz1(zz);
160                 dF_Morison_z(zz,tt) = dF_Morison_mass(zz,tt) + dF_Morison_drag(zz,tt);
161             end
162         end
```

```
    end
    F_Morison(tt) = sum(dF_Morison_z(:,tt),1);

    %% Add ramp

    Nt = length(t);
    tramp = 5*T;
    Nramp = sum(t<tramp);
    dF_Morison_z(:,1:Nramp)=dF_Morison_z(:,1:Nramp).*sin(2*pi/(tramp*4)*t(1:Nramp));
    F_Morison(1:Nramp)=F_Morison(1:Nramp).*sin(2*pi/(tramp*4)*t(1:Nramp));

    %% Write to file
    if iInputfile == 1
        if iMethod ==1;
            outfile = ['nodalforce_S40_Morison_' num2str(r) '.asc'];
        elseif iMethod ==2;
            outfile = ['nodalforce_S40_Morison_SF_' num2str(r) '.asc'];
        end

        outfid = fopen(outfile,'w');
        % header
        % NTDFO
        fprintf(outfid,'%d \n', Nt);

        for tt = 1:length(t) % loop over time steps
            % MDCOMP TIMDFO
            fprintf(outfid,'%d\t %.7e\t \n',nnode,t(tt)); % this has to be written at
                every time step!
            for zz = 1:nnode %loop over nodes
                % RLMAG
                fprintf(outfid,'%.7e\n',dF_Morison_z(zz,tt)/1000); % nodal force at the
                    given time for node j [kN]
            end
        end
        fclose(outfid);
    end
end
```

FNV.m

```
%=========================================================================
%   NAME:       FNV.m
%
%   PURPOSE:    Generate nodal load force files for regular wave tests
%               using FNV method
%
%   BY:         Elise Moen 02.06.20,
%
%   COMMENT:    Nodal loads are found using the FNV method. A stream
%               function wave is generated to obtain the kinematics.
%               Finally, the caculated nodal loads are written to .asc file
%               to be given as input in SIMA
%
%=========================================================================
clear all
close all
addpath('Processed','matlab')

%% Choose run and options
%=========================================================================
```

```
iInputfile = 1;
for r = 1:22
    %% Input data
    Hvec = [1.398,1.632,1.872,2.118,2.364,2.610,2.854,3.096,3.334,3.572,3.806,...
        4.036,4.266,4.494,4.720,4.944,5.168,5.390,5.610,5.830,6.048,6.264]; %S40
    % Hvec =[2.5430,2.9655,3.4034,3.8493,4.2977,4.7448,5.1887,5.6281,6.0629,6.4929,...
    %
        6.9185,7.3399,7.7574,8.1714,8.5823,8.9903,9.3956,9.7986,10.1994,10.5982,10.9953,11.3907];
         %S22

    Tvec = [6:0.5:16.5];
    D = 9; % Diameter (m)
    a = D/2; % Radius (m)
    h = 27; % Water depth (m)
    rho = 1025; % Sea water density (kg/m^3)
    g = 9.81; % Gravitational acceleration (m/s^2)
    T = Tvec(r); % Wave period (s)
    H = Hvec(r); % Wave height (m)
    omega = 2*pi/T; % Circual frequency
    z_sima = [103.9:0.98:108.8 109.3:0.98:114.2 114.7:0.98:119.6 120.1:0.98:125
        125.5:0.98:130.4 130.9:0.98:135.8 136.3:0.98:141.2 141.7:1.225:144.15];
    z = -(z_sima-117.15);
    nnode = length(z)-1;
    dt = 0.01; % Time step
    Np = 60;
    t = [0:dt:Np*T]; % Length of time series
    x = 0; % At centre of model

    %% Stream function waves
    d = h;
    LorTandU = [T 0 1];
    N = 10;
    Hsteps = 20;
    Npos = T*10;
    plt = 0;
    [eta,B,Ubar,k,Q,R] = fenton(H,d,LorTandU,N,Hsteps,Npos,plt)
    c = Ubar;

    % Stream function wave elevation
    eta2 = flip(eta(2,:));
    whole_wave = [eta(2,:) eta2(2:end-1)]-h;
    zeta_temp = zeros(length(whole_wave)*Np,1);
    for i=0:Np-1
        zeta_temp(i*length(whole_wave)+1:((i+1)*length(whole_wave)))=whole_wave(1:end);
    end
    time_temp=eta(1,:)/c;
    dt_temp = time_temp(end)-time_temp(end-1);
    time_temp1 = [time_temp(1):dt_temp:Np*T];

    zeta = interp1(time_temp1(1:length(zeta_temp)),zeta_temp,t); % Sample to same as rest

    %% Stream function kinematics

    for tt = 1:length(t);
        for zz = 1:nnode;
            for j = 1:N;
                u_temp(j) = j*B(j)*cosh(j*k*(z(zz)+h))/cosh(j*k*h)*cos(j*k*(x-c*t(tt)));
                w_temp(j) = j*B(j)*sinh(j*k*(z(zz)+h))/cosh(j*k*h)*sin(j*k*(x-c*t(tt)));

                dudt_temp(j) = j*B(j)*cosh(j*k*(z(zz)+h))/cosh(j*k*h)*j*k*c*sin(j*k*(x-c*
```

```
                    t(tt)));
78                  dudx_temp(j) = j*B(j)*cosh(j*k*(z(zz)+h))/cosh(j*k*h)*j*k*(-1)*sin(j*k*(x
                        -c*t(tt)));
79                  dudz_temp(j) = j*B(j)*j*k*sinh(j*k*(z(zz)+h))/cosh(j*k*h)*cos(j*k*(x-c*t(
                        tt)));
80              end
81              u(zz,tt) = c - Ubar + sqrt(g/k)*sum(u_temp);
82              w(zz,tt) = sqrt(g/k)*sum(w_temp);
83              dudt(zz,tt) = sqrt(g/k)*sum(dudt_temp);
84              dudx(zz,tt) = sqrt(g/k)*sum(dudx_temp);
85              dudz(zz,tt) = sqrt(g/k)*sum(dudz_temp);
86          end
87      end
88      for tt=1:length(t)
89          for zz=1:nnode;
90              if z(zz)<=zeta(tt) && z(zz-1)<zeta(tt) % fully submerged
91                  dz1(zz)=0.5*(abs(z(zz)-z(zz-1))+abs(z(zz+1)-z(zz)));
92              elseif z(zz)<=zeta(tt) && z(zz-1)>zeta(tt) % partly submerged
93                  dz1(zz)=0.5*(abs(z(zz+1)-z(zz)))+abs(z(zz)-zeta(tt));
94              elseif z(zz)<zeta(tt) && z(zz+1)>z(end)
95                  dz1(zz)=0.5*(abs(z(zz)-z(zz-1)));
96              else
97                  dz1(zz)=0;
98              end
99              dF_FNV_z(zz,tt) = (rho*pi*a^2*(dudt(zz,tt)+u(zz,tt)*dudx(zz,tt)+w(zz,tt)*dudz
                    (zz,tt))+rho*pi*a^2*(dudt(zz,tt) + w(zz,tt)*dudz(zz,tt)))*dz1(zz);
100         end
101         dF_FNV_z(16,tt) = dF_FNV_z(16,tt) + rho*pi*a^2*4/g*u(16,tt)^2*dudt(16,tt); %
                evaulated and added at z=0
102         F_FNV(tt) = sum(dF_FNV_z(:,tt),1);
103     end
104
105     % Add ramp
106     Nt = length(t);
107     tramp = 5*T;
108     Nramp = sum(t<tramp);
109     dF_FNV_z(:,1:Nramp)=dF_FNV_z(:,1:Nramp).*sin(2*pi/(tramp*4)*t(1:Nramp));
110     F_FNV(:,1:Nramp)=F_FNV(:,1:Nramp).*sin(2*pi/(tramp*4)*t(1:Nramp));
111
112     %% Write to file
113     if iInputfile == 1
114         outfile = ['nodalforce_S40_FNV_' num2str(r) '.asc'];
115
116         outfid = fopen(outfile,'w');
117         % header
118         % NTDFO
119         fprintf(outfid,'%d \n', Nt);
120
121         for tt = 1:length(t) % loop over time steps
122             % MDCOMP TIMDFO
123             fprintf(outfid,'%d\t %.7e\t \n',nnode,t(tt)); % this has to be written at
                    every time step!
124             for zz = 1:nnode %loop over nodes
125                 % RLMAG
126                 fprintf(outfid,'%.7e\n',dF_FNV_z(zz,tt)/1000); % nodal force at the given
                        time for node j [kN]
127             end
128         end
129         fclose(outfid);
130     end
```

```
end
```

F Scripts: Irregular wave input

Morison_irreg.m

```
%==========================================================================
%   NAME:       Morison_irreg.m
%
%   PURPOSE:    Generate nodal load force files for irregular wave tests
%
%   BY:         Elise Moen 02.06.20,
%
%   COMMENT:    User can select between linear kinematics or stream
%               function kinematics, add Wienke slamming load and write
%               input file
%
%==========================================================================
clear all
close all

%% Choose options
%==========================================================================
iMethod = 2; % 1 - Linear, 2 - Stream function
iWienke = 1; % 1 - Add Wienke slamming load
iInputfile = 0; % 1 - Write inputfile

%% Input data
%==========================================================================

for iseed = [201 202 203 205 207 208 209 210 214 216] % Relevant wave seeds

    wseed = num2str(iseed);

    if iMethod == 1 % Linear kinematics
        loadname = ['wave_org_' wseed '.mat']; load(loadname);
        u = u_org;
        DUDT = dudt_org;
    elseif iMethod ==2 % Stream function kinematics
        loadname = ['wave_emb_' wseed '.mat']; load(loadname);
        u = u_emb;
        DUDT = dudt_emb;
        zeta = wave_emb;
    end

    z_sima = [103.9:0.98:108.8 109.3:0.98:114.2 114.7:0.98:119.6 120.1:0.98:125
        125.5:0.98:130.4 130.9:0.98:135.8 136.3:0.98:141.2 141.7:1.225:144.15];
    z = -(z_sima-117.15);
    nnode = length(z)-1;

    D = 9; % Diameter (m)
    a = D/2; % Radius (m)
    h = 27; % Water depth (m)
    rho = 1025; % Sea water density (kg/m^3)
    g = 9.81; % Gravitational acceleration (m/s^2)

    Cm = 2; % Mass coefficient
    Cd = 1; % Drag coefficient

```

```
    for tt = 1:length(t);

        % Calculate force per length in z-direction for writing nodal force
        for zz = 1:nnode;
            dz(zz) = z(zz)-z(zz+1);
            if iMethod ==2 ;

                if z(zz)<=zeta(tt) && z(zz-1)<zeta(tt) % fully submerged
                    dz1(zz)=0.5*(abs(z(zz)-z(zz-1))+abs(z(zz+1)-z(zz)));
                elseif z(zz)<=zeta(tt) && z(zz-1)>zeta(tt) % partly submerged
                    dz1(zz)=0.5*(abs(z(zz+1)-z(zz)))+abs(z(zz)-zeta(tt));
                elseif z(zz)<zeta(tt) && z(zz+1)>z(end)
                    dz1(zz)=0.5*(abs(z(zz)-z(zz-1)));
                else
                    dz1(zz)=0;
                end

                dF_Morison_mass(zz,tt) = rho*pi*a^2*Cm*DUDT(zz,tt)*dz1(zz);
                dF_Morison_drag(zz,tt) = rho*0.25*a*Cd*abs(u(zz,tt))*u(zz,tt)*dz1(zz);
                dF_Morison_z(zz,tt) = dF_Morison_mass(zz,tt) + dF_Morison_drag(zz,tt);

            elseif iMethod ==1;

                if z(zz)<=0 && z(zz-1)<0 % fully submerged
                    dz1(zz)=0.5*(abs(z(zz)-z(zz-1))+abs(z(zz+1)-z(zz)));
                elseif z(zz)<= 0 && z(zz-1)>0 % first node
                    dz1(zz)=0.5*(abs(z(zz)-z(zz+1)));
                elseif z(zz)<= 0 && z(zz+1)>z(end) % last node
                    dz1(zz)=0.5*(abs(z(zz)-z(zz-1)));
                else
                    dz1(zz)=0;
                end

                dF_Morison_mass(zz,tt) = rho*pi*a^2*Cm*DUDT(zz,tt)*dz1(zz);
                dF_Morison_drag(zz,tt) = rho*0.25*a*Cd*abs(u(zz,tt))*u(zz,tt)*dz1(zz);
                dF_Morison_z(zz,tt) = dF_Morison_mass(zz,tt) + dF_Morison_drag(zz,tt);
            end
        end
    end
    savename= ['dF_Morison_z_' wseed '.mat'];
    save(savename,'dF_Morison_z','t','SF')
end
%%
T0_vec = [1.464180059132752e+03, 2.758981163366641e+03, 5.355440598922057e+03, ...
    6.038399431496664e+03, 7.034383996697868e+03, 9.031160207122541e+03,...
    2.424394255346392e+03, 9.450153784945493e+03, 2.048169566544405e+03,...
    2.707941314893645e+03, 7.945537737976771e+03, 4.653324153905130e+03,...
    7.632229228290362e+03, 6.410523979102521e+03, 1.703685736713269e+03,...
    5.043758043947747e+03, 9.214324117381664e+03, 6.025109498484062e+02,...
    9.479137649785588e+02, 9.753070549288343e+03] ; % Time of peak

eventseed = [201 201 201 201 201 201 202 203 205 205 207 208 208 ...
    209 210 210 210 214 216 216 217 218]; % Wave seed for each event

if iWienke == 1;
    for e =1:20;
        wseed = num2str(eventseed(e));
        loadname = ['dF_Morison_z_' wseed '.mat']
        load(loadname);

```

```
113         if exist('t_new','var');
114             disp('Exsists')
115         else
116             dt_W = 0.01;
117             t_new = [0:dt_W:t(end)];
118             for zz = 1:nnode;
119                 dF_Morison_z_new(zz,:) = interp1(t,dF_Morison_z(zz,:),t_new);
120             end
121         end
122         T0 = T0_vec(e);
123         iT0 = sum(t_new<T0);
124 
125         c = SF.c(e);
126         zeta_b = SF.zeta_b(e);
127         lambda = 0.28;
128         TW = 13/32*a/c;% Duration of Wienke impact
129         iTshift = sum(t_new<(T0-a/c));
130         dt = t_new(2)-t_new(1)
131         tw = [0:dt:TW+1];
132         Cs=zeros(1,length(tw));
133         for tt=1:length(tw)
134             if 0<tw(tt)&& tw(tt)<1/8*a/c;
135                 Cs(tt) = 2*pi - 2*sqrt((c*tw(tt))/a)*atanh(sqrt(1-1/4*(c*tw(tt))/a));
136             end
137             if 3/32*a/c <= tw(tt)-1/32*a/c && tw(tt)-1/32*a/c <= 12/32*a/c;
138                 Cs(tt) = pi*sqrt(1/(6*c/a*(tw(tt)-1/32*a/c)))-nthroot((8/3*c/a*(tw(tt)
                        -1/32*a/c)),4)...
139                     *atanh(sqrt(1-c/a*(tw(tt)-1/32*a/c)*sqrt(6*c/a*(tw(tt)-1/32*a/c))));
140             end
141             FI(tt) = rho*a*c^2*Cs(tt)*lambda*zeta_b;
142         end
143 
144         dF_Morison_z_new(10,iTshift:iTshift+length(tw)-1)=dF_Morison_z_new(10,iTshift:
                iTshift+length(tw)-1)+FI;
145 
146         save(loadname,'dF_Morison_z_new','t_new');
147         clear FI
148         clear tw
149         clear dF_Morison_z_new
150         clear t_new
151 
152     end
153 end
154 
155 %% Write to file
156 if iInputfile == 1
157     for iseed = [201 202 203 205 207 208 209 210 214 216]
158         wseed = num2str(iseed);
159         loadname = ['dF_Morison_z_' wseed '.mat']
160         load(loadname);
161         if iMethod ==1;
162             outfile = ['nodalforce_lin_' wseed '.asc'];
163             Nt = length(t);
164             outfid = fopen(outfile,'w');
165             % header
166             % NTDFO
167             fprintf(outfid,'%d \n', Nt);
168 
169             for tt = 1:length(t) % loop over time steps
170                 % MDCOMP TIMDFO
```

```
171                 fprintf(outfid,'%d\t %.7e\t \n',nnode,t(tt)); % this has to be written at
                        every time step!
172                 for zz = 1:nnode %loop over nodes
173                     % RLMAG
174                     fprintf(outfid,'%.7e\n',dF_Morison_z(zz,tt)/1000); % nodal force at
                            the given time for node j [kN]
175                 end
176             end
177             fclose(outfid);
178         elseif iMethod ==2 && iWienke == 0;
179             outfile = ['nodalforce_SF_' wseed '.asc'];
180             Nt = length(t);
181             outfid = fopen(outfile,'w');
182             % header
183             % NTDFO
184             fprintf(outfid,'%d \n', Nt);
185 
186             for tt = 1:length(t) % loop over time steps
187                 % MDCOMP TIMDFO
188                 fprintf(outfid,'%d\t %.7e\t \n',nnode,t(tt)); % this has to be written at
                        every time step!
189                 for zz = 1:nnode %loop over nodes
190                     % RLMAG
191                     fprintf(outfid,'%.7e\n',dF_Morison_z(zz,tt)/1000); % nodal force at
                            the given time for node j [kN]
192                 end
193             end
194             fclose(outfid);
195         elseif iMethod ==2 && iWienke == 1;
196             outfile = ['nodalforce_SFW_' wseed '.asc'];
197             Nt = length(t_new);
198             outfid = fopen(outfile,'w');
199             % header
200             % NTDFO
201             fprintf(outfid,'%d \n', Nt);
202 
203             for tt = 1:length(t_new) % loop over time steps
204                 % MDCOMP TIMDFO
205                 fprintf(outfid,'%d\t %.7e\t \n',nnode,t_new(tt)); % this has to be
                        written at every time step!
206                 for zz = 1:nnode %loop over nodes
207                     % RLMAG
208                     fprintf(outfid,'%.7e\n',dF_Morison_z_new(zz,tt)/1000); % nodal force
                            at the given time for node j [kN]
209                 end
210             end
211             fclose(outfid);
212         end
213     end
214 end
```

NTNU

Norwegian University of
Science and Technology